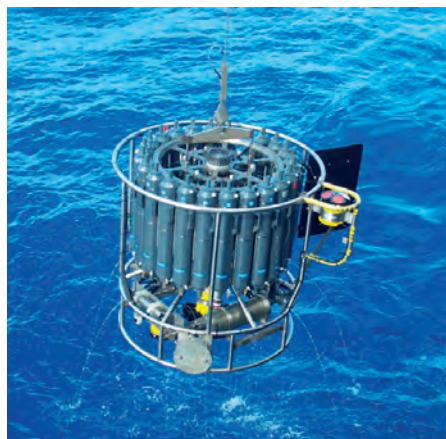
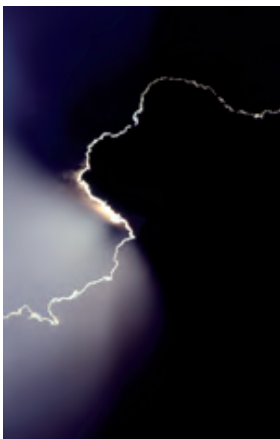




## Climate instabilities under strong solar forcing

Max Popp



## Hinweis

Die Berichte zur Erdsystemforschung werden vom Max-Planck-Institut für Meteorologie in Hamburg in unregelmäßiger Abfolge herausgegeben.

Sie enthalten wissenschaftliche und technische Beiträge, inklusive Dissertationen.

Die Beiträge geben nicht notwendigerweise die Auffassung des Instituts wieder.

Die "Berichte zur Erdsystemforschung" führen die vorherigen Reihen "Reports" und "Examensarbeiten" weiter.



## Notice

*The Reports on Earth System Science are published by the Max Planck Institute for Meteorology in Hamburg. They appear in irregular intervals.*

*They contain scientific and technical contributions, including Ph. D. theses.*

*The Reports do not necessarily reflect the opinion of the Institute.*

*The "Reports on Earth System Science" continue the former "Reports" and "Examensarbeiten" of the Max Planck Institute.*

## Anschrift / Address

Max-Planck-Institut für Meteorologie  
Bundesstrasse 53  
20146 Hamburg  
Deutschland

Tel.: +49-(0)40-4 11 73-0  
Fax: +49-(0)40-4 11 73-298  
Web: [www.mpimet.mpg.de](http://www.mpimet.mpg.de)

## Layout:

Bettina Diallo, PR & Grafik

Titelfotos:

vorne:

Christian Klepp - Jochem Marotzke - Christian Klepp

hinten:

Clotilde Dubois - Christian Klepp - Katsumasa Tanaka

Climate instabilities under strong solar forcing

Max Popp

aus Winterthur, Schweiz

Hamburg 2014

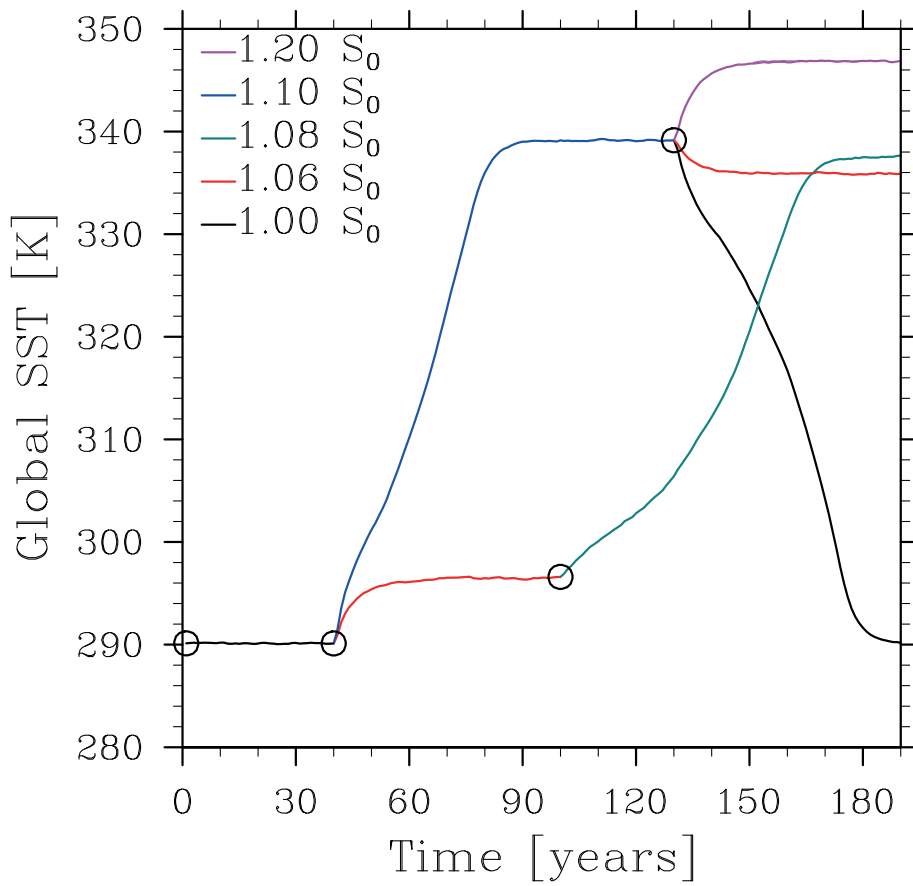
Max Popp  
Max-Planck-Institut für Meteorologie  
Bundesstrasse 53  
20146 Hamburg

Als Dissertation angenommen  
vom Fachbereich Geowissenschaften der Universität Hamburg

auf Grund der Gutachten von  
Prof. Dr. Jochem Marotzke  
und  
Dr. Hauke Schmidt

Hamburg, den 17. Dezember 2013  
Professor Dr. Christian Betzler  
Leiter des Fachbereichs für Geowissenschaften

## Climate instabilities under strong solar forcing



Max Popp

Hamburg 2014



---

## Abstract

Water rich planets, such as Earth, are virtually certain to lose most of their water if only the total solar irradiance (TSI) becomes large enough. There are two potential pathways which could lead to the loss of an ocean of water, but there is controversy on which pathway an Earth-like planet would take. Therefore, in this thesis, I investigate different aspects of the response of an Earth-like planet to strong solar forcing with a variety of different models.

One of the pathways leading to the loss of water is the so called Runaway Greenhouse, a process in which all oceans are evaporated due to a self-sustaining water vapor feedback loop. The influence of clouds on the onset of a Runaway Greenhouse has not been systematically investigated. Therefore I take up the topic in this thesis. I use a single-column version of the general circulation model ECHAM6, which includes an appropriate representation of clouds for this task. My results suggest that the TSI necessary to trigger a Runaway Greenhouse is substantially increased if clouds are included in the radiative transfer calculations. Cloud thickness increases with TSI and the associated increase in cloud albedo allows the column to remain in a steady-state for large values of TSI. Furthermore, the increase in cloud albedo allows the column to attain steady states with surface temperatures larger than 360 K.

The other pathway to the loss of water leads to a Moist Greenhouse, a regime of steady states in which an ocean is present at the surface, but water vapor becomes abundant enough in the upper atmosphere for the planet to lose water at a fast rate. At present-day it is uncertain whether a planet would attain the Moist Greenhouse regime or whether it would go into a Runaway Greenhouse before. Therefore, I investigate the fate of an aqua-planet under strong solar forcing with the three-dimensional version of ECHAM6. I find that the planet encounters a climate instability as the TSI is increased to a value between 1.06 and 1.08 time the present-day TSI on Earth ( $S_0$ ). However, the planet does not go into a Runaway Greenhouse, but attains a new steady state with a global-mean surface temperature of 339 K. The planet remains in the same regime of warm steady states for a TSI of at least up to 1.2  $S_0$ , because the cloud albedo increases with the TSI allowing the planet to remain in equilibrium. The warm states lie in the Moist Greenhouse regime and therefore the aqua-planet would lose substantial amounts of water in this regime.

In the last part of the thesis I focus again on the Runaway Greenhouse. Previous studies have shown that a limitation of outgoing longwave radiation (OLR) can cause a Runaway Greenhouse. However, these previous studies have made specific assumptions on the temperature profiles, and the proposed mechanisms leading to a limitation of

OLR may have been crucially influenced by the assumptions made. Therefore, I use a one-dimensional gray-atmosphere model to assess which properties of temperature profiles cause a limitation of OLR. I find that a limitation occurs if the temperature in the optically thin region of the atmosphere remains finite, and if in the optically thick region of the atmosphere the temperature does not increase faster with optical depth than a nearly-exponentially increasing limit profile. Furthermore, I find that in physically relevant settings the occurrence of a limitation of OLR depends indeed on the assumptions made.

# Contents

<b>Abstract</b>	<b>i</b>
<b>1 Introduction</b>	<b>1</b>
1.1 Motivation and open questions . . . . .	1
1.2 Thesis outline . . . . .	6
<b>2 Initiation of a Runaway Greenhouse in a cloudy column</b>	<b>7</b>
2.1 Introduction . . . . .	8
2.2 Energy balance and the Runaway Greenhouse . . . . .	10
2.3 Experimental design . . . . .	12
2.3.1 Model . . . . .	12
2.3.2 Experiments . . . . .	16
2.4 Results . . . . .	18
2.4.1 Critical TSI and multiple equilibria . . . . .	18
2.4.2 The effect of clouds on the energy balance . . . . .	20
2.4.3 Summary . . . . .	27
2.5 Discussion . . . . .	29
2.5.1 Boundary layer clouds . . . . .	29
2.5.2 Clouds in the warm regime . . . . .	30
2.5.3 Unusual behavior of the Tompkins scheme . . . . .	32
2.6 Comparison to previous studies . . . . .	34
2.7 Implications for Venus . . . . .	36
2.8 Conclusions . . . . .	37
<b>3 Climate instabilities on an Earth-like planet under strong solar forcing</b>	<b>39</b>
3.1 Introduction . . . . .	40
3.2 Experimental design . . . . .	43
3.2.1 Model . . . . .	43
3.2.2 Experimental setup . . . . .	45

3.3	Results . . . . .	46
3.3.1	Steady states and double equilibria . . . . .	46
3.3.2	Climate instability and transient behavior . . . . .	51
3.4	Discussion . . . . .	56
3.4.1	Limitations of the model . . . . .	56
3.4.2	Physical interpretation of the results . . . . .	57
3.5	Comparison to previous work . . . . .	61
3.6	Implications for planetary science . . . . .	63
3.7	Conclusions . . . . .	65
3.A	Influence of the sponge on the control climate . . . . .	66
<b>4</b>	<b>The Runaway Greenhouse as a result of a limitation of outgoing long-wave radiation</b>	<b>67</b>
4.1	Introduction . . . . .	68
4.2	Methods . . . . .	70
4.2.1	Model atmosphere . . . . .	70
4.2.2	Radiative transfer . . . . .	71
4.3	Results . . . . .	72
4.3.1	Assumptions . . . . .	72
4.3.2	Conditions . . . . .	72
4.4	Discussion . . . . .	74
4.4.1	Interpretation of the conditions . . . . .	74
4.4.2	The limit profile . . . . .	76
4.4.3	Application to selected temperature profiles . . . . .	77
4.4.4	A comparison to the conditions obtained by Sugiyama et al. (2005)	80
4.4.5	Generalizations and limitations . . . . .	82
4.5	Summary . . . . .	83
4.A	Mathematical principles of the Nakajima limitation . . . . .	84
<b>5</b>	<b>Conclusions</b>	<b>85</b>
5.1	Answers to the research questions . . . . .	85
5.2	Synthesis and implications . . . . .	87
5.2.1	Differences between the effects of solar forcing on the climate of an aqua-planet and of CO <sub>2</sub> -induced forcing on Earth's climate .	87
5.2.2	A look into Earth's far future . . . . .	88
5.2.3	Early Venus . . . . .	89
5.2.4	The habitable zone of our solar system . . . . .	89
5.2.5	The Runaway Greenhouse at different stages of stellar evolution	90

---

5.2.6	Simulation of an entire Runaway Greenhouse . . . . .	91
<b>A</b>	<b>Appendix</b>	<b>93</b>
A.1	Moist physics in ECHAM6 . . . . .	93
A.1.1	Pressure . . . . .	93
A.1.2	Specific humidity . . . . .	95
A.1.3	Relative humidity . . . . .	97
A.1.4	Density . . . . .	98
A.1.5	Specific gas constants . . . . .	99
A.1.6	Density- and virtual temperatures . . . . .	100
A.2	Modifications of the Radiation Code . . . . .	101
A.2.1	Molecular absorption coefficients . . . . .	101
A.2.2	Lookup-table for the integrated Planck function . . . . .	102
A.2.3	Concentrations of radiatively active gases . . . . .	102
	<b>List of Figures</b>	<b>107</b>
	<b>Bibliography</b>	<b>113</b>
	<b>Acknowledgements</b>	<b>115</b>



# Chapter 1

## Introduction

### 1.1 Motivation and open questions

The long-term temporal evolution of the climate of water-rich planets such as Earth is heavily influenced by changes of solar activity. Stellar theory predicts that the luminosity of our sun was only about 0.7 times the present-day value when the sun reached the main sequence (period of a star in which it is fueled by fusion of hydrogen to helium in its core) 4.5 billion years ago and that the luminosity will increase to 2.2 times the present-day value until the end of the main sequence in 5.5 billion years (Sackmann et al., 1993). Currently the luminosity of our sun increases at a rate of around 9 % per billion years (Sackmann et al., 1993). Therefore, in this thesis, I investigate the impact of increased values of total solar irradiance (TSI) on the climate of a water-rich planet.

We can think of increasing the TSI from the present-day value of Earth ( $S_0$ ) in three ways. First, by moving the planet closer to the sun, second, by assuming a future state of the sun at which its luminosity is higher, and, third, by assuming another type of star of higher luminosity. Hence, studying an Earth-like planet under increased values of TSI may be used as an analogue for similar planets at different stages in stellar evolution, at different distances from the sun, and even for planets in other solar systems.

The first efforts for studying Earth-like planets under increased values of TSI were motivated by Venus. Presently only very little water is present in the atmosphere of Venus (Meadows and Crisp, 1996), but this may have been different in the past. This raised the question whether a planet which is habitable, that is, liquid water is stable at the surface, could lose nearly all of its water and hence become uninhabitable, as the

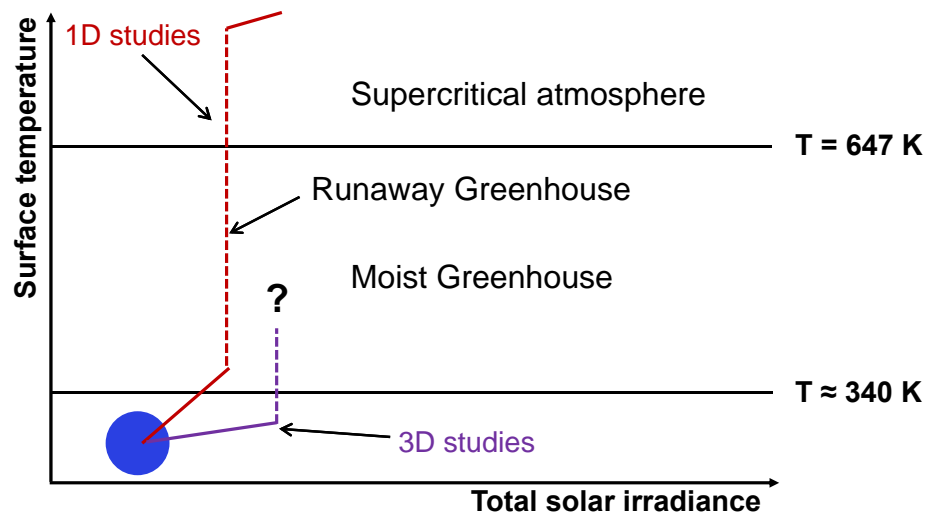


Figure 1.1: Sketch of previous results obtained in studies considering strong solar forcing. The blue ball denotes Earth’s present surface temperature and TSI. Solid (colored) lines denote steady states found in previous studies and dashed lines denote climate instabilities. The red lines indicates the results obtained with one-dimensional models and violet lines denote the results obtained with three-dimensional models. The lower limit of surface temperatures of the Moist Greenhouse is supposed to lie around 340 K and the hard upper limit is the critical temperature of water (647 K).

TSI increases. Observations indicate that Venus did indeed lose considerable amounts of water (Donahue et al. (1982), Debergh et al. (1991)). In recent years, the question of where the habitable zone around stars is located, has seen increasing attention as the exploration of extrasolar planets has made a leap forward thanks to a new generation of telescopes. Investigating water-rich planets under increased values of TSI is crucial to determine the inner edge of the habitable zone and thus to evaluate the habitability of newly discovered extrasolar planets.

Atmospheres of terrestrial planets lose water through photo-dissociation of water vapor close to the top of the atmosphere and the subsequent escape of hydrogen to space. This process is occurring also on present-day Earth, but the volume mixing ratio of water vapor in the upper atmosphere is too low to lead to a substantial loss of water (e.g. Pierrehumbert (2010)). In order for a terrestrial planet to lose water at a rate which could lead to the loss of an Earth-like ocean, water vapor must become substantially more abundant than on present-day Earth in the region at the top of the atmosphere where hydrogen can escape to space. Presently two different paths have been suggested that could lead to the loss of an ocean of water, termed Runaway Greenhouse and Moist Greenhouse, which will both be defined in the next two

paragraphs.

In the 1960s the idea was advanced that a water-vapor feedback-loop, termed Runaway Greenhouse, could lead to the evaporation of all oceans on an Earth-like planet (Gold (1964), Komabayashi (1967), Ingersoll (1969)). In the resulting steam-atmosphere, water vapor would be abundant up to the top of the atmosphere, and hence water could be lost at a fast rate. Furthermore, a Runaway Greenhouse would directly lead to the loss of all liquid water at the surface and would hence render a planet uninhabitable before the water vapor is lost.

In contrast, a planet could also lose water at a fast rate to space in a Moist Greenhouse, a regime of steady states in which water is still stable at the surface (Kasting et al., 1984). Unlike for the Runaway Greenhouse, a planet in the Moist Greenhouse would remain habitable until nearly all the water is lost to space. The Moist Greenhouse emerges as the cold trapping of water vapor at the tropopause becomes less effective with increasing steady-state surface temperatures and eventually water vapor becomes abundant in the stratosphere.

Studies with one-dimensional models with state-of-the-art radiative transfer schemes suggest that the equilibrium surface temperature increases with TSI and attains the Moist Greenhouse regime at around 340 K. As the TSI is further increased, the equilibrium surface temperature increases as well until a Runaway Greenhouse occurs as a critical value of TSI is attained (Kasting (1988), Kopparapu et al. (2013), Goldblatt et al. (2013)). The maximum equilibrium surface temperature in the Moist Greenhouse lies in the upper 300 K's. Studies with three-dimensional models suggest that the equilibrium surface temperature increases less fast with TSI than for one-dimensional models. However, a climate instability is encountered before the Moist Greenhouse regime is attained, and hence at much lower surface temperature. In contrast, the critical TSI necessary to trigger a climate instability is lower in the three-dimensional models than in the one-dimensional model (Ishiwatari et al. (2002) Boer et al. (2005), Ishiwatari et al. (2007)). The results of previous one-dimensional and three-dimensional simulations are sketched in Figure 1.1.

All previous three-dimensional studies have used models with either simplified physics (Ishiwatari et al. (2002), Ishiwatari et al. (2007)) or the model could not be run to sufficiently high temperatures to ascertain that the encountered climate instability would indeed lead to a Runaway Greenhouse (Boer et al., 2005). Thus, it is uncertain whether a climate instability leading to a Runaway Greenhouse would occur before a planet attains the Moist Greenhouse regime, and whether if a planet attains a steady state in this regime, a Runaway Greenhouse would occur before an ocean of water is

lost there. Furthermore it is uncertain which value of TSI would be necessary to cause a climate instability. Therefore, I address the following questions in this thesis:

**What TSI is necessary to cause a climate instability when starting from a present-day Earth-like climate? Would this climate instability prevent an Earth-like planet from attaining the Moist Greenhouse regime?**

The influence of clouds on the climate under increased values of TSI has received only little attention, and the influence of clouds on the climates in warm steady states is not well understood. In particular, there has not been a systematic assessment of the role of clouds in the context of the Runaway Greenhouse. However, several studies have pointed out that clouds may have a crucial influence on the TSI required to trigger a Runaway Greenhouse (e.g. Kasting (1988), Abe et al. (2011), Goldblatt et al. (2013)). Two studies with general circulation models suggest that a decrease of cloud cover may lead to a climate instability and to a runaway behavior of surface temperatures (Boer et al. (2005), Heinemann (2009)). However, these two studies did not run to high enough temperatures to assess whether a Runaway Greenhouse was underway. Hence, I tackle the following questions:

**What is the influence of clouds on the critical TSI for the onset of a Runaway Greenhouse? How do clouds influence the energy balance in warm climates?**

In order to understand the influence of clouds on the global energy balance, it is imperative to understand the underlying circulation (Stevens and Bony, 2013). Several studies have investigated or discussed different aspects of the interaction between clouds and circulation for present-day Earth conditions and for moderate greenhouse-gas forcing scenarios with a moderate increase in global-mean surface temperatures (e.g. Hartmann and Larson (2002), Bony et al. (2006), Brient and Bony (2013)). Only Boer et al. (2005) have briefly discussed aspects of the interaction between clouds and circulation under strong solar forcing in their simulations, but not for steady states at high global-mean surface temperatures. Hence, not only has the interaction between clouds and circulation never been investigated for very warm climates, but the global circulation itself has never been investigated under such conditions with a general circulation model (GCM) with a representation of clouds. Therefore, I address the following questions in this thesis:

**How does the global circulation differ between a present-day Earth-like climate and a much warmer climate? How does the circulation affect the cloud formation in a warm climate?**

Theoretical studies of the Runaway Greenhouse have established the paradigm that a limitation of outgoing longwave radiation (OLR) is the cause of a Runaway Greenhouse (e.g. Komabayashi (1967), Ingersoll (1969), Nakajima et al. (1992)). If the absorbed solar radiation exceeds the upper bound of OLR, an uncompensated gain of energy occurs, which leads to a steady increase of temperature. Only once the thermal emission spectrum shifts into the visible, does the intensity of the outgoing radiation increase again, and a new steady state can be attained. Nakajima et al. (1992) showed that the limitation of OLR in their model is caused by the decoupling of the temperature profile from the surface temperature. Sugiyama et al. (2005) hypothesized that the decoupling of the temperature profile from the surface temperature should be a sufficient condition for a limitation of OLR to occur for an optically thick troposphere. However, no previous study has investigated the limitation of OLR without making specific assumptions on the temperature profile. As a consequence, it remains unclear whether the decoupling of the temperature profile from the surface temperature is the ultimate cause of a limitation of OLR or whether the decoupling is linked to the specific assumptions in the previous studies. Furthermore, even though Nakajima et al. (1992) pointed out that the temperature profile decouples from the surface temperature in their model, a convincing argument for why the model should exhibit this behavior was not introduced. Therefore, I pose the following questions in this thesis:

**Which properties of a temperature profile cause the OLR to be limited?  
Do physically realistic assumptions lead to profiles with such properties?**

## 1.2 Thesis outline

In each of the the three main chapters I present the work conducted with a different model. The work with each model makes its particular contribution to answer one or several of the research questions. As a courtesy to the reader, the main chapters are organized in a way that they can be read independently.

In Chapter 2 I present the results and the discussion of the simulations I perform with the single-column version of ECHAM6. I investigate the influence of clouds on the energy balance of the column for a large range of TSIs and for surface temperatures of up to 120° C. The focus lies on how clouds affect the critical TSI for the initiation of the Runaway Greenhouse and on the cloud-dynamics involved. This work has been submitted to the Journal of the Atmospheric Sciences for publication (Popp et al., 2014).

In Chapter 3 I present the results and the discussion of the simulations of an aqua-planet I performed with the three-dimensional version of ECHAM6. I investigate abrupt climate transitions leading away from a present-day Earth-like climate, assess the required TSI to start such transitions, and explore the role of clouds in causing and possibly terminating such transitions. Furthermore, I describe how the circulation evolves with increasing global-mean surface temperatures and how the circulations affects the clouds. Finally I discuss the emergence of the Moist Greenhouse on the aqua-planet and assess whether the aqua-planet may become uninhabitable in the Moist Greenhouse regime.

In Chapter 4 I use a one-dimensional gray-atmosphere model to investigate the influence of assumptions made on temperature profiles and their influence on a possible limitation of OLR.

In Chapter 5 I draw the main conclusions from the work presented in this thesis. Furthermore, I make the synthesis of the results of the different chapters and put their relevance into the larger context of habitability.

## Chapter 2

# Initiation of a Runaway Greenhouse in a cloudy column

A one-dimensional radiative-convective equilibrium model with two different cloud-cover schemes is used to investigate the influence of clouds on the onset of a Runaway Greenhouse under strong solar forcing. By comparing experiments with clear-sky conditions (clouds are transparent to radiation) to experiments with full-sky conditions (clouds are radiatively active), we find that the critical solar irradiance to trigger a Runaway Greenhouse is increased from 1.10 - 1.12 times the present-day total solar irradiance (TSI) on Earth ( $S_0$ ) for clear-sky conditions to 1.50-1.70  $S_0$  for full-sky conditions. Cloud thickness increases with TSI, leading to a substantially higher albedo, which in turn allows the climate to remain in equilibrium for markedly higher values of TSI. Clouds play an important role in the occurrence of climate instabilities and multiple equilibria for a large range of TSI. Furthermore our results suggest that steady states with sea surface temperatures higher than 360 K exist for a large range of TSI with full-sky conditions. The outgoing longwave radiation has attained a minimum in these warm states. Therefore, a further thickening of clouds increases only their shortwave effect. This mechanism allows the column to remain in balance for large values of TSI.

## 2.1 Introduction

In the 1960's the idea was advanced that under strong radiative forcing a runaway water-vapor feedback may occur, which may lead to the evaporation of all oceans on an Earth-like planet (e.g., Gold (1964), Komabayashi (1967), Ingersoll (1969)). This was the original idea of a so-called Runaway Greenhouse. The idea was used to explain how Venus could have lost most of its water and could have ended up with the inhospitable atmosphere it has today. But even though fifty years have passed, little attention has been paid to the role of clouds in the context of the Runaway Greenhouse, a topic we take up here.

Vardavas and Carver (1985) used a simple cloud model of one layer and assumed that the cloud cover and the cloud-optical depth were proportional to the atmospheric water vapor content. Other studies made use of models with a constant cloud layer as well or investigated the influence of clouds tentatively for single cloud layers at different temperature and pressure levels (e.g., Kasting (1988)). The radiative-convective model used by Renno et al. (1994) and Renno (1997) included the thermodynamic properties of convective clouds, but the radiative properties of the clouds were either neglected, or a fixed cloud cover was assumed.

More recently Boer et al. (2005) studied the influence of strong solar forcings on Earth's climate with the NCAR CSM v1.4 general circulation model (GCM). The cloud cover decreased with increasing temperature, causing the temperature to run away. This result stands in contrast to the expectation by Vardavas and Carver (1985) that cloud cover is to increase with increasing temperatures. The GCM simulation failed, however, before the average surface temperature exceeded 340 K, and therefore only a relatively small range of temperatures could be explored. Heinemann (2009) found as well that the cloud cover decreased with increasing surface temperature in the GCM ECHAM5/MPIOM. The surface temperatures also ran away for high temperatures, but only because, due to the prescribed concentrations of ozone, high concentrations of ozone came to lie in the troposphere as the tropopause climbed. This runaway behavior was, however, likely a direct consequence of the limitations of the radiation code in the applied GCM. Abe et al. (2011) studied the habitable zone of dry Earth-like planets, i.e., with no oceans but including soil moisture. They used a GCM and included the radiative properties of clouds, but they did not focus on the influence of the clouds on the onset of a Runaway Greenhouse. As in Boer et al. (2005) and Heinemann (2009), the cloud cover decreased with increasing temperatures in Abe et al. (2011).

In the present study we investigate the influence of clouds and especially of the radiative properties of clouds on the onset of a Runaway Greenhouse. We use a one-dimensional radiative-convective equilibrium model with a complex hydrological cycle and two different schemes for the representation of cloud cover. Our model differs from all previous one-dimensional studies in that it computes self-consistently the location of clouds, their fractional cover, their microphysical properties, and their radiative properties. This allows us to explore the behavior of the column under strong solar forcings for full-sky conditions (i.e., with full cloud-radiation interaction) as well as for clear-sky conditions (i.e., clouds are transparent to radiation), for sea surface temperatures of up to 120° C (393.15 K). This maximum sea surface temperature is much higher than the ones attained in the three-dimensional studies by Boer et al. (2005) and Heinemann (2009) and especially extends over the whole range of temperature where according to Renno (1997) equilibria may be expected. Our approach permits us to quantify the effect of clouds and to estimate their influence on the value of the total solar irradiance (TSI) that is necessary to trigger a Runaway Greenhouse; moreover we can explore the possibility of equilibria at high temperatures, as found by Renno (1997). Ensembles of simulations give us the possibility to assess the robustness of our results.

This chapter is organized as follows. We start with a discussion of the energy balance in the context of the Runaway Greenhouse in Section 2.2 before describing the single-column model, including its limitations, and the experimental setup in Section 2.3. The results are presented and described in Section 2.4. We discuss the behavior of the clouds in detail in Section 2.5 and compare our results to previous studies in Section 2.6. We discuss our results in the context of early Venus in Section 2.7 before stating our conclusions in Section 2.8.

## 2.2 Energy balance and the Runaway Greenhouse

We start with some considerations of the energy balance at the top of the atmosphere. The crucial mechanism for a Runaway Greenhouse to occur is that the outgoing long-wave radiation (OLR) decouples from the surface temperature as the atmosphere becomes optically thick in the infrared (Nakajima et al. (1992), Goldblatt and Watson (2012)). As a consequence, the OLR does not change anymore with surface temperature and is hence bounded. If the absorbed solar radiation exceeds the upper bound of OLR, an uncompensated gain of energy occurs — the Runaway Greenhouse.

The temporal average of the steady-state energy balance at the top of the atmosphere can be written as

$$(1 - \alpha_e)\bar{S} = \bar{I}_0 \quad , \quad (2.1)$$

where an overbar denotes the temporal averages,  $I_0$  is the OLR,  $S$  the TSI, and  $\alpha_e$  the effective albedo defined as

$$\alpha_e = \frac{\bar{S}_R}{\bar{S}} \quad , \quad (2.2)$$

with  $S_R$  the reflected shortwave radiation at the top of the atmosphere. The advantage of using the effective albedo is that unlike the albedo, the effective albedo is a direct measure for the absorbed energy. For example, the value of the albedo during night has no influence on the energy budget.

We now discuss different assumption on the optical properties of the atmosphere. We start by assuming that the atmosphere absorbs longwave radiation but no short-wave radiation, and that clouds are transparent to all radiation. Without atmospheric shortwave absorption, the effective albedo and hence  $\bar{S}_R$  remain constant. According to Eq. (2.1), if the TSI is increased, an equilibrium can only exist if the OLR increases accordingly. It follows in this case that if the OLR is bounded and if  $(1 - \alpha_e) \cdot \bar{S}$  exceeds the maximum that the OLR can attain, a Runaway Greenhouse occurs.

We assume next that the atmosphere also absorbs shortwave radiation but that the clouds are still transparent to radiation. This is our clear-sky conditions (CSC) setup (see Section 2.4). The reflected shortwave radiation can now change with temperature, because the amount of atmospheric water vapor changes and because water vapor absorbs solar radiation. Hence, the reflected shortwave radiation will decrease with increasing sea surface temperature (SST) (at least in the range of temperatures we consider). If the TSI is increased, an equilibrium can only be attained if the OLR compensates not only for the increase in TSI but also for the reduction of reflected shortwave radiation. Therefore the atmosphere is more susceptible to a Runaway Greenhouse in CSC than in the case without solar absorption by the atmosphere.

At last we assume that clouds interact with radiation as in our full-sky conditions (FSC) setup. Clouds can lead to an increase or to a decrease of OLR, depending on the height at which the cloud top is located. Since the surface in our model is assumed to consist of liquid water, clouds always lead to an increase in albedo. So, depending on whether the cloudiness increases or decreases, depending on the level at which clouds form, and depending on whether the shortwave or the longwave effect dominates, clouds may have a stabilizing or a destabilizing effect.

## 2.3 Experimental design

### 2.3.1 Model

We employ a modified single-column version of the general circulation model ECHAM6 (Stevens et al., 2013), which we couple to a mixed-layer ocean. We will not discuss the entire model here, but will give a short general introduction as well as a summary of the radiation and the convection schemes, the hydrological cycle, the microphysical cloud scheme, and the two cloud-cover schemes. The column consists of 95 vertical layers and is energetically isolated. Hence, energy can only leave and enter the column in form of radiation at the top of the atmosphere.

Several physical formulations of thermodynamic variables implemented in ECHAM6 are based on the assumption that the mass of water vapor in the atmosphere is negligible compared to the mass of dry air. In this case the pressure  $p$  of a column of dry air (which is assumed to be equal to the total pressure in ECHAM6) corresponds closely to the pressure  $P$  of a column of moist air, and the volume mixing ratio of water vapor corresponds closely to the specific humidity. However, if water vapor becomes a major constituent of the atmosphere, these approximations may lead to considerable errors. Therefore we use more generalized formulations to allow for a more precise representation of thermodynamic variables, that is, we include the mass of water vapor to calculate the total pressure, and we omit all approximations where small specific humidities were assumed (as for example for the calculation of density). For more details on the formulations please refer to the appendix of the thesis.

ECHAM6 does not conserve energy (Stevens et al., 2013), a common problem in many general circulation models (Mauritsen et al., 2012). Even in the single-column version of ECHAM6 the energy is not conserved, as can be recognized by top-of-the-atmosphere imbalances in steady states. These imbalances are, however, small enough in all except three simulations not to affect the results qualitatively, and even the impact on the quantitative results should be minor. We will point out the three problematic simulations in the results section.

### Radiation

The employed radiation scheme is the Rapid Radiative Transfer Model (RRTMG) (Mlawer et al. (1997), Iacono et al. (2008)). It uses the correlated-k method to solve the radiative transfer equations in the two-stream approximation. The shortwave radiation

spectrum is divided into 14 bands, and the longwave radiation spectrum is divided into 16 bands. Since the lookup-tables of the molecular absorption coefficients are designed for a limited range of temperatures only, we perform an exponential extrapolation for temperatures up to 400 K for the longwave radiation scheme. We apply the same extrapolation scheme to the lookup-tables for the absorption coefficients of the water vapor self-broadened continuum in the shortwave radiation scheme, but we keep the original linear extrapolation scheme for all the other absorption coefficients. However, the exponential extrapolation likely becomes increasingly inaccurate the further the temperature leaves the range of the original look-up tables of the absorption coefficients.

We introduce the water vapor self-broadened continuum in the upper atmosphere radiation calculations, since water vapor concentrations increase above 100 hPa as the temperatures rise. Rayleigh scattering by water vapor is neglected since the effect is minor at temperatures below 120° C (Kopparapu et al., 2013). We do not include the effect of pressure broadening by water vapor on the molecular absorption coefficients. The consequence of neglecting this is that the absorption will be too weak where pressure is larger than it is for the present-day Earth climate. Since we are interested in the behavior of clouds, it is of interest to assess how this may influence cloud formation. Large increases in total pressure occur only in the convective region in our model. This region is dominated by convection, and therefore we do not expect clouds to be substantially affected within this region by neglecting the water-vapor-induced pressure broadening. However, since the absorption of radiation may be too weak where water vapor is abundant, the upward longwave radiation flux at the top of the convective region may be overestimated, and therefore cloud formation at the top and above the convective region may be underestimated. With these caveats in mind, we expect nonetheless the radiation scheme to allow for a satisfactory picture of clouds in the range of temperatures we consider, even if the values of critical TSI and other variables may be affected. Furthermore, transient simulations under clear-sky conditions indicate that for increasing SST the OLR converges towards a value between 310 and 320 W m<sup>-2</sup>. This convergence of OLR shows that our model is indeed suited to investigate the initiation of a Runaway Greenhouse.

Clouds are incorporated in the radiation calculation, assuming the so-called maximum-random-overlap assumption, that is, cloud layers are assumed to be maximally overlapping if they are adjacent to one another, and randomly overlapping if they are separated by a clear layer. Clouds are not assumed to be blackbodies; rather their absorptivity depends on the combined optical depths of the cloud, the gas in which they are embedded, and the interstitial aerosol. The microphysics to determine the optical properties of the cloud particles involve the liquid-water and ice paths,

cloud-drop radii, as well as liquid-water and ice content. Cloud scattering is included in the form of a single-scattering albedo in the shortwave calculation, but is neglected in the longwave calculations. The single-scattering albedo is calculated by assuming Mie scattering from cloud droplets. Clouds are not considered in the radiative transfer routines if the cloud-condensate does not exceed  $10^{-7}$  kg per kg of air.

## Hydrological Cycle

Water vapor enters the atmosphere by means of evaporation at the surface. The water (in all phases) is then distributed within the column by convection and vertical diffusion. Water can leave the column by means of convective and large-scale precipitation and by surface condensation. The specific mass of water (in all phases) and, as a consequence, the relative humidity in the model are the result of this hydrological cycle. Precipitation is created by the convection scheme as well as by the cloud microphysical scheme. Even though the convection scheme provides information about detrained water to the microphysical cloud scheme, cloud condensate is created or destroyed by the microphysical cloud scheme only.

## Convection

ECHAM6 uses a mass-flux scheme for cumulus convection (Tiedtke, 1989), with modifications for the penetrative convection according to Nordeng (1994). The contribution of cumulus convection to the large-scale budgets of heat, moisture, and momentum is represented by an ensemble of clouds consisting of updrafts and downdrafts in a steady state. Depending on moisture convergence at the surface and depth of the convection cell, the model will either run in penetrative, mid-level, or shallow convection mode.

## Clouds

We make use of two different schemes for the representation of cloud cover, the Sundqvist scheme (Sundqvist et al., 1989) and the Tompkins scheme (Tompkins, 2002). These two cloud schemes have been tuned for the use with present-day Earth's climate (Lohmann and Roeckner (1996), Tompkins (2002), Mauritsen et al. (2012)). Obviously we cannot ascertain that the choices of the tuning parameters are still valid for temperatures of up to  $120^{\circ}$  C. However, both models relate cloud cover to relative humidity, with the Tompkins scheme also explicitly modeling the subgrid variability of water.

Since relative humidity should be crucial to cloud formation irrespective of the surface temperature, we expect the models not to go far astray at high temperatures.

The microphysical cloud scheme is the same for both cloud-cover schemes and is described in detail in Lohmann and Roeckner (1996). However, the microphysical scheme is handled differently by the two cloud-cover schemes in that the threshold for cloud growth is different. The microphysical cloud scheme consists of prognostic equations for the vapor, liquid, and ice phases. There are explicit microphysics for warm phase, mixed phase, and ice clouds. The cloud-condensation-nuclei concentration follows a prescribed vertical profile which is typical for present-day Earth maritime conditions. Since we have no estimate of the aerosol load in a hypothetical warm climate, we just assume that this profile is also a reasonable choice for warmer climates. The microphysics does not require changes for the use of the scheme in warm climates, since cloud formation in a warm-phase cloud, in which potential changes may occur, is not directly temperature dependent (at least not in the range of temperatures we consider). Hence the present formulation should be valid.

### **The Sundqvist scheme**

We do not discuss the parameterization of fractional cloud cover in detail but give a short summary thereof; for more details please refer to Lohmann and Roeckner (1996). Cloud cover  $C$  is parametrized as a function of relative humidity  $r$  at each layer of the column. For  $r > r_0$ , where  $r_0 < r_{sat}$  is a subgrid-scale condensation threshold and  $r_{sat}$  is the relative humidity of saturation ( $= 1$  in general), condensational growth of cloud droplets occurs. The threshold  $r_0$  is an empirical function of pressure and decreases from  $r_0(p_{surf}) = 0.9$  at the surface to  $r_0(p \approx 500 \text{ hPa}) = 0.7$  and remains constant at 0.7 above about 500 hPa.

### **The Tompkins scheme**

Again we do not discuss the parameterization of fractional cloud cover in detail, but we give a short summary thereof; for more details please refer to Roeckner et al. (2003). In simple terms, the difference between the Tompkins scheme and the Sundqvist scheme is that the Tompkins scheme does not only relate fractional cloud cover directly to relative humidity as the Sundqvist scheme does, but also models the fluctuations of water within each layer of the column in order to determine the fractional cloud cover. Furthermore the Tompkins scheme takes information directly from other processes of the hydrological cycle to calculate the cloud cover. In technical terms, the scheme is based on a statistical-dynamical approach. Neglecting temperature fluctuations, that is, assuming that subgrid-scale cloud formation is caused solely by fluctuations in total water content, the fractional cloud cover can be expressed as the integral of a beta

distribution. This beta distribution represents the probability density function of the abundance of water (in all phases). The choice of the probability density function was guided by simulations with a cloud-resolving model, which was run on a horizontal domain of about 90 km x 90 km and 21 km in the vertical (Tompkins, 2002).

### 2.3.2 Experiments

All simulations are performed for 50 years or until the sea surface temperature (SST) exceeds 393.15 K. Since for this SST the ocean exceeds the boiling temperature at normal pressure and hence water vapor becomes very abundant in the atmosphere, the atmosphere is opaque enough to shield effectively the radiation emitted from the surface. Hence it is likely that the OLR decouples from the SST, in which case a Runaway Greenhouse would occur (Nakajima et al., 1992). In our transient simulations with clear-sky conditions, the OLR shows evidence of convergence at SSTs around 393.15 K, but it has not yet completely attained its maximum value. However, we should keep in mind that irrespectively of the convergence of OLR our setup ultimately does not allow us to determine whether the oceans will completely evaporate or not. We will nonetheless speak of a Runaway Greenhouse if the simulations are terminated due to SSTs exceeding 393.15 K.

The obliquity of our planet is set to zero, and we assume a perfectly spherical orbit around its star. Hence there is no seasonal cycle. Since the velocity of rotation is not changed from present-day Earth, the column experiences a day-night cycle of 24 hours. The column is located at 38 N, because in this case the temporal average of the angle of incidence of the solar radiation in the column corresponds to the temporal and spatial average of solar radiation on the sphere. The TSI is varied by changing the total intensity of the flux, but leaving the ratio of intensities per band unchanged.

We perform all simulations for FSC as well as for CSC. Clouds are transparent to radiation in CSC, but all the other cloud physics are active. All the physics are active in FSC, including the cloud-radiation interaction. The set of FSC simulations is performed twice, once for the Sundqvist and once Tompkins scheme. Hence, in total three sets of simulations are performed. In CSC we make use of the Sundqvist scheme to produce (transparent) clouds. In order to obtain comparable settings for CSC and FSC, we increase the surface albedo in CSC such that the temporal average of SST does not differ by more than 1 K from the value obtained for FSC when the present-day value of TSI is applied. The surface albedo is therefore increased from 0.07 to 0.28 in clear-sky conditions. The greenhouse-gas concentrations are kept at present-day values (except for water vapor, which is a prognostic variable).

	<b>CSC</b>	<b>FSC with the Sundqvist scheme</b>	<b>FSC with the Tompkins scheme</b>
TSI:	1.00 - 1.55 $S_0$ (Total 12)	1.00 - 1.55 $S_0$ (Total 12)	1.00 - 1.70 $S_0$ (Total 15)
Initial SSTs:			
cold:	285.8, 286.8, 287.8 K	285.8, 286.8, 287.8 K	285.8, 286.8, 287.8 K
warm:	382.2, 383.2, 384.2 K (Total 6)	382.2, 383.2, 384.2 K (Total 6)	361.6, 362.6, 363.6 K (Total 6)
Number of simulations	6 x 12 = 72	6 x 12 = 72	6 x 15 = 90

Table 2.1: Overview of the experimental setup.

We will henceforth denote the present-day value of TSI with  $S_0$ . The control simulations are performed for 50 years with an annually averaged incoming solar radiation ( $\overline{S_0}$ ) of  $340 \text{ W m}^{-2}$ . As for a sphere,  $\overline{S}$  corresponds to  $\text{TSI}/4$  for the column. We conduct simulations for a combination of different initial conditions and of different TSIs for the three different setups (Table 2.1). The simulations are performed for TSIs starting from  $1.00 S_0$  up to  $1.55 S_0$  in steps of  $0.05 S_0$ . Additional simulations are performed for the Tompkins scheme for  $1.60 S_0$ ,  $1.65 S_0$  and  $1.70 S_0$ .

For each value of TSI six different initial conditions are considered, which are divided into two ensembles with different ranges of initial SSTs. The initial SSTs of the ensemble with a cold start are 285.8 K, 286.8 K and 287.8 K, and the atmospheric initial conditions are identical for all three SSTs. The initial SSTs of the ensemble with a warm start are 382.2 K, 383.2 K and 384.2 K (with identical atmospheric initial conditions for all three SSTs) for CSC and FSC with the Sundqvist scheme, whereas they are 361.6 K, 362.6 K and 363.6 K (with identical atmospheric initial conditions for all three SSTs) for the ensemble with a warm start for FSC with the Tompkins scheme. The reason for choosing two ensembles with a very different range of SST is that we want to investigate whether multiple equilibria are possible (Renno, 1997). The difference in the range of SSTs for the ensemble with a warm start is introduced because the Sundqvist scheme produces stable climates in the 380's K and the Tompkins scheme in the 360's K (see results). Note that our approach does not allow us to determine whether we find all possible multiple equilibria.

## 2.4 Results

### 2.4.1 Critical TSI and multiple equilibria

#### Clear-sky conditions

The temporal average of SSTs over the last five years for CSC shows that a Runaway Greenhouse occurs for all simulations for TSIs larger than  $1.15 S_0$  (Figure 2.1, top left panel). For a TSI of  $1.10 S_0$ , all simulations with a cold start attain an equilibrium with SSTs of 305.7 K, whereas all simulations with a warm start go into a Runaway Greenhouse. Hence the critical value of TSI to trigger a Runaway Greenhouse for initial SSTs in the 380's K is smaller than the one for initial SSTs in the 280's K, which is a consequence of the considerably stronger solar and infrared absorption by water vapor in the warm climate. Two different equilibria are attained for a TSI of 1.00 and  $1.05 S_0$  with temperatures in the 280's K for simulations with a cold start and in the 370's K for those with warm start; this result is consistent with Renno (1997). The three simulations with a warm start with  $1.00 S_0$  have a radiative imbalance at the top of the atmosphere of around  $-15 \text{ W m}^{-2}$  without notable change of temperature. Due to the missing energy in the calculations for the atmospheric and the surface temperature (see subsection 2.32.3.1), it is not certain if these simulations should be in a steady state or if they should go into a Runaway Greenhouse.

In order to further constrain the critical TSI for simulations with a cold start, we perform longer simulations in the range between  $1.10 S_0$  and  $1.15 S_0$  and find that the critical TSI is between  $1.10 S_0$  and  $1.13 S_0$ . The radiative imbalance at the top of the atmosphere decreases with SST up to approximately 315 K but increases sharply at larger temperatures (Figure 2.2), indicating a bifurcation at this SST.

#### Full-sky conditions with the Sundqvist scheme

The temporal average of SSTs over the last five years for FSC with the Sundqvist scheme shows that a Runaway Greenhouse occurs for all simulations with a TSI of  $1.55 S_0$ . All simulations attain an equilibrium with surface temperatures of approximately 380 K for TSIs between  $1.40 S_0$  and  $1.50 S_0$  (Figure 2.1, top right panel). Warm and cold starts result in different equilibria with surface temperatures of approximately 370 K for a warm start and 290 K for a cold start for TSIs below  $1.40 S_0$ , indicating a bistability in the climate. However, in two simulations with a TSI of  $1.00 S_0$  with a warm start, the temperatures keep decreasing and longer simulations reveal that they attain an equilibrium with a surface temperature of approximately 290 K. In order to

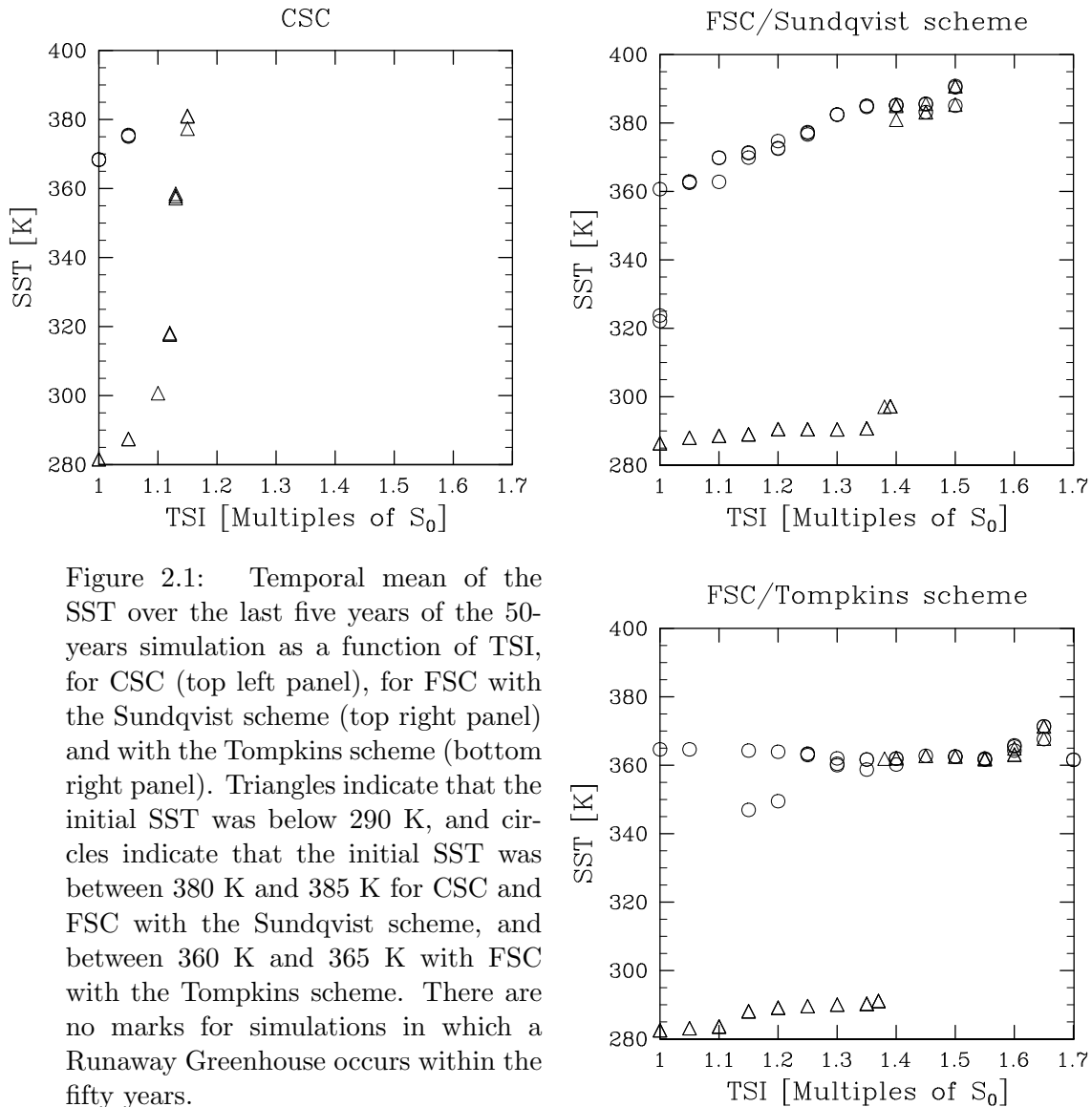


Figure 2.1: Temporal mean of the SST over the last five years of the 50-years simulation as a function of TSI, for CSC (top left panel), for FSC with the Sundqvist scheme (top right panel) and with the Tompkins scheme (bottom right panel). Triangles indicate that the initial SST was below 290 K, and circles indicate that the initial SST was between 380 K and 385 K for CSC and FSC with the Sundqvist scheme, and between 360 K and 365 K with FSC with the Tompkins scheme. There are no marks for simulations in which a Runaway Greenhouse occurs within the fifty years.

further constrain the critical TSI for simulations with a cold start we perform further simulations in the range between  $1.35 S_0$  and  $1.40 S_0$  and find that the critical TSI is between  $1.39 S_0$  and  $1.40 S_0$ . The equilibria are at around 296 K for the range of  $1.38$  to  $1.39 S_0$ , but the sharp increase in radiative imbalance at larger temperatures indicates, that this is the highest possible SST for an equilibrium to exist in the cold regime (Figure 2.2).

### Full-sky conditions with the Tompkins scheme

The picture for the simulations with the Tompkins scheme (Figure 2.1, bottom right panel) with a cold start is similar to the one obtained with the Sundqvist scheme with the following notable differences : The critical TSI is markedly higher and lies between

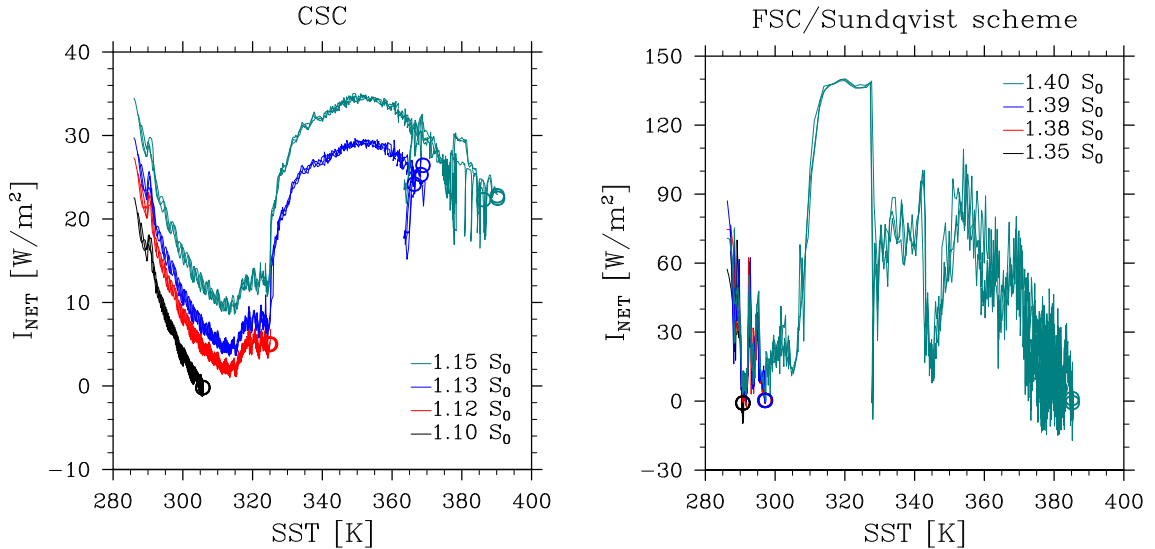


Figure 2.2: Temporal evolution of the radiative imbalance at top of the atmosphere ( $I_{NET}$ ) as a function of SST for four realizations with an initial  $SST_{ini}$  of 286.8 K but different TSIs. For CSC (left panel) TSIs are  $1.10 S_0$  (black),  $1.12 S_0$  (red),  $1.13 S_0$  (blue) and  $1.15 S_0$  (green). For FSC with the Sundqvist scheme (right panel) the TSIs are  $1.35 S_0$  (black),  $1.38 S_0$  (red),  $1.39 S_0$  (blue) and  $1.40 S_0$  (green). The circles mark the value of the temporal average over the last five years of the 50-years simulation.

$1.65 S_0$  and  $1.70 S_0$ , and the equilibrium SSTs in the warm regime is only approximately 370 K. However, for simulations with a warm start the picture is more varied, and the model fails in 9 simulations for 5 different TSIs ( $1.00$ ,  $1.05$ ,  $1.10$ ,  $1.15$  and  $1.20 S_0$ ). The failure occurs because the algorithm for condensation overestimates in a first step the amount of water vapor to be condensed, if strong oversaturation occurs. Nonetheless the successful simulations allow for a relatively complete picture. All simulations with a warm start terminate in a warm state for TSIs smaller than  $1.70 S_0$ . For TSIs of both  $1.15 S_0$  and  $1.20 S_0$ , the two simulations that terminate successfully attain two different states within the warm regime. So there are at least three equilibria for this range of TSI. One of the simulations goes into a Runaway Greenhouse while the other two attain an equilibrium for a TSI of  $1.70 S_0$ .

## 2.4.2 The effect of clouds on the energy balance

### The Sundqvist scheme and Tompkins scheme for present-day conditions

In order to facilitate the interpretation of our results we present the cloud climatology for present-day simulations (Figure 2.3). We have a larger effective albedo than for present-day Earth for both the Sundqvist scheme and the Tompkins scheme; we find 0.37 for the Sundqvist scheme and 0.40 for the Tompkins scheme. The cloud albedo is

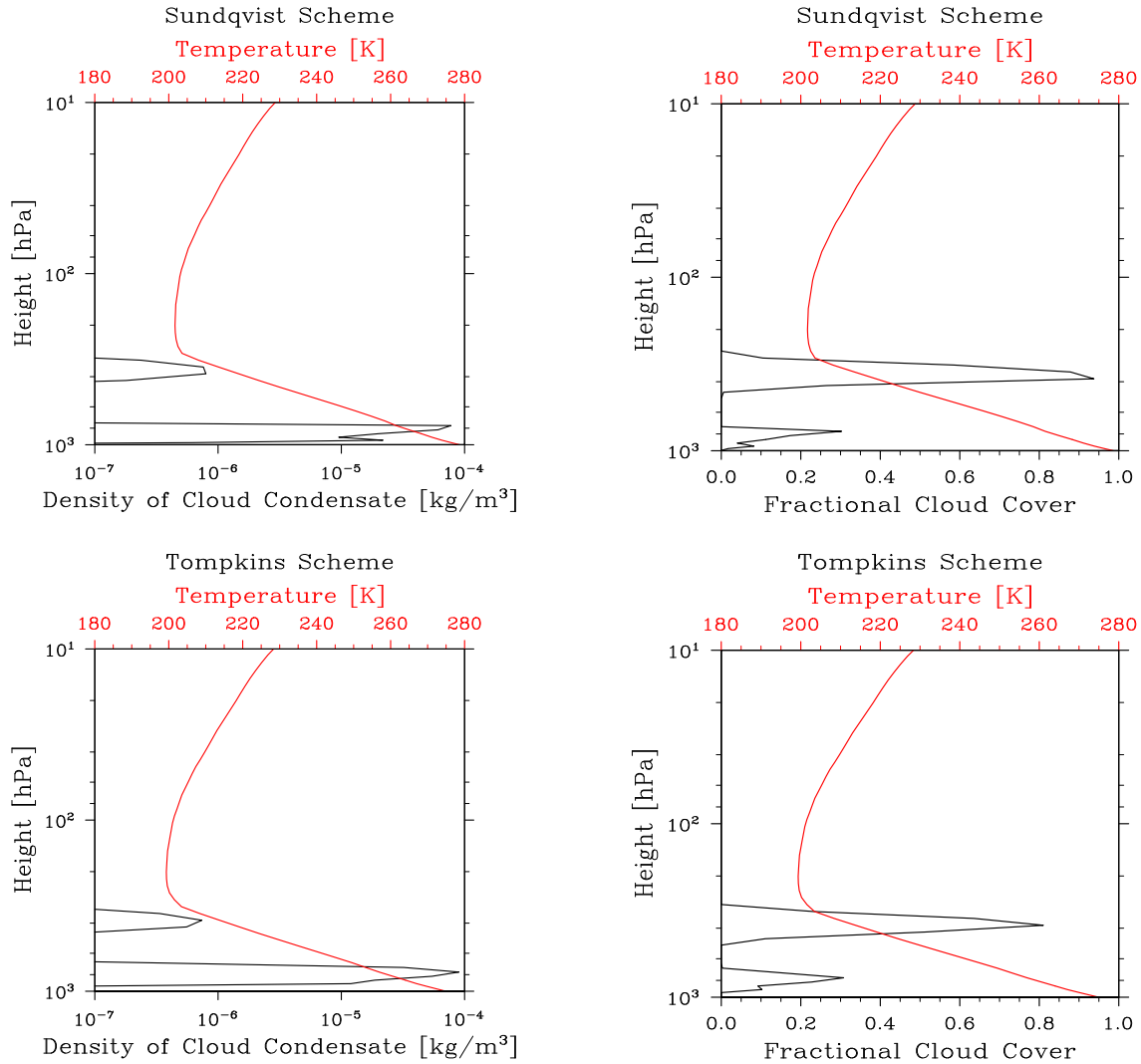


Figure 2.3: Atmospheric profiles of the temporal average over the last five years of simulation of cloud condensate (black, left panels) and temperature (red, left panels) and of cloud cover (black, right panels) and temperature (red, right panels). The vertical axis is the height in terms of pressure of dry air. The panels on the top show the results of one simulation with a cold start ( $SST_{ini} = 286.8$  K) for present-day insolation  $S_0$  for the Sundqvist scheme and the lower panels show the result of a simulation with the same initial SST for the same TSI but for the Tompkins scheme. These are the two control simulations for present-day climate for each of the cloud-cover schemes.

more strongly influenced by the lower clouds at the top of the boundary layer than by the clouds in the upper troposphere, despite the cloud cover being larger for the upper clouds, because the lower clouds contain more condensate. In order to maintain the energy balance, the OLR is therefore lower than for present-day Earth, with values of  $217 \text{ W m}^{-2}$  for the Sundqvist scheme and  $204 \text{ W m}^{-2}$  for the Tompkins scheme. We choose not to tune our model to fit Earth's energy balance but to keep the values of the tuning parameters which give the best results in 3-dimensional simulations (Mauritsen

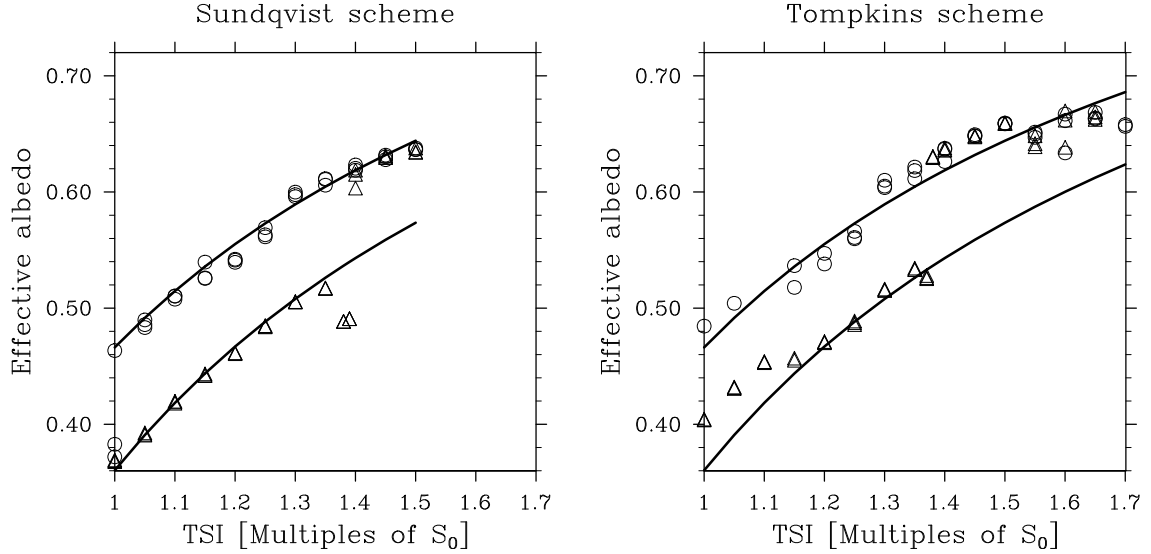


Figure 2.4: Temporal mean of the effective albedo over the last five years of simulation as a function of TSI for FSC with the Sundqvist scheme (left panel) and FSC with the Tompkins scheme (right panel). The curves are calculated by solving the energy balance at the top of the atmosphere for the albedo, with the OLR kept constant. Triangles indicate that the initial SST was below 290 K, and circles indicate that the initial SST was between 380 K and 385 K for CSC and FSC with the Sundqvist scheme, and between 360 K and 365 K with FSC the Tompkins scheme. There are no marks for simulations in which a Runaway Greenhouse occurs.

et al., 2012). Due to the inherently simplified geometry of a one-dimensional model compared to a three-dimensional model, it is not surprising that our one-dimensional model does not reproduce Earth’s averaged energy balance exactly. We will keep this in mind when discussing the results.

### FSC with the Sundqvist scheme

A TSI between  $1.00 S_0$  and  $1.35 S_0$  only leads to a small increase in equilibrium SST with increasing TSI, because in equilibrium the effective albedo increases as well with increasing TSI (Figure 2.4). The increase in albedo is caused by an increase of both fractional cloud cover and cloud condensate of the water clouds in the lower troposphere (Figure 2.5). The low clouds form at the top of the boundary layer which is, however, not recognizable in Figure 2.5 because of the coarse temperature resolution of the contours. Clouds remain approximately at the same position in the cold regime, but the temperature within the boundary layer increases gently with TSI. This increase in temperature leads to an increase in moisture within the boundary layer (not shown), which explains the increased amount of cloud condensate within the clouds. However,

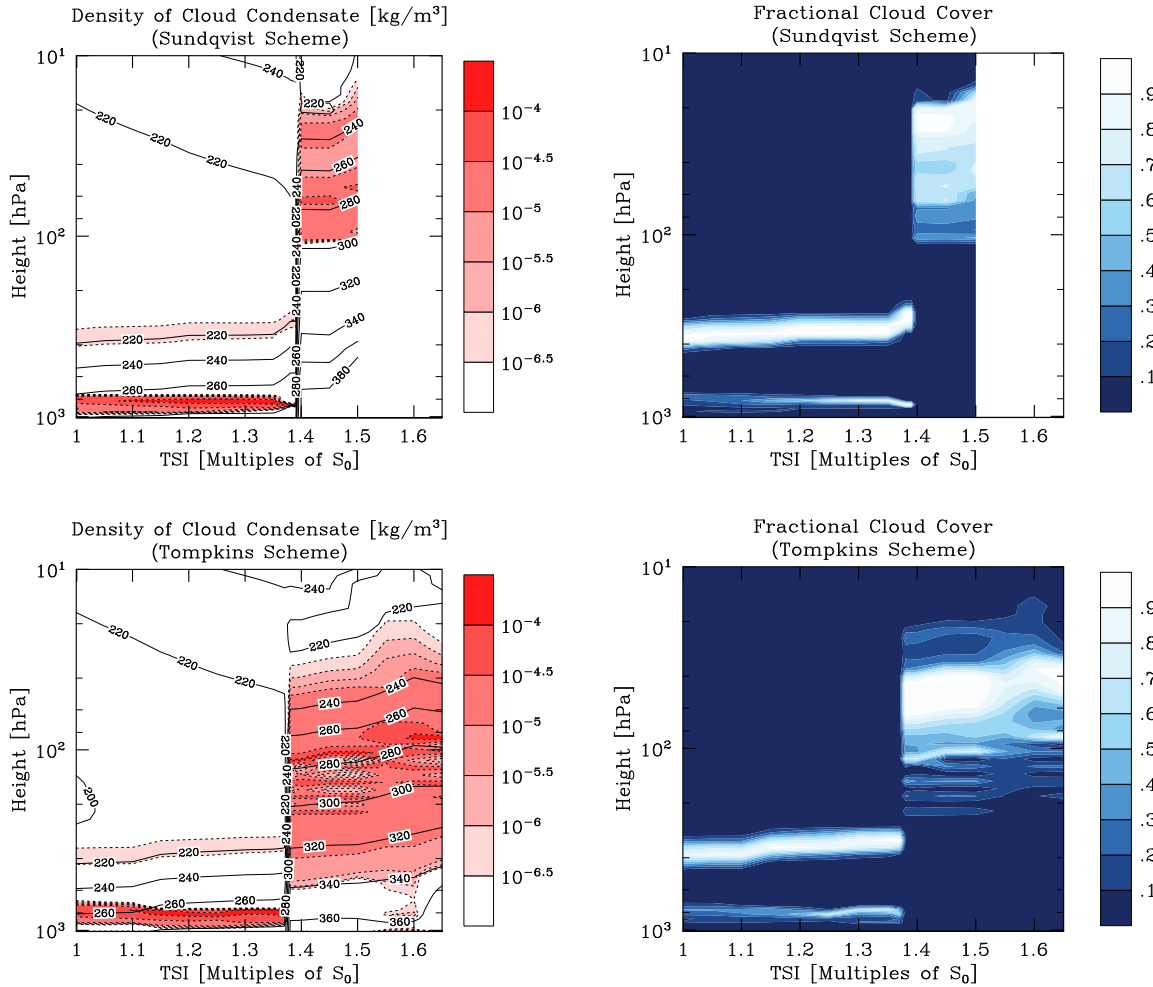


Figure 2.5: Cloud cover and cloud condensate in equilibrium: The top panels show the the temporal average over the last five years of simulation of cloud condensate (left) and fractional cloud cover (right) of one ensemble member with a cold start for different values of TSI with the Sundqvist scheme. The lower panels show the same variables for the Tompkins scheme. The vertical coordinate is height (in terms of pressure of dry air). The line contours on the left panels denote the temperatures in K. There are no steady states for TSIs larger than  $1.5 S_0$  for the Sundqvist scheme. Furthermore the simulation with a TSI of  $1.4 S_0$  was extended for an additional 30 years for the Sundqvist scheme to ensure that the equilibrium was attained.

as a critical temperature is exceeded, a further increase in surface temperature leads to a decrease of relative humidity at the top of the boundary layer (not shown), which causes the clouds at the top of the boundary layer to vanish (Figure 2.6). The disappearance of the boundary-layer clouds and the associated drop in albedo are the cause of the climate transition towards high temperatures. Only after the atmospheric structure has substantially changed is a new equilibrium attained, because eventually the shortwave effect outweighs the longwave effect of the clouds which form in the upper troposphere in the warm state (Figure 2.7). Clouds form at temperatures below 300 K in this warm regime (Figure 2.5). The spatial extent of the cloud region is relatively wide and reaches

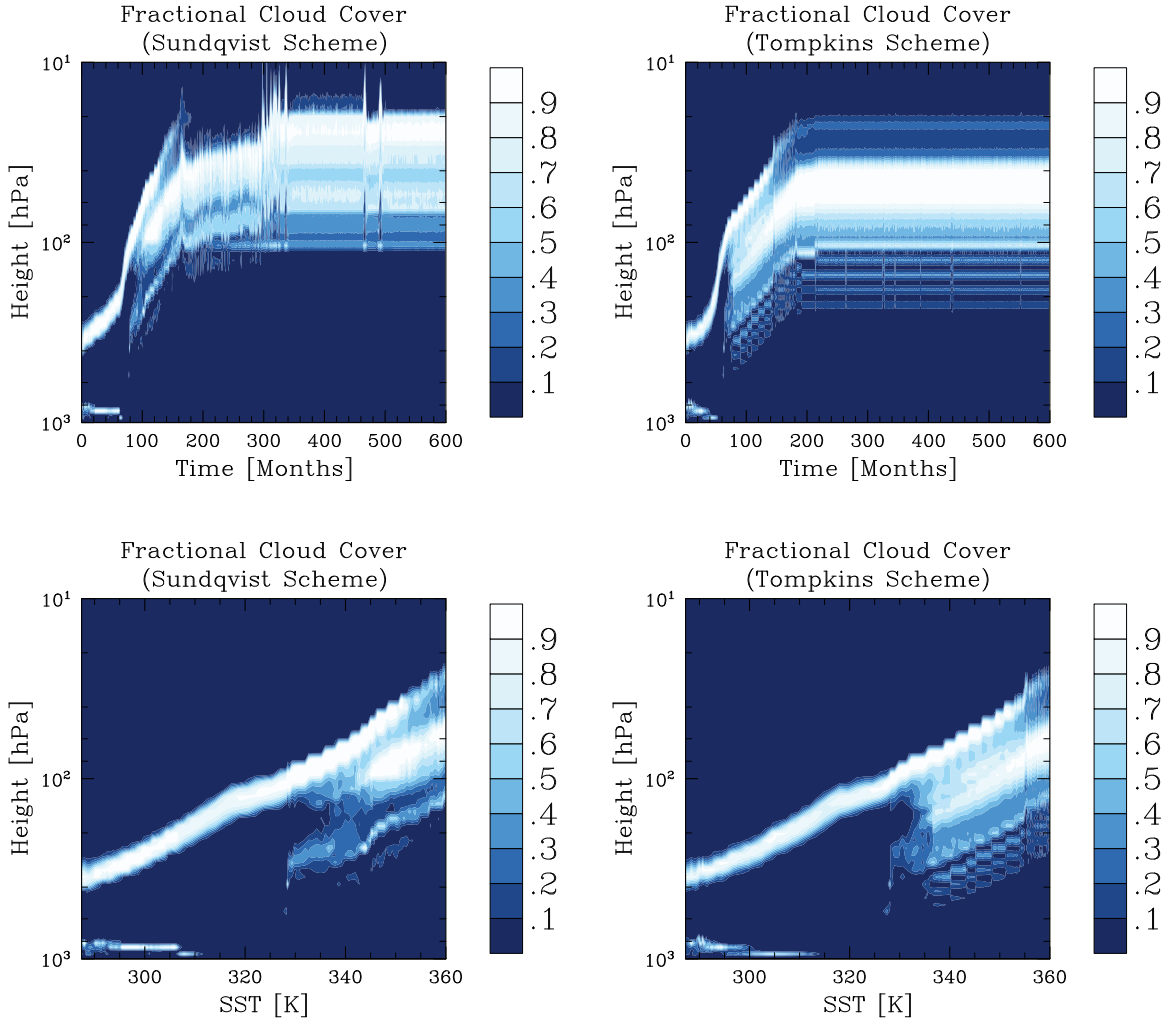


Figure 2.6: The upper panels show the temporal evolution of fractional cloud cover as a function of time and height (in terms of pressure of dry air) for a simulation with a cold start ( $SST_{ini} = 286.8$  K) for a TSI of  $1.45 S_0$  for the Sundqvist scheme (left) and the Tompkins scheme (right). The lower panels show the fractional cloud cover of the same simulations plotted against the SST up to 360 K for the Sundqvist scheme (left) and the Tompkins scheme (right).

up to where the temperature falls to 220 K. The clouds tend to be concentrated into two layers, but this information is largely lost in the temporal average. The largest density of cloud condensate occurs at a temperature of around 280 K in the warm state (Figure 2.5), but the density of cloud condensate remains larger than  $10^{-5}$  kg /  $m^3$  up to levels where the temperature falls below 240 K. As a consequence, the OLR is smaller (around  $180 \text{ W m}^{-2}$  on average) in this warm state compared to the cold state. The total amount of cloud condensate is larger, which tends to make the clouds more reflective (Figure 2.8). Furthermore, the cloud condensate is distributed over a relatively large vertical extent, and as a consequence the cloud droplets remain relatively small, which increases the albedo of the clouds even further.

All but two simulations with a warm start terminate in the warm regime. The clouds in these simulations are thus very similar to the ones with a cold start that end up in the warm regime (not shown). The clouds remain confined to a range of temperature between 220 K and 300 K, but the total amount of cloud condensate decreases with decreasing TSI (Figure 2.8), and hence the albedo decreases (Figure 2.4). The OLR, however, remains nearly constant at a value of around  $180 \text{ W m}^{-2}$ .

### **FSC with the Tompkins scheme**

In all simulations with a cold start with the Tompkins scheme that remain in the cold regime, the clouds evolve similarly to the ones produced by the Sundqvist scheme (Figure 2.5), that is, the albedo increases with TSI due to an increase in fractional cloud cover and cloud condensate at the boundary layer. However, the picture is different for simulations that terminate in the warm regime. Cloud condensate forms at temperatures of up to 340 K and hence at higher temperatures than for the Sundqvist scheme. Condensate may form even at higher temperatures in some very few instances. The total amount of cloud condensate in the warm regime is much larger and more scattered than for the Sundqvist scheme (Figure 2.8), which does, however, not lead to different values of the albedo (Figure 2.4). This can be partly explained by the small fractional cloud cover of the clouds at temperatures higher than around 300K (Figure 2.5), which implies that in this region the super-saturation is small. However, even weak super-saturation may lead to a considerable amount of condensate at large temperature because of the exponential dependence of the water-vapor-saturation pressure on temperature.

The cloud top is located at a similar temperature as in the Sundqvist case (around 220 K) and hence the OLR is similar (around  $180 \text{ W m}^{-2}$  on average) as well, although the spread between simulations is larger than for the Sundqvist scheme. The structure of the clouds produced by the Tompkins scheme is not as homogeneous across simulations as with the Sundqvist scheme, and furthermore the structure evolves less smoothly with increasing TSI. We will address these issues in the discussion. In simulations with the Tompkins scheme the transition from the cold regime to the warm regime is caused similarly to the Sundqvist scheme by the decrease in relative humidity at the top of the boundary layer (not shown), which causes the clouds at the boundary layer to vanish (Figure 2.6). Eventually the shortwave effect outweighs the longwave effect of the clouds that form in the upper troposphere in the warm climate (Figure 2.7).

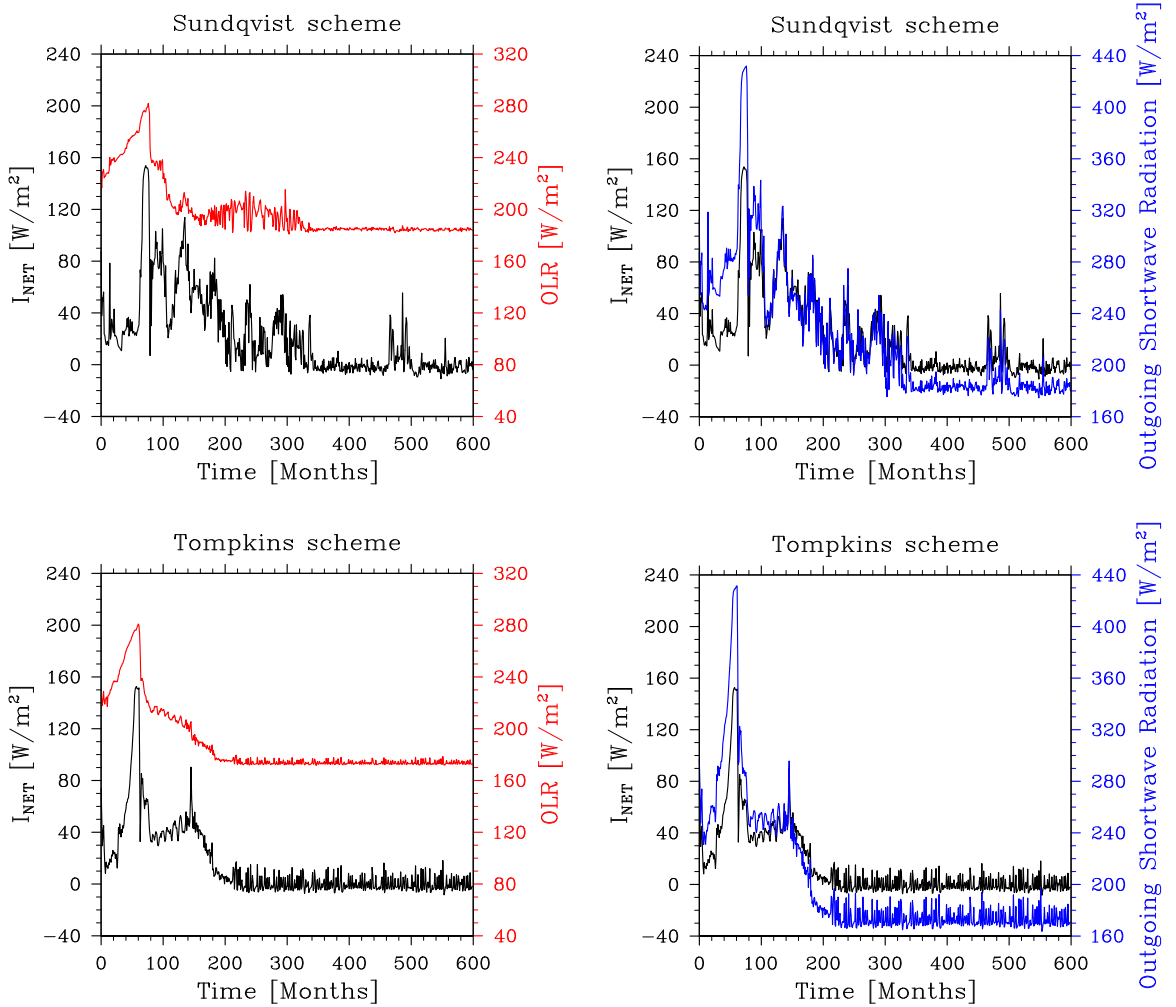


Figure 2.7: Temporal evolution of the radiative imbalance at the top of the atmosphere ( $I_{NET}$ , black line) against the OLR (left panels, red line) as well as against the net outgoing shortwave radiation (right panels, blue line). The panels on the top show the results of one simulation with a cold start ( $SST_{ini} = 286.8$  K) for a TSI of  $1.45 S_0$  for the Sundqvist scheme and the lower panels show the result of a simulation with the same initial SST for the same TSI but for the Tompkins scheme. The simulation for the Sundqvist scheme and the one for the Tompkins scheme are the same as the ones shown in Figure 2.6.

All complete simulations with a warm start terminate in the warm regime. The clouds form generally in the range of temperatures between 220 K and 340 K, and the albedo decreases with decreasing TSI (Figure 2.4). However, despite a tendency of the cloud condensate to decrease with decreasing TSI as well (Figure 2.8), changes in the cloud structure also contribute to the decrease in albedo with decreasing TSI (not shown). The exact behavior of clouds in the Tompkins scheme is difficult to understand, a point which we will address in the discussion.

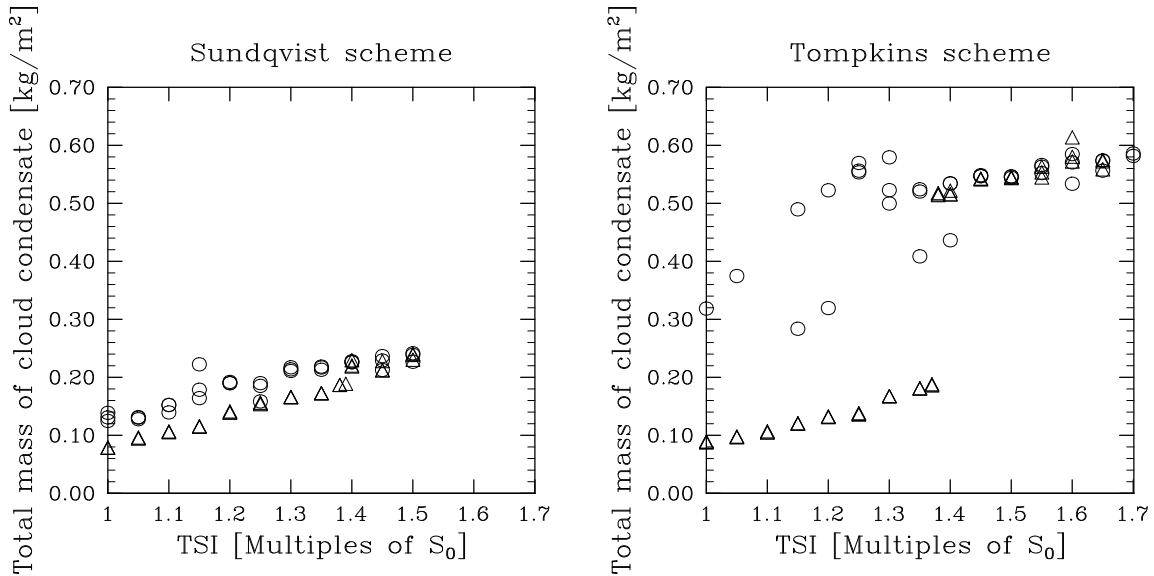


Figure 2.8: Temporal mean of the vertically integrated mass of cloud condensate over the last five years of simulation as a function of TSI for FSC with the Sundqvist scheme (left panel) and FSC with the Tompkins scheme (right panel). Triangles indicate that the initial SST was below 290 K, and circles indicate that the initial SST was between 380 K and 385 K for CSC and with the Sundqvist scheme, and between 360 K and 365 K with FSC and with the Tompkins scheme. There are no marks for simulations in which a Runaway Greenhouse occurs.

### 2.4.3 Summary

It stands out that the critical TSI to trigger a Runaway Greenhouse is markedly higher for FSC than for CSC. This is true for the Sundqvist scheme, but even more so for the Tompkins scheme. The critical TSI is in the range of 1.10 - 1.13  $S_0$  for CSC with initial SSTs in the 280's K and 1.05 - 1.10  $S_0$  for initial SSTs in the range of 382 - 385 K. The critical TSI for FSC with the Sundqvist scheme is in the range of 1.50 - 1.55  $S_0$ , with multiple equilibria occurring for a wide range of TSI (1.00  $S_0$  to 1.39  $S_0$ ). The results for FSC with the Tompkins scheme are qualitatively similar to the ones obtained with the Sundqvist scheme, but the critical TSI is larger (1.65 - 1.70  $S_0$ ), the SSTs in warm states are lower (360 - 375 K, compared to 360 - 390 K for the Sundqvist scheme), and for TSIs of 1.15  $S_0$  and 1.20  $S_0$  we find three equilibria.

The simulations with FSC show that it is exclusively the increased cloud albedo that prevents a Runaway Greenhouse to occur for large values of TSI. This is true for both the Sundqvist scheme and the Tompkins scheme. Clouds become increasingly optically thick with increasing TSI, which causes the cloud albedo to increase as well. In the warm regime, clouds occur in a well-defined range of atmospheric temperature

in the upper troposphere, irrespective of the TSI. This range is, however, different for the Tompkins scheme and for the Sundqvist scheme. The climate transition from the cold to the warm climate is caused by the disappearance of clouds at the top of the boundary layer, which causes a temporary drop in the albedo.

## 2.5 Discussion

### 2.5.1 Boundary layer clouds

The results show that both fractional cloud cover and cloud condensate at the top of the boundary layer first increase with TSI (Figure 2.5). As a critical TSI is attained, both cloud cover and cloud condensate at the top of the boundary layer decrease with increasing SST and these clouds eventually vanish (Figure 2.6)). We discuss here why our model exhibits this behavior and compare our results to the literature.

The moisture content in the boundary layer increases with the SST; the relative humidity at the top of the boundary layer increases as well, and so do the fractional cloud cover and the amount of cloud condensate. The increase in moisture content (and temperature) causes the moist static energy to increase faster in the boundary layer than in the layers above. Hence, the stability across the boundary layer decreases, and convection exports moisture out of the boundary layer with increasing intensity, which causes the relative humidity at the top of the the boundary layer to decrease. This in turn eventually leads to the disappearance of the clouds. As the albedo drops and strong surface heating occurs, the convection becomes strong enough to temporarily destroy the boundary layer. This mechanism explains not only the behavior of clouds in our model but also the dependence of the disappearance of the clouds on the temperature (the clouds disappear always at SSTs of around 310 K), since the moist static energy depends on moisture and hence on temperature rather than it does on the applied forcing. Furthermore it is not surprising that both cloud-cover schemes show a similar behavior, since the disappearance of clouds is caused by the increasing moisture export by the convection scheme.

The boundary-layer clouds in our model can best be compared to boundary-layer clouds at low latitudes, since the large-scale motions are less important there than at higher latitudes. Model simulations have shown both increase and decrease of low clouds at low-latitudes with increasing temperature (Bony et al., 2006), but Clement et al. (2009) infer from the analysis of observations and model results of the north-eastern Pacific that the low-latitude low-level clouds decrease with increasing temperatures. We can, however, not conclude that the mechanisms at work would lead to the complete disappearance of boundary-layer clouds as in our model. Briert and Bony (2013) suggest that the decrease in low-level clouds produced by the IPSL-CM5A general circulation model with increasing temperature is triggered by a decrease of the vertical gradient of moist static energy, which leads to dry air being mixed into the boundary layer in low-latitude subsidence regions and hence to a drying. The decrease

of the gradient of moist static energy also causes the cover of low clouds to decrease in our model, but the mechanism for the decrease is different, since our one-dimensional model cannot simulate the drying of the boundary layer in the subsidence regions. If the process of Brient and Bony (2013) is indeed responsible for a decrease in low-level clouds, then this decrease should not occur as abruptly as in our model. The simulations of Boer et al. (2005) show only little changes in cloud cover and albedo for a TSI of up to  $1.15 S_0$ , but both total cloud cover and albedo decrease in the simulation with  $1.25 S_0$ . However, the fractional cover of boundary-layer clouds does not change substantially in their study.

The value of TSI necessary to make the boundary-layer clouds disappear is large in our model (around  $1.4 S_0$ ). However, the annual average of net solar irradiance on present-day Earth at the equator is more than 20 per cent larger than the global average. Therefore our results suggest that a TSI of  $1.15 S_0$  would be sufficient to lead to the disappearance of the boundary-layer clouds at the equator. Such an extrapolation is obviously too simplistic, but it serves as a reminder that low-level boundary layer clouds on an Earth-like planet may disappear at a lower TSI than our results may at first suggest.

## 2.5.2 Clouds in the warm regime

A warm atmosphere is expected to be moist, and therefore convection should lead to the formation of clouds in most of the troposphere. Our results show that indeed thick clouds form in the troposphere, but only within a well-defined range of temperatures. We will present physical arguments for the clouds to form in a confined temperature range and discuss the implications of this behavior in the next two subsections .

### **The impact of the shortwave and the longwave effect of clouds in the warm regime**

Our results show that the shortwave effect of clouds dominates their longwave effect as thick clouds form in the warm regime. There are two reasons for this to occur. First, the longwave absorption saturates faster with the mass of cloud condensate than does the cloud albedo (Pierrehumbert, 2010). If there is enough cloud condensate to make a cloud act like a blackbody, a thickening of the cloud has no further effect on the OLR, but the reflected shortwave radiation would still increase. The clouds contain sufficient condensate in the warm regime to act as a blackbody in all our simulations.

Second, there is a lower limit to the emission temperature of clouds. This is important because the longwave cloud-radiative effect could outweigh the shortwave cloud-radiative effect if optically thick clouds were to form at ever lower temperatures, which would cause the emission temperature to decrease as well. But since the mass of possible condensate depends on temperature through the Clausius-Clapeyron relation, clouds become optically thin below a certain temperature, and hence the emission temperature of clouds has a lower bound. This is supported by our results since there is very little cloud condensate below 220 K. The emission temperature in the simulations with clouds therefore does not fall below 235 K and varies only little. This is even true in experiments where we removed the ozone from the atmosphere and hence the temperature at the tropopause falls below 200 K (not shown). The mechanism involved here is similar to the fixed anvil temperature theory (Hartmann and Larson, 2002), in that the emission temperatures do not change for a wide range of TSI in our study.

We can illustrate that the OLR is nearly constant in the warm state by solving the radiative balance at the top of the atmosphere Eq. (2.1) for  $S$ . For a prescribed OLR, we obtain the effective albedo as a function of TSI. We have added this function to Figure 2.4 (upper curve) for one constant value of OLR (obtained in the warm regime) for both the Sundqvist scheme and the Tompkins scheme. The curves give a very good fit to the results obtained for both the Sundqvist scheme and the Tompkins scheme and highlight that the OLR is independent of the cloud thickness and hence of the albedo in the warm state. Optically thick clouds form at the top of the boundary layer in the cold regime, and hence the OLR is larger than in the warm regime. Compared to the cold regime, there is thus a larger longwave cloud forcing in the warm regime. But once the maximum longwave cloud forcing is attained in the warm regime because the clouds form in the upper troposphere, any increase in cloud condensate will have an effect on the shortwave radiation only, and eventually the shortwave effect of the clouds dominates their longwave effect.

### **Suppression of cloud formation in the optically thick region of the atmosphere**

With the Sundqvist scheme and equilibrium SSTs in the warm regime, the relative humidity exceeds the threshold value for cloud formation in most of the troposphere. Nonetheless cloud condensate never forms where the water vapor density exceeds  $0.05 \text{ kg m}^{-3}$ . We now give an explanation why we would expect clouds not to form in the regions of the atmosphere where water vapor is abundant. The explanation is based on an argument by Renno (1997) for the behavior of convection. He argued that

the warm and hence optically thick region in the lower atmosphere must be close to saturation. The radiative cooling tends to zero in this region, due to the high opacity. In equilibrium the convective downdraft must therefore be saturated to compensate the saturated convective updraft. We can also apply the argument to condensation: In the regions of the atmosphere where, due to high opacity, radiative cooling is ineffective, condensation heat cannot be effectively dissipated. Therefore the condensation heat will cause re-evaporation of the condensate and hence suppress cloud formation. We can, however, not establish whether this effect is the only cause for the suppression of cloud formation.

Cloud condensate forms with the Tompkins scheme at locations where the water vapor densities are as high as  $0.5 \text{ kg m}^{-3}$  and which hence are in the optically thick region of the atmosphere. But the fractional cloud cover is small in the regions where the water vapor density is high, and furthermore the density of cloud condensate decreases with increasing water vapor density. The maximum specific amount of cloud condensate is found at water vapor densities similar to the ones for simulations with the Sundqvist scheme. So even though we cannot conclude with certainty that the above mechanism is at work in simulations with the Tompkins scheme, the small amount of cloud condensate and the small fractional cloud cover suggest that condensation is suppressed in the optically thick region in simulations with the Tompkins scheme as well.

### 2.5.3 Unusual behavior of the Tompkins scheme

The Tompkins scheme exhibits some unusual behavior in the warm regime. The simulations with a warm start, for example, end up in different states despite the very similar initial conditions for a TSI of  $1.15 S_0$  and  $1.20 S_0$ . The Tompkins scheme is much more likely to produce sharp bifurcations than the Sundqvist scheme, because the function to determine cloud cover is not just dependent on relative humidity, but also on inputs from other components of the hydrological cycle. For example, if only the surface temperature is slightly changed but all other variables remain unchanged, the Sundqvist scheme would just diagnose the same cloud cover as before and return to the same state. By contrast, in the Tompkins scheme this small change in surface temperature may suffice to cause a change in convective activity and to directly alter the clouds, which in turn would again have an influence on the column's climate. Due to this large sensitivity, the detailed behavior of the Tompkins scheme is sometimes difficult to understand. Furthermore, a checkered pattern of cloudy and cloud-free levels in the warm regime occurs in some simulations (for example in Figure 2.6). We

---

performed simulations with a reduced timestep, in order to assess whether such behavior is a problem of numeric stability. The outcome of these simulations is, however, no different, and hence the behavior appears not to be a consequence of numeric instability. Note that the qualitative behavior of the Tompkins scheme is similar to the one of the Sundqvist scheme and that this behavior can also be physically explained, even if the interpretation of some details is difficult.

## 2.6 Comparison to previous studies

Kasting (1988) studied an Earth-like atmosphere under strong solar forcing with a radiative-convective model. He considered temperatures as high as 1600 K, but at the price of prescribing the temperature profile in his atmosphere. Clouds were included only for a single case with a surface temperature of 640 K. Kasting discussed the influence on the energy balance at the top of the atmosphere of a single cloud layer (with either 50% or 100% fractional cloud cover), located tentatively at different pressures. He found that the longwave effect is small irrespective of the location of the cloud layer, but that the shortwave effect is very important in this warm state. This is in agreement with the results we obtain for the equilibria in the warm regime for both cloud schemes, even though the surface temperatures are much lower than in Kasting's case. The magnitude of the effect of the cloud albedo on the critical TSI is, however, much larger in Kasting's study.

Our results with CSC can be easily compared to the ones by Renno et al. (1994). They tested the influence on the critical solar irradiance of different convection schemes embedded in a radiative-convective model. Their radiation scheme was non-gray and included solar absorption, but no cloud radiation. They showed that depending on the convection scheme a critical solar irradiance of between  $1.10 S_0$  and  $1.41 S_0$  was necessary to trigger a Runaway Greenhouse. In the present study, a value of TSI in the range of  $1.10 - 1.13 S_0$  is sufficient to trigger a Runaway Greenhouse. Hence, for CSC the value of critical TSI found in our study lies within the range found by Renno et al. (1994), but rather on the low side. In the experiments with a fixed cloud cover, Renno et al. (1994) found that the critical solar irradiance was increased compared to CSC for all convection schemes. Hence their results are in agreement with ours, even though the critical TSI is larger in our study than in that by Renno et al. (1994). Due to missing information we cannot compare the change in magnitude of critical solar irradiance between CSC and fixed cloud cover in their study. However, it is not surprising that we obtain higher values for the critical TSI, because Renno et al. (1994) prescribed the shortwave optical properties according to present-day satellite observations, whereas the clouds become more reflective (than they are at present) with larger SSTs and larger TSIs.

Similar to Renno (1997), we find a range of TSI for which multiple equilibria are possible. The strong greenhouse effect of water vapor allows equilibria at high SSTs even when the TSI is close to the present-day value. This is true for all simulations, although there are some caveats for CSC, because of the leakage of energy. However, the simulations with FSC show that the range for which multiple equilibria exist is extended

to much higher values of TSI if the optical properties of the clouds are included.

In the study by Boer et al. (2005), the model went into a Runaway Greenhouse for a TSI of  $1.35 S_0$ . However, for this TSI their model crashed at a mean surface temperature increase of 50 K. The absolute value of the mean surface temperature hence did not exceed 340 K. The climate instability leading to the rising surface temperatures in the study of Boer et al. (2005) was caused by a decrease in cloud albedo, an effect which can also be temporally seen in our study. However, it remains unclear whether the cloud albedo would recover in this case as seen in our study.

Goldblatt et al. (2013) recently studied the Runaway Greenhouse with a state-of-the-art radiative-transfer model but without clouds. They conclude that a present-day Earth-like planet would be on the verge of a Runaway Greenhouse without clouds (assuming a surface albedo of 0.12) and that therefore the net cooling effect of clouds (together with sub-saturation) keeps Earth from going into a Runaway Greenhouse. Our results suggest that this holds true even for much larger values of TSI.

Several studies (e.g. Colman (2003), Bony et al. (2006), Soden et al. (2008)) have analyzed and discussed the cloud radiative forcing and the cloud feedback obtained by various GCM simulations with increased atmospheric  $\text{CO}_2$  concentrations. Depending on the GCM, the change in the cloud-radiative effect can be positive or negative, but the change is positive in most cases. Since we impose a much stronger radiative forcing, the results may look different again in our case. Especially in much warmer climates than the one on present-day Earth we expect the cloud feedback to be negative, as previously discussed.

## 2.7 Implications for Venus

We discuss here the possible implications of our results for early Venus. Due to the simplicity of our model such comparisons are, however, to be taken with caution. Measurements of the ratio of deuterium to hydrogen in the Venusian atmosphere suggest that early Venus may have held much more water than it does today (Donahue et al., 1982). The TSI on early Venus is expected to have been between  $1.34 S_0$  and  $1.43 S_0$  (Newman and Rood, 1977). If we apply our values of the critical TSI ( $> 1.50 S_0$ ) to early Venus, we find that Venus would not have gone into a Runaway Greenhouse, but that early Venus would have been either in a climate close to the present-day Earth climate or in the warm regime with SSTs in the 380's K (360 K for the Tompkins scheme). Either way, Venus would ultimately have gone into the warm regime as the TSI increased with time. These equilibria are in a range of temperatures that Kasting et al. (1984) called the Moist Greenhouse state. According to Kasting et al. (1984), the moist stratosphere in this state is susceptible to photo-dissociation of water vapor and to hydrogen escape. In our simulations the stratosphere remains dry for the duration of the simulations, despite the high SSTs. Stratospheric water concentrations increase linearly by means of diffusion through the tropopause, but only at a rate of  $10^{-11}$  kg/kg per year. On a planet the moistening of the stratosphere would occur faster than in a column, because large-scale dynamics such as the Brewer-Dobson circulation would mix water more efficiently into the stratosphere. If the stratosphere became wet in our model, our results would support the idea by Kasting et al. (1984) that Venus could have lost its water without going into a Runaway Greenhouse. Given the range of critical TSI found in our model, if Venus did not lose its water sufficiently fast in the Moist Greenhouse state, the planet would have gone into a Runaway Greenhouse.

## 2.8 Conclusions

Based on our simulations with a single-column version of the general circulation model ECHAM6, we conclude:

1. Clouds provide a strong negative feedback and hence increase substantially the critical total solar irradiance that is necessary to trigger a Runaway Greenhouse. The critical value is increased from 1.10-1.13  $S_0$  for clear-sky conditions (clouds are transparent to radiation) to 1.50-1.70  $S_0$  for full-sky conditions (clouds are radiatively active).
2. Clouds enlarge the range of total solar irradiance for which a double equilibrium is possible: Additionally to states with near-present-day sea surface temperatures, warm states exist with sea surface temperatures larger than 360 K.
3. The outgoing longwave radiation has attained a minimum in the warm state. Therefore, a further thickening of clouds increases only their shortwave effect. This mechanism allows the column to remain in balance for large values of total solar irradiance.



## Chapter 3

# Climate instabilities on an Earth-like planet under strong solar forcing

A modified version of the general circulation model ECHAM6 is used to investigate the impact of increased total solar irradiance (TSI) on a  $0^\circ$ -obliquity aqua-planet on a present-day Earth-like orbit. We find that the present-day Earth-like climate destabilizes for a TSI between 1.06 and 1.08 times the present-day Earth value ( $S_0$ ) because of a positive cloud feedback. The aqua-planet does not, however, go into a Runaway Greenhouse, but attains a new steady state with global-mean sea-surface temperatures exceeding 335 K. The cloud feedback becomes negative as the global-mean sea-surface temperature exceeds 330 K, which leads, together with the increased outgoing long-wave radiation at high latitudes, to a new steady state. As the TSI is further increased, the planet remains in the same regime of warm steady states for TSIs of at least up to  $1.2 S_0$ , because the cloud albedo increases as well and balances the increasing forcing. These warm states are characterized by a low meridional temperature gradient, a weak meridional circulation without polar cells, a moist stratosphere, and convection-dominated cloud formation. The volume mixing ratio of water vapor in the upper atmosphere attains values as large as 0.015. This large mixing ratio suggests that a planet in such a warm state would be subject to a rapid loss of water. Applied to Earth, our results suggest that, assuming an increase of TSI of 9 % per billion years, the planet's climate will remain in a present-day like state for another 650 to 880 million years before going into the warm regime of steady states where it will remain for at least another one billion years.

### 3.1 Introduction

In the course of stellar evolution, water-rich planets such as Earth are expected to lose most of their water inventory as the total solar irradiance (TSI) increases beyond a certain threshold. For an Earth-like planet, previous studies with one-dimensional radiative-convective models have established two different paths that could lead to the loss of an ocean of water termed Runaway Greenhouse and Moist Greenhouse. There were, however, only a few studies with three-dimensional models on this topic, and none of these could conclusively determine which of the two mechanisms would lead to the loss of water. Therefore, we investigate the fate of an Earth-like aqua-planet for values of TSI larger than the value on present-day Earth.

The Runaway Greenhouse is a process in which strong solar forcing leads to a water-vapor feedback-loop, which ultimately leads to the evaporation of all oceans on a water rich planet (Gold (1964), Komabayashi (1967), Ingersoll (1969)). As the water would then reach very high in the atmosphere, it could be easily photo-dissociated by ultra-violet radiation and the resulting hydrogen could escape to space.

Water could also be lost in a regime of steady states called Moist Greenhouse, even though a liquid ocean is still present at the surface (Kasting et al., 1984). The Moist Greenhouse emerges, because the cold trapping of water vapor becomes less and less effective as the surface temperature rises and the tropopause climbs to lower and lower pressures (Kasting et al., 1984). The minimum water vapor mixing ratio in the upper atmosphere necessary to lose an Earth-like ocean within the age of Earth is estimated to be around  $3 \times 10^{-3}$  (Kasting et al., 1993), which we consider here to be the limit for the Moist Greenhouse. The Moist Greenhouse emerges from a present-day Earth-like state along a trajectory of steady states as the surface temperature increases to about 340 K (Kasting (1988), Kopparapu et al. (2013)). Unlike for a Runaway Greenhouse, a planet that loses its water in a Moist Greenhouse would remain habitable; that is, liquid water would be stable on the surface until most of the water is lost.

A planet in a Moist Greenhouse might transform into a dry but habitable land planet, because the stratosphere becomes dry again if water becomes scarce at the surface (Abe et al., 2011). In this case the planet would remain habitable for an even longer time, before the remaining water evaporates in a Runaway Greenhouse. However, whether a planet goes into a Moist Greenhouse depends crucially on the maximum surface temperature for which a steady state can exist before the planet goes into a Runaway Greenhouse. This maximum equilibrium temperature in turn depends on the background atmosphere and on the assumptions made on albedo and

thus on clouds (e.g. Kasting (1988), Goldblatt et al. (2013)). A Runaway Greenhouse can also be triggered while a planet is in the Moist Greenhouse regime (e.g. Kasting (1988), Abe et al. (2011)). The possible paths leading to a loss of water are sketched in Figure 1.1 (which is located in the introduction of the thesis).

In Chapter 2 we have investigated the influence of clouds on the critical TSI for the onset of a Runaway Greenhouse with a one-dimensional radiative-convective equilibrium model, and have found that clouds increase substantially the critical TSI, compared to clear-sky calculations (where clouds are considered to be transparent to radiation). Furthermore, only if clouds are included in the radiative transfer calculations, does the atmosphere go into a warm steady state. The transition to such a state occurs for TSI between 1.37 to 1.40 present-day TSI on Earth ( $S_0$ ). Unlike previous studies, the transition occurs due to a climate instability. Depending on the applied cloud scheme, the system would remain in a warm state at least up to TSIs of 1.50 to 1.70  $S_0$ . However, the stratosphere remains dry in these states, which we attribute to the lack of a strong mechanism in a one-dimensional model to mix water effectively into the stratosphere. The representation of clouds is difficult in a one-dimensional model, since, for example, cloud formation through large-scale advection cannot be represented. So even though the work with the single-column model gives some insight into the influence of clouds on the climate system under strong solar forcing, only a general circulation model (GCM) can simulate the interaction between circulation and clouds which is fundamental to assess the influence of clouds on the climate system (Stevens and Bony, 2013).

Previous studies on Earth-like planets with GCMs under increased solar forcing either did not contain any representation of clouds (Ishiwatari et al. (2002), Ishiwatari et al. (2007)), or only considered global-mean surface temperatures of less than 340 K (Boer et al., 2005). However, these studies found that a climate instability leads to a runaway of the global-mean surface temperatures well below the aforementioned threshold for a Moist Greenhouse. Ishiwatari et al. (2002) and Ishiwatari et al. (2007) attributed this runaway behavior to a limitation of thermal emission (as a consequence of the runaway water-vapor feedback), whereas a reduction of cloud cover caused the same behavior in Boer et al. (2005).

Abe et al. (2011) performed simulations with a GCM of a dry land-planet for different TSIs. Even though they also performed simulations with an aqua-planet, the results of the aqua-planet simulations were only briefly discussed, the evolution of clouds was not presented and the maximum equilibrium temperature not mentioned. In summary, it is presently unclear whether a climate instability occurs before a Moist

Greenhouse is attained or not, whether such a climate instability is caused by a decrease of cloud cover or by a runaway water vapor feedback, and whether such a climate transition would necessarily lead to a Runaway Greenhouse.

To tackle these points, we use a modified version of the GCM ECHAM6 on a  $0^\circ$  obliquity aqua-planet. Our model uses the same interactive representation of clouds as the single-column model used in Chapter 2, with a prognostic scheme for cloud microphysical properties and a diagnostic scheme for the representation of fractional cloud cover. Furthermore, our model runs to temperatures of up to 350 K (and hence to higher temperatures than the model of Boer et al. (2005)), which is a posteriori sufficient for the task at hand.

This chapter is organized as follows. In Section 3.2 we give a description of the model and of the experimental setup. Then we present the results of the steady-state and transient behavior of our model (Section 3.3). In Section 3.4 we discuss the limitations of the model and give a physical interpretation of some of the results. A comparison to previous work is presented in Section 3.5 and the implications of our results for planetary science are discussed in Section 3.6. Finally we state the main conclusions drawn from this Chapter (Section 3.7).

## 3.2 Experimental design

### 3.2.1 Model

We employ a modified version of the GCM ECHAM6 (Stevens et al., 2013) in an aqua-planet setting in which the whole surface is covered by a 50 m deep mixed-layer ocean. We run the model with a spectral truncation of T31, which corresponds to a Gaussian grid with a grid-point spacing of  $3.75^\circ$ . The atmosphere is resolved vertically by 47 layers up to a pressure (of dry air) of 0.01 hPa. The oceanic heat transport is prescribed by a sinusoidal function of latitude. There is no representation of sea ice in our model, and as a consequence water may be colder than the freezing temperature. We neglect the sea ice, because we can then more readily compare our model to its single-column version used in Chapter 2. Besides practical advantages, the missing sea-ice albedo feedback makes the driving mechanisms for a possible climate transition easier to understand. This does not affect the conclusions we draw in this study, as we will explain in the discussion. The orbit of the aqua-planet is perfectly spherical with a radius of 1 AU. The obliquity of the aqua-planet is  $0^\circ$ . For simplicity, a year is set to be 360 days, and hence the planet moves slightly too fast on its orbit. But due to the perfect symmetry of the orbit of the planet, the results are not affected, since the daily cycle remains constant over time. The rotation velocity of the aqua-planet corresponds to present-day Earth.

The hydrological cycle of our model is similar to the single-column version thereof used in Chapter 2, except that water (in all phases) can be transported horizontally by the means of advection and diffusion. Water is added to the atmosphere by surface evaporation and is then vertically distributed by advection, convection, and vertical diffusion. The convection scheme is a mass-flux scheme for cumulus convection (Tiedtke, 1989), with modifications for the deep convection according to Nordeng (1994). Water leaves the atmosphere system through convective and large-scale precipitation as well as by condensation at the surface, and as a result of snow melt. In ECHAM6 water (in all phases) is advected as a tracer. However, since the transport equations in ECHAM6 are formulated in sigma pressure coordinates, interpolation between pressure levels is required for the transport between grid points, a scheme that leads to a violation of the mass conservation of tracers. As a consequence, water is not fully conserved in our model; we will discuss the implications thereof later.

Stratiform clouds are represented by the scheme proposed by Sundqvist et al. (1989), which is standard in ECHAM6. This scheme consists of prognostic equations for the vapor, liquid, and ice phases, and a diagnostic cloud cover scheme. We give only a short

summary of the scheme here; for more details please refer to Lohmann and Roeckner (1996). Fractional cloud cover is parametrized as an empirical function of relative humidity  $r$  at each layer of the column. For  $r > r_0$ , where  $r_0 < r_{sat}$  is a subgrid-scale condensation threshold and  $r_{sat}$  is the relative humidity of saturation ( $= 1$  in general), condensational growth of cloud droplets occurs. The threshold  $r_0$  is a function of pressure and decreases from  $r_0(p_{surf}) = 0.9$  at the surface to  $r_0(p \approx 500 \text{ hPa}) = 0.7$  and remains constant at 0.7 above about 500 hPa. The empirical nature of the equations may raise questions about the justification of the threshold value  $r_0$  in a climate much warmer than the one of present-day Earth. However, given the very different conditions found on different places on present-day Earth, the prescribed profile of  $r_0$  appears to be a sound choice for a large range of temperatures.

For the radiative calculations we use the modified version of the Rapid Radiative Transfer Model (RRTMG) (Mlawer et al. (1997), Iacono et al. (2008)) described in Chapter 2. The modifications consist of the exponential extrapolation up to 400 K of all molecular absorption coefficients for long-wave calculations and of the self-broadened water-vapor continuum for the shortwave calculations, and of the introduction of the self-broadened water-vapor continuum above 95 hPa. In order to be able to run the model at high temperatures, we introduce the same modifications to the grid-point physics as in the single-column version of the model (see Chapter 2 and Appendix A.1). The pressure effects of water vapor are not considered for the horizontal transport. However, the pressure effects of water vapor are included in the grid-point calculations (except for the radiative transfer calculations), which comprise the surface exchange, the vertical diffusion, the gravity-wave drag parametrization, the radiative heating, the convection, and the cloud calculations. Hence the model can be characterized as a hybrid model, with water vapor adding to the total pressure for local effects but not so for the large-scale transport.

In addition to the changes introduced to the single-column version of the model, several more modifications are necessary for our three-dimensional model to run stably at high temperatures. The temperature tendency due to condensation/evaporation has been limited to 30 K per timestep, since condensation/evaporation may lead to exaggerated temperature tendencies, because the condensation algorithm does not always converge in the case of strong supersaturation. Furthermore, the convective mass-flux is downscaled if the resulting temperature tendency at any level exceeds 3 K per minute or the wind tendency exceeds 3 m per minute. The radiative transfer calculations are performed every 24 minutes instead of every 2 hours as standard, in order to avoid unrealistic radiative heating by very high clouds. We encountered problems with resolved waves propagating to the top levels of the model, where their amplitude grows

and where they may be reflected. In order to avoid frequent model failure due to these effects, we reduce the model time step from the default of 15 minutes to 6 minutes and we introduce Rayleigh friction to vorticity and divergence as well as increase the horizontal diffusion in the top 8 layers (above around 1.5 hPa). The time constant of the Rayleigh friction is  $(8 \text{ d})^{-1}$  at the eighth layer and is increased by a factor of 3.2 per layer towards the top and is hence increased by a factor of 11000 in the top layer. The horizontal diffusion is increased by a factor of 3.2 per layer starting at the eighth layer from the top. The values of the time constant of the Rayleigh friction and horizontal diffusion are determined by trial and error. Since we investigate a large range of climates, it is difficult to find suitable values for these time constants and despite these modifications the model fails occasionally. In these cases, however, the runs can be continued by simply changing their trajectory, which is achieved by reducing the factor of multiplication per level for the Rayleigh friction from 3.2 to 3.199 for 30 days. In this setup the model can be run in a practical way to a TSI of up to  $1.2 S_0$ , which proves to be sufficient for the task at hand. Henceforth we will denote the combined effect of Rayleigh friction and increased horizontal diffusion as “sponge”.

Energy is not fully conserved in ECHAM6 and leads to an imbalance between the top of the atmosphere and the surface of between  $0.1$  and  $0.8 \text{ W m}^{-2}$  in temporal and global mean in steady states of reference experiments (Stevens et al., 2013). Therefore, we will calculate radiative forcings by subtracting the temporal and global mean of the top-of-the-atmosphere radiative imbalance of the unperturbed state from the radiative imbalance of the global mean of the top-of-the-atmosphere radiative imbalance of the perturbed state. We will state the magnitude of the imbalance of the different steady states we attain in our simulations in the discussion.

### 3.2.2 Experimental setup

We perform a total of seven experiments with different initial conditions and different values of TSI. The setup of the experiments is shown and explained in Figure 3.1. In total we apply five different values of TSI ( $1.00$ ,  $1.06$ ,  $1.08$ ,  $1.10$  and  $1.20 S_0$ ) and start simulations from a total of four different initial conditions. For TSIs of  $1.00$  and  $1.06 S_0$ , two simulations are performed in order to assess the range of steady states. Therefore, for each of these TSIs, one simulation starts from cold conditions and one simulation starts from warm conditions. In order to obtain statistics, all simulations run in steady state for 30 years except the one with a TSI of  $1.00 S_0$  with a warm start and the one with a TSI of  $1.08 S_0$ . In order to evaluate the influence of the sponge on the climate, we perform an additional experiment without sponge for present-day TSI, which we discuss in the appendix of this chapter.

### 3.3 Results

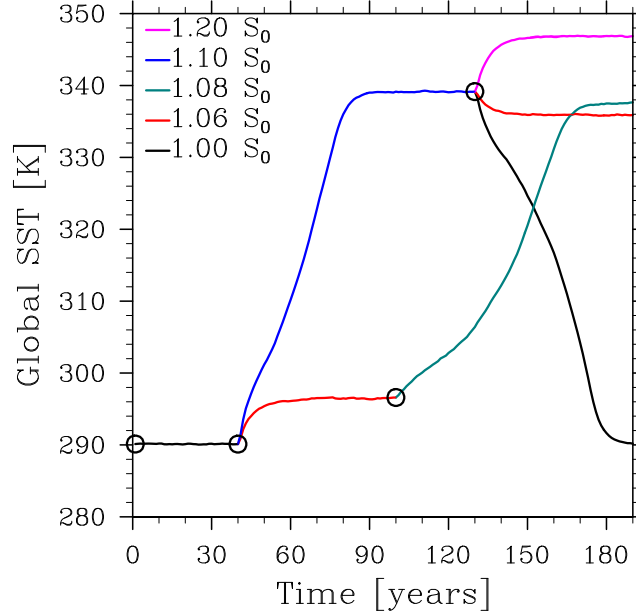


Figure 3.1: Annual mean of globally averaged SST against time in years. The circles denote the four states from which new simulations were started. For a TSI of  $1.0 S_0$  and  $1.6 S_0$  two simulations were performed.

#### 3.3.1 Steady states and double equilibria

The temporal evolution of the global-mean SST (gSST) of all simulations is shown in Figure 3.1. The results suggest that two different regimes of steady states exist. The gSSTs in the cold regime remain below 297 K and the equator to pole difference is larger than 45 K (Figure 3.2). The gSST in the warm regime is higher than 335 K, and the equator to pole difference is less than 10 K. The TSI required to trigger a climate transition from the cold regime to the warm regime lies between  $1.06 S_0$  and  $1.08 S_0$ . For a TSI of  $1.06 S_0$ , the aqua-planet remains in the warm regime for warm initial conditions and remains in the cold regime for cold initial conditions. Hence, at least two equilibria are possible for this value of TSI.

For the two simulations with a TSI of  $1.06 S_0$ , a comparison of the energetics in the cold and the warm regimes is straightforward, and hence we will focus on these two simulations to discuss the differences between the two regimes. In the warm state, the cloud albedo and the mass of cloud condensate are larger at low latitudes, while

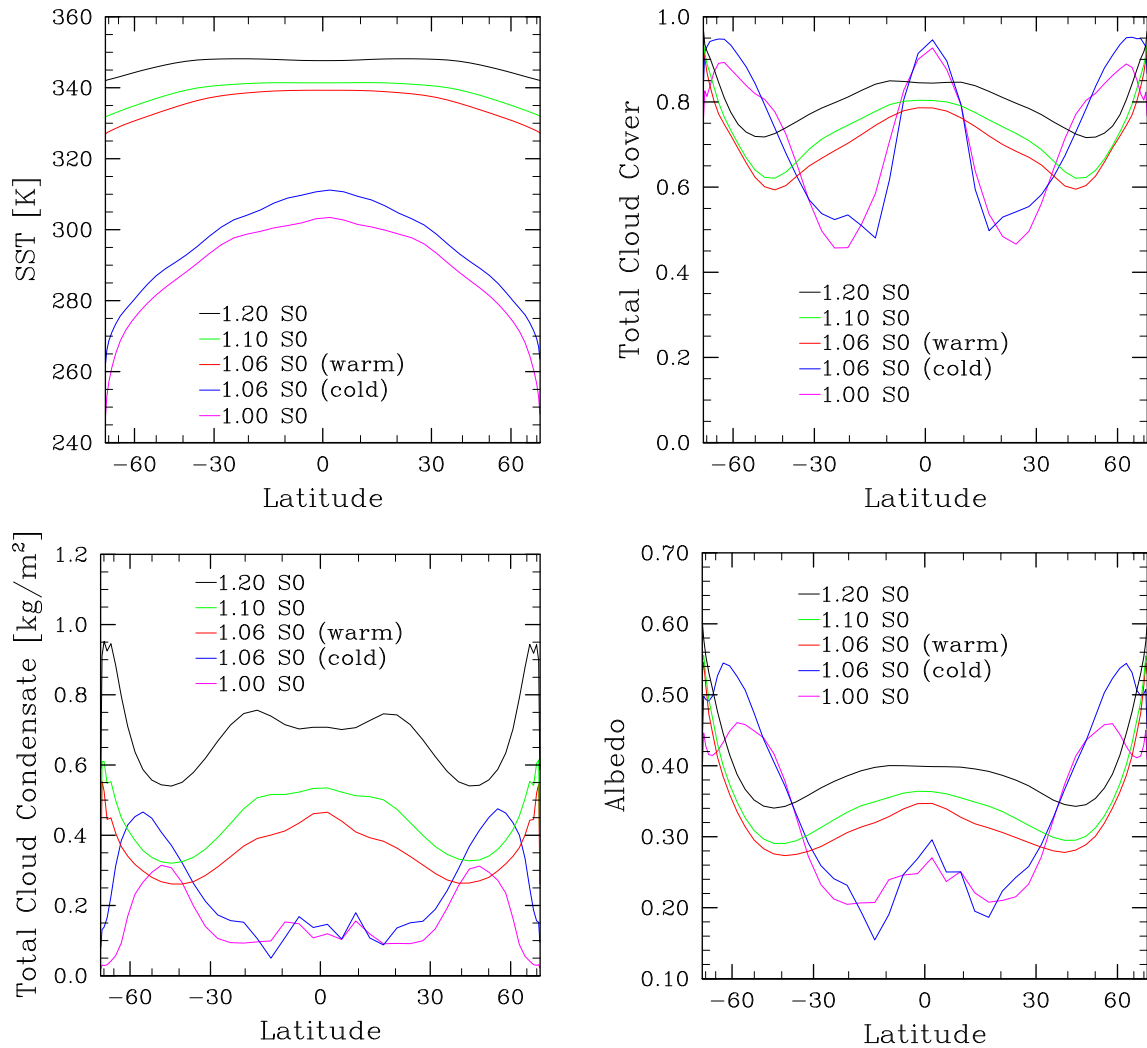


Figure 3.2: Zonal and temporal average over the last 30 years in steady-state of SST (top left panel), total amount of cloud condensate (bottom left panel), total cloud cover (top right panel) and albedo (bottom right panel) for five different simulations plotted against latitude. The horizontal axis is scaled with the sine of the latitude.

the cloud albedo is smaller at mid latitudes (Figure 3.2). This structure is partly a consequence of a widening of the Hadley cells. However, not only do the Hadley cells widen, but the relative humidity (not shown), the amount of cloud condensate, and the cloud cover are considerably larger in the subsidence region of the Hadley cells (Figure 3.2), which is a consequence of the much weaker tropospheric circulation (Figure 3.3). The increase of moisture, cloud condensate and cloud cover in the subsidence region of the Hadley cells also leads to a strong greenhouse effect. In fact, the outgoing longwave radiation in the warm state in this region is smaller than in the cold state (Figure 3.4). However, due to a strong negative cloud feedback, the total effect of the changes within the Hadley cells is a cooling (Figure 3.4). At the poleward flanks of

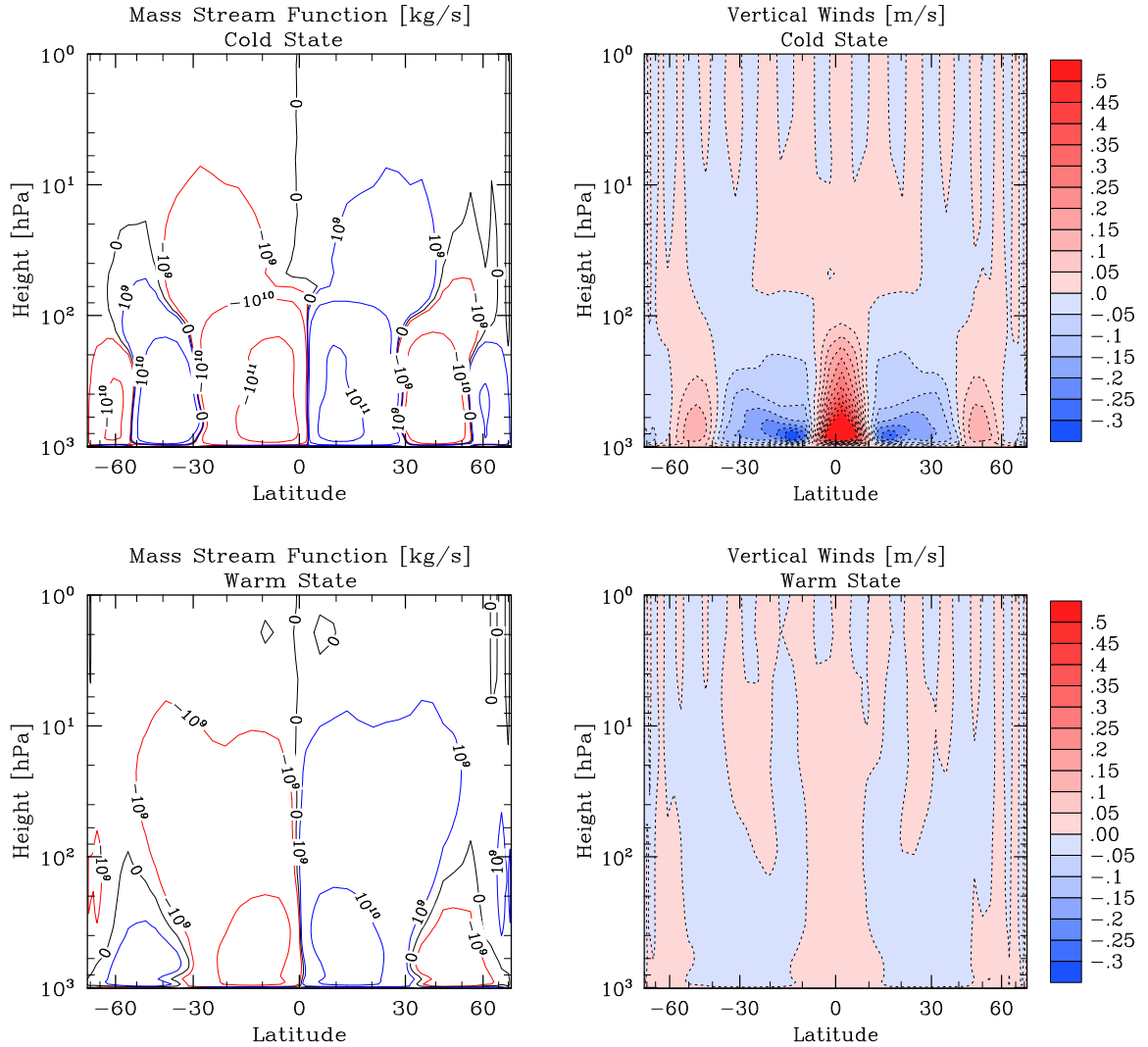


Figure 3.3: Temporal average over the last 30 years of the Eulerian-mean mass-stream function (left panels) and the vertical velocity (right panels) for the simulation with a TSI of 1.06  $S_0$  in the cold steady-state (top panels) and in the warm steady-state (bottom panels). The vertical axes are the height in terms of pressure of dry air and the horizontal axes are the latitude scaled with its sine. Blue contour lines denote clockwise rotation and red contour lines denote counter-clockwise rotation on the left panels.

the Hadley cells and at mid-latitudes the difference of the net radiative flux at the top of the atmosphere between the warm and the cold state is positive (Figure 3.4). This positive effect is caused by the increased greenhouse effect in the warm state at the poleward flanks of the Hadley cells, while at mid-latitudes the decreased cloud albedo is responsible for the positive difference (Figure 3.4). The decreased heating at low latitudes and the increased heating at mid-latitude may be partly responsible for the much lower meridional temperature gradient in the warm state. Furthermore, in the warm regime, the Ferrel cells extend to the poles, and therefore warm air is advected up to the low-level convergence at the poles, and the increased meridional moisture

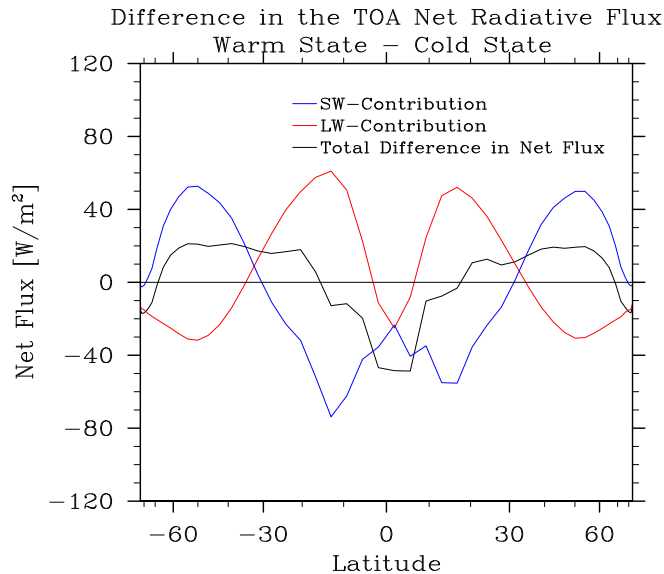


Figure 3.4: Difference of the zonal and temporal average over the last 30 years of the steady-state radiative imbalance at the top of the atmosphere (TOA) between the warm and the cold state for the simulation with a TSI of  $1.06 S_0$  plotted as a function of Latitude. The black line denotes the net difference in imbalance, the red line denotes the difference in the LW-contribution and the blue line denotes the difference in the SW-contribution to the net imbalance. The horizontal axis is scaled as the sine of the latitude.

gradient in the warm state leads to an increased poleward energy transport despite the weaker circulation within the Ferrel cells (not shown).

In the warm regime, the gSST increases gently with TSI at all latitudes (Figure 3.2), as does the cloud cover and the total cloud condensate (Figure 3.2). As a consequence, the albedo increases, which allows the system to stay in equilibrium (Figure 3.2). This increase in cloud cover and total cloud condensate occurs across all latitudes. Since the cloud-top temperatures do hardly change with TSI in the warm regime, the OLR changes little with TSI as well. The clouds form in the middle and upper troposphere starting where the temperatures fall below 300 K and reach up to the tropopause (Figure 3.5). Both cloud cover and amount of cloud condensate have a maximum at the equator and another one at high latitudes. However, the subsidence region of the Hadley cells is considerably moister than in the cold regime, and both cloud cover and amount of cloud condensate are larger in this region in the the warm regime. Due to the weak meridional circulation, convective cells form everywhere on the planet and are an important source of both clouds and precipitation, especially in the (weak) subsidence regions (not shown). The large vertical spread of cloud condensate and the relatively low fractional cloud cover in the warm regime (Figure 3.5), are both a consequence of the frequent occurrence of convective cells (not shown).

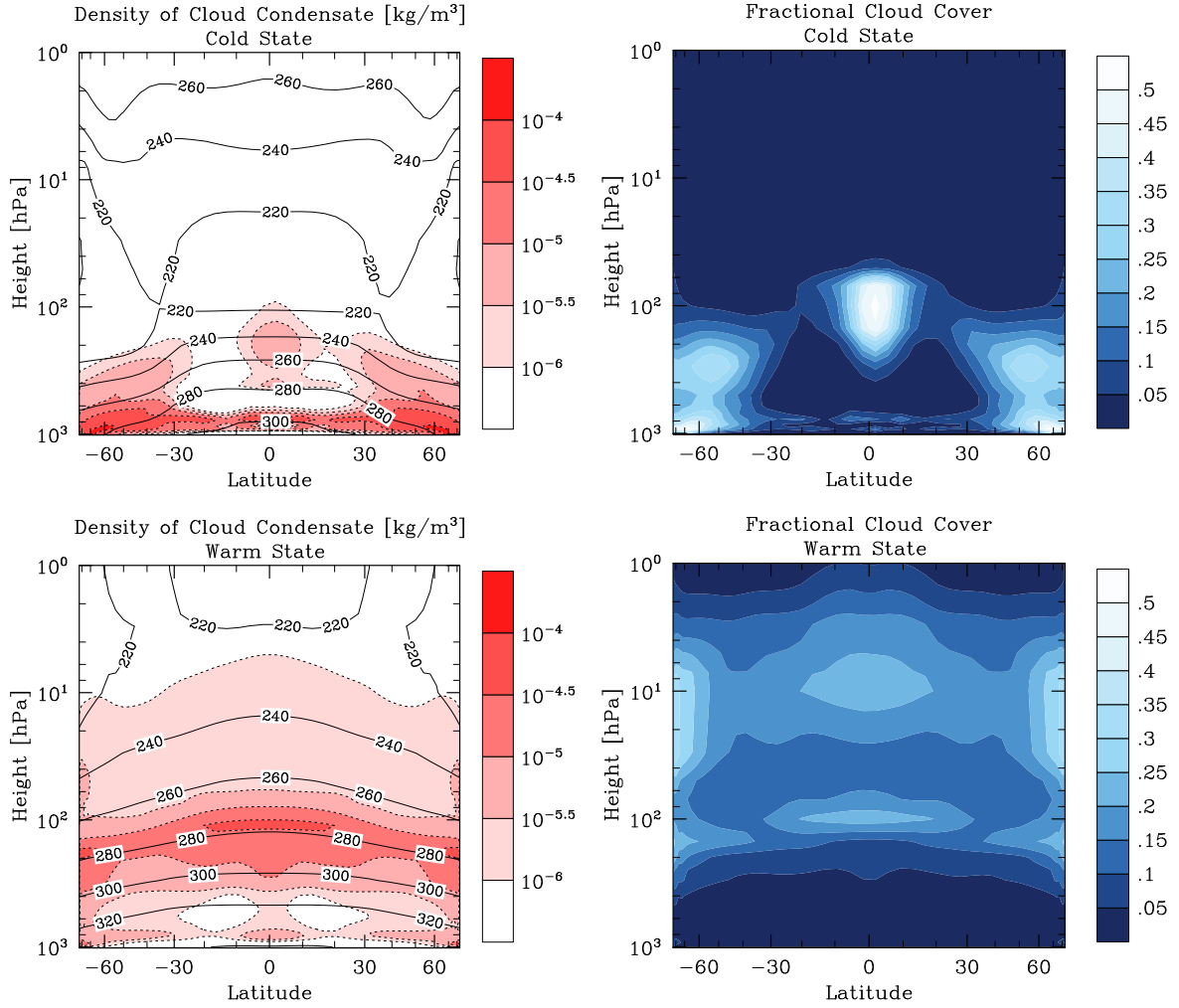


Figure 3.5: Zonal and temporal average over the last 30 years of the cloud condensate (left panels) and the fractional cloud cover (right panels) for the simulation with a TSI of  $1.06 S_0$  in the cold steady-state (top panels) and in the warm steady-state (bottom panels). The contours on the left panels denote temperatures in Kelvin. The vertical axis is the height in terms of pressure of dry air and the horizontal axis is the latitude scaled with its sine.

The tropopause reaches up to 1 hPa at the equator in the warm state, and water vapor becomes an important emitter in all of the stratosphere. Hence, the increase in temperature in the stratosphere, typical of the cold regime, is less pronounced in the warm regime (Figure 3.6). As the TSI is increased to  $1.2 S_0$  the specific humidity in the stratosphere increases even further (Figure 3.6).

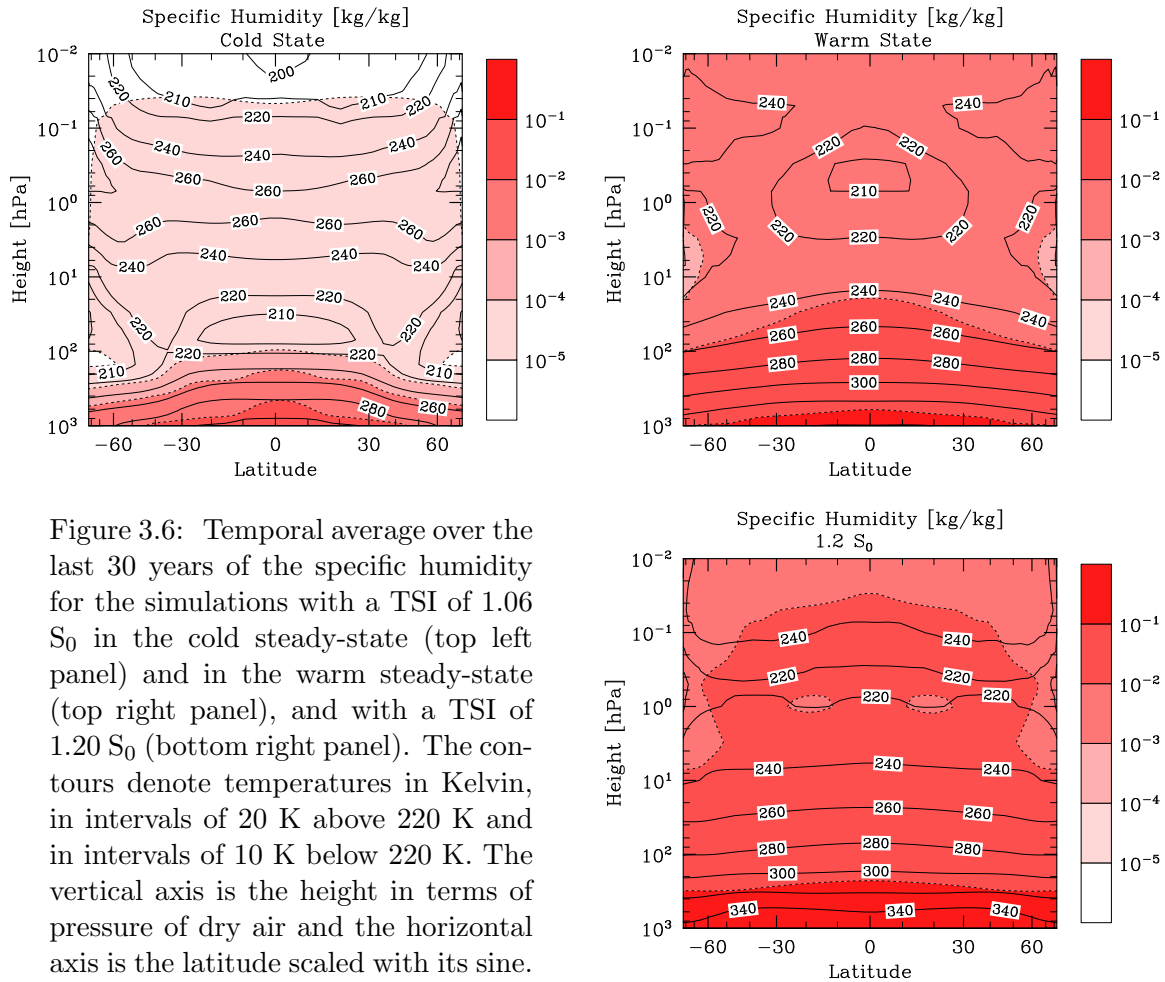


Figure 3.6: Temporal average over the last 30 years of the specific humidity for the simulations with a TSI of 1.06  $S_0$  in the cold steady-state (top left panel) and in the warm steady-state (top right panel), and with a TSI of 1.20  $S_0$  (bottom right panel). The contours denote temperatures in Kelvin, in intervals of 20 K above 220 K and in intervals of 10 K below 220 K. The vertical axis is the height in terms of pressure of dry air and the horizontal axis is the latitude scaled with its sine.

### 3.3.2 Climate instability and transient behavior

Our results suggest that a climate instability exists for a TSI between 1.06 and 1.08  $S_0$  (Figure 3.1). We focus now on the simulation with a TSI of 1.08  $S_0$  to investigate the transient behavior from the cold to the warm state. The progressive increase of the total radiative effect at the top of the atmosphere with increasing gSST in the range between 300 K and 320 K is evidence of this climate instability (Figure 3.7). We define here the total radiative effect to be the total radiative imbalance at the top of the atmosphere minus its mean value over the first year of the simulation. The shortwave and the longwave effects are defined analogously. The shortwave effect increases first at most latitudes except for a narrow region at the equator and except for high latitudes (Figure 3.7). This increase is caused by a decrease of cloud cover (Figure 3.8), especially of the clouds at the top of the boundary layer in the Hadley cells (Figure 3.9). The Planck effect outweighs, however, the positive shortwave cloud

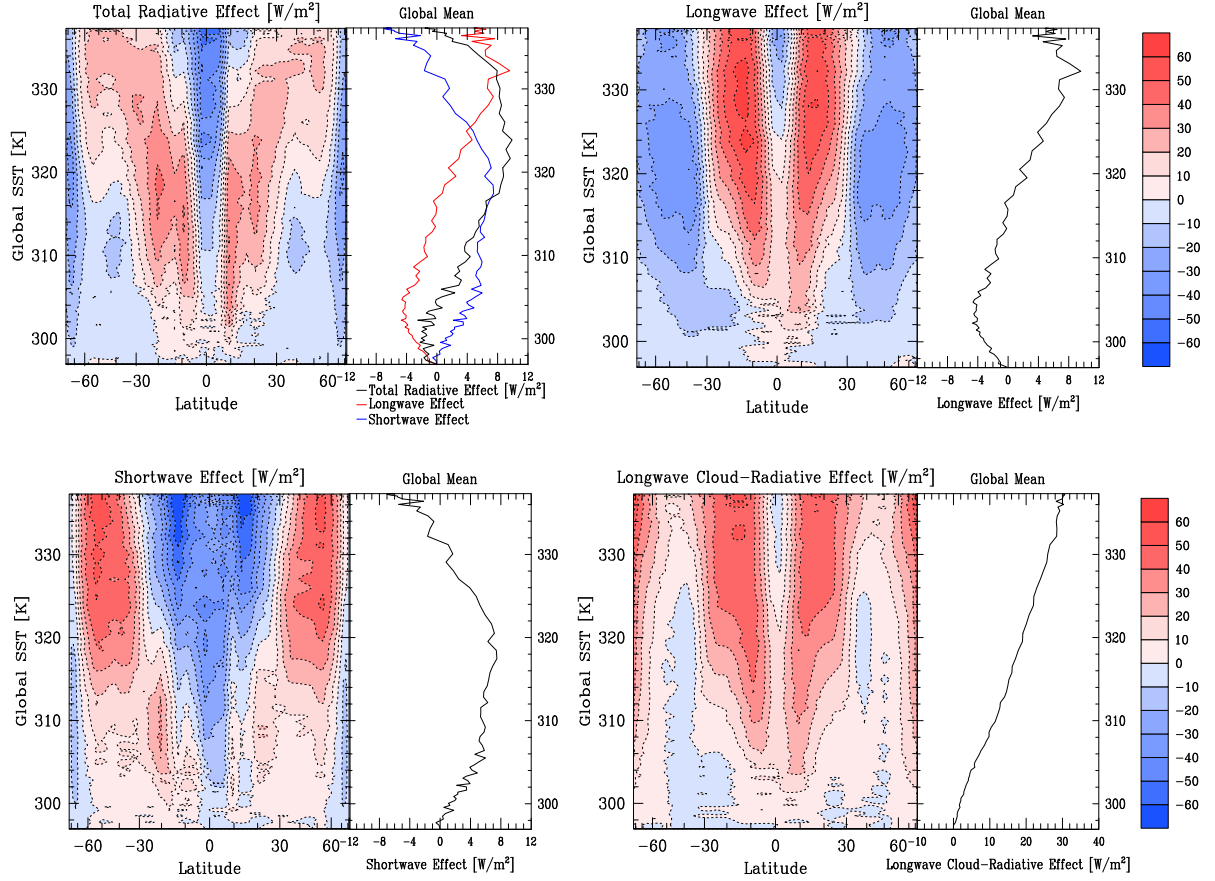


Figure 3.7: Zonal mean of total radiative effect (top left panel), of longwave effect (top right panel), of shortwave effect (bottom left panel) and of longwave cloud-radiative effect (bottom right panel) as a function of the global SST and latitude, for the transient simulation with a TSI of  $1.08 S_0$ . The radiative effects are calculated as changes from the initial radiative imbalances. The latitude is scaled with its sine. The global average of these quantities is plotted as a function of gSST to the right of the zonal averages.

radiative effect and the total radiative effect decreases to a minimum of  $-2 \text{ W m}^{-2}$  at a gSST of 300 K (Figure 3.7). Due to the initial radiative forcing of around  $4.7 \text{ W m}^{-2}$  the negative feedback is, however, not strong enough for the planet to attain an equilibrium. The further evolution of the total radiative effect with increasing gSST is a consequence of the weakening of the meridional circulation with increasing gSST (Figure 3.8). As the Hadley circulation weakens, high clouds form more frequently in the subsidence region of the Hadley cells (Figure 3.9), which leads to a progressive increase of the longwave effect there, as the gSST exceeds 305 K (Figure 3.7). This increase in longwave cloud radiative effect in the subsidence region of the Hadley cells dominates the negative longwave effect at mid and high latitudes caused by the Planck feedback. The weakening of the circulation leads, furthermore, to a decrease of cloud cover in the storm-track region which leads to a further increase of the shortwave

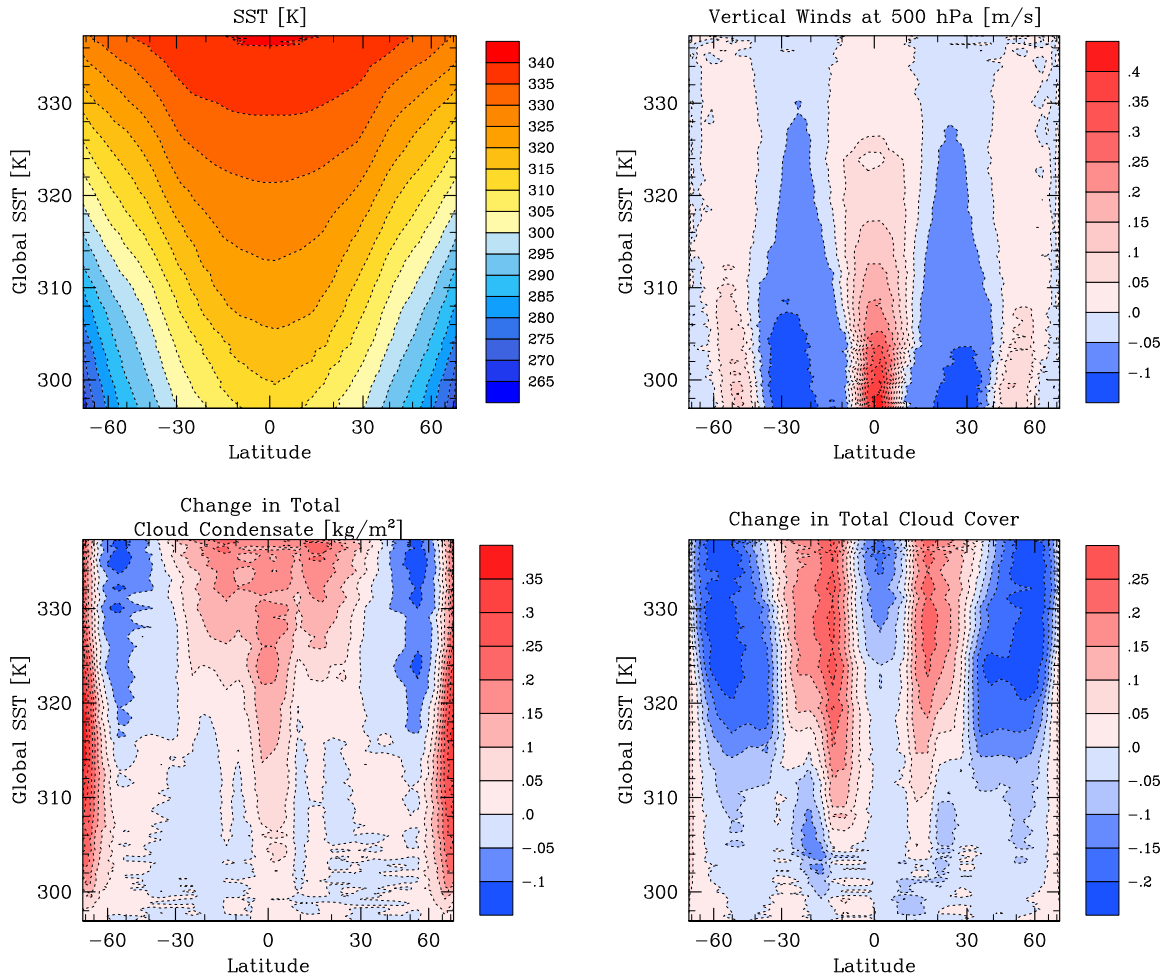


Figure 3.8: Zonal mean of SST (top left panel), of vertical winds at 500 hPa (top right panel), of change in total cloud condensate (bottom left panel) and of change in total cloud cover (bottom right panel) as a function of the global SST and latitude for the transient simulation with a TSI of  $1.08 S_0$ . The latitude is scaled with its sine. The changes in total cloud condensate, total cloud cover and vertical winds are with respect to the annual average of the first year of simulation.

effect (Figure 3.7). As the gSST attains 315 K, the atmospheric structure changes fundamentally (Figure 3.10). Deep convection in the tropical upwelling region starts driving the tropopause upward, injecting more and more water vapor into the upper levels of the model. The infrared cooling by the water vapor in the upper levels makes the atmosphere even more unstable. As the circulation weakens further, convective cells become more frequent in the subsidence region of the Hadley cells and drive the tropopause upward there as well (Figure 3.10). The associated increase in cloud cover and cloud condensate leads to an increase of longwave cloud radiative effect and to a decrease of the shortwave effect (Figure 3.7). As the cloud tops stop climbing within

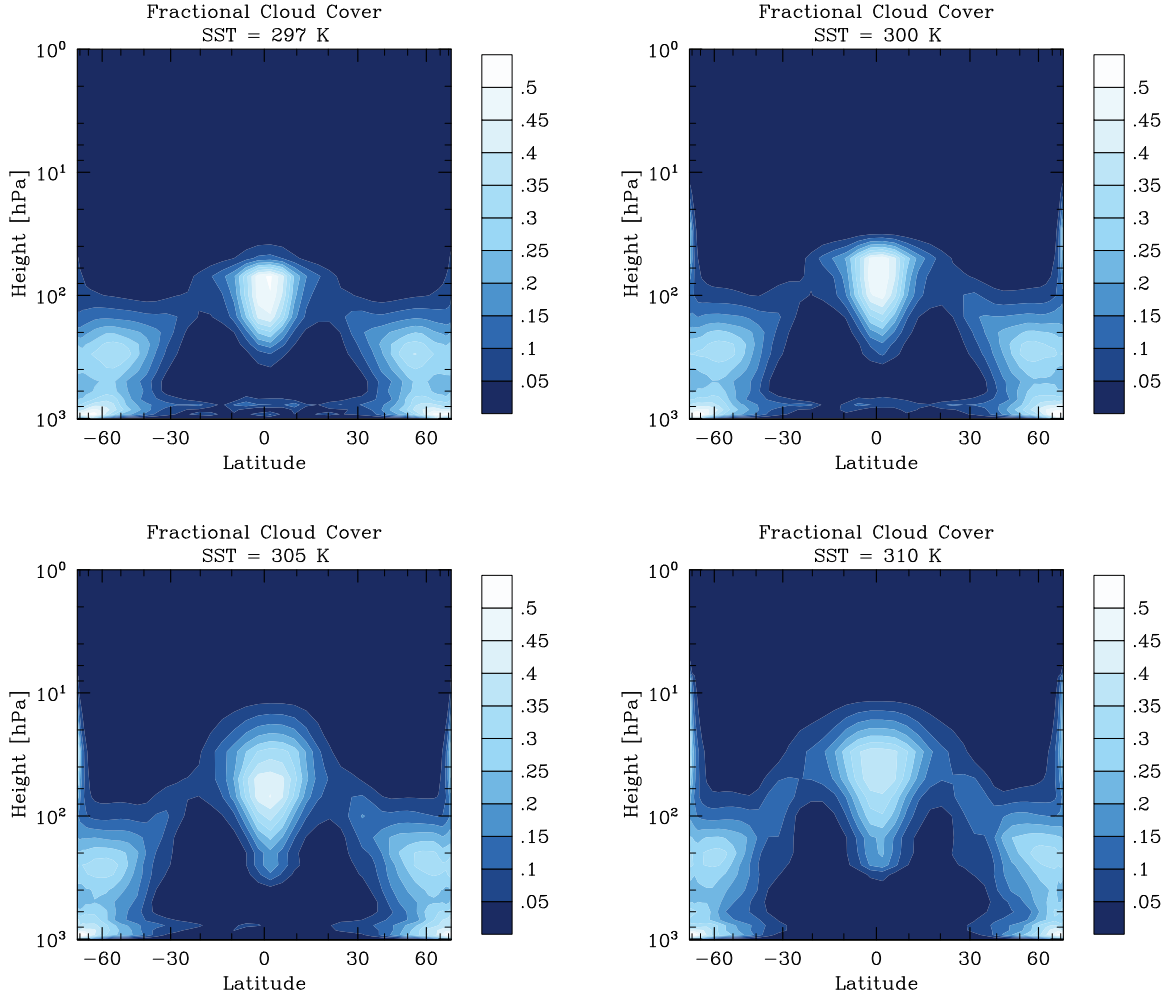


Figure 3.9: Zonal mean of fractional cloud cover for the transient simulation with a TSI of  $1.08 S_0$  at global SSTs of 297 K (top left panel), of 300 K (top right panel), of 305 K (bottom left panel) and of 310 K (bottom right panel). The vertical axis is the height in terms of pressure of dry air and the horizontal axis is the latitude scaled with its sine.

the Hadley cells at a gSST of around 325 K, the longwave cloud radiative effect within the Hadley cells stabilizes. However, since the clouds keep thickening in all of the Hadley cells with increasing SSTs the shortwave effect keeps decreasing (Figure 3.7). Eventually the total radiative effect becomes negative and allows the system to attain a new equilibrium. During the whole transient period an increasing amount of energy is transported to high-latitudes with increasing gSST (not shown), which causes the high latitude SSTs to rise rapidly during the whole period (Figure 3.8). Eventually the meridional temperature gradient in the new equilibrium is only of the order of 10 K. The decrease in meridional temperature gradient with increasing gSST may explain the weakening of the tropospheric circulation.

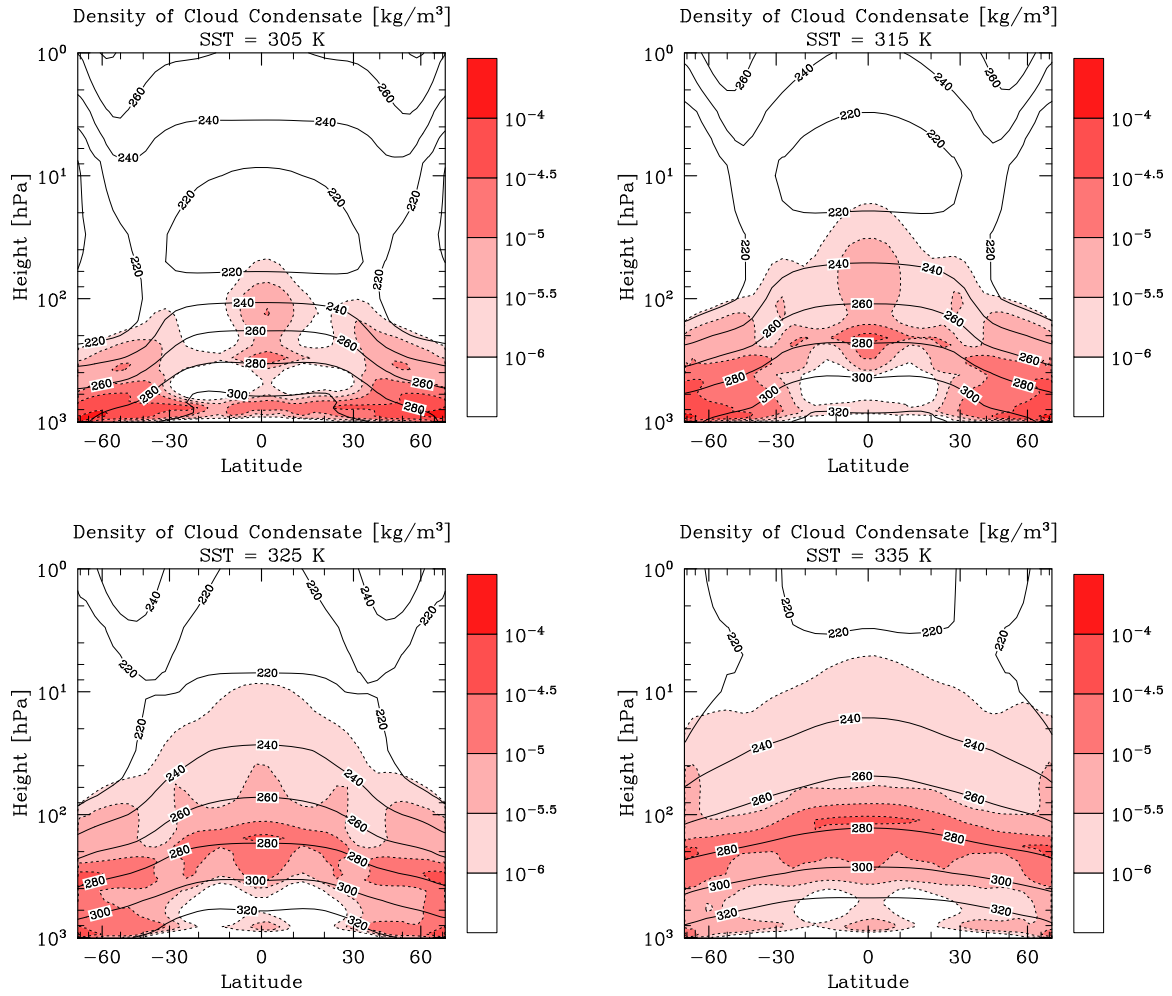


Figure 3.10: Zonal mean of the density of cloud condensate for the transient simulation with a TSI of  $1.08 S_0$  at global SSTs of 305 K (top left panel), of 315 K (top right panel), of 325 K (bottom left panel) and of 335 K (bottom right panel). The contours denote temperatures in Kelvin. The vertical axis is the height in terms of pressure of dry air and the horizontal axis is the latitude scaled with its sine.

## 3.4 Discussion

### 3.4.1 Limitations of the model

We overestimate the gSST in the cold states because of the absence of sea ice in the model. In the steady state with  $1.06 S_0$  there would be sea ice at latitudes higher than  $75^\circ$  that would increase the planetary albedo. Hence, a larger TSI may be required for the climate transition to the warm state to occur, and the range of TSI for two distinct equilibria to exist could thus be underestimated. The absence of sea ice in our model may partly explain the larger TSIs required in the studies by Boer et al. (2005) and Abe et al. (2011). Donohoe and Battisti (2011) demonstrate, however, that, based on observations and model results, the atmospheric reflection dominates the surface reflection, even near the poles. Therefore the influence of the sea-ice albedo on the global energy budget is smaller than intuitively expected. Furthermore, by neglecting sea ice we demonstrate that the existence of two equilibria is not a consequence of sea ice being present in the cold state.

In the methods we already mentioned that energy is not fully conserved in ECHAM6 and that this leads to an imbalance between the top of the atmosphere and the surface energy fluxes in equilibrium. In our setup, for a TSI of  $1.0 S_0$ , the 30 year global mean of the imbalance in equilibrium is  $1.5 \text{ W m}^{-2}$ . It increases to  $2.8 \text{ W m}^{-2}$  for a TSI of  $1.06 S_0$  in the cold state (at 296 K) and to  $5.3 \text{ W m}^{-2}$  in the warm state (336 K), to  $5.5 \text{ W m}^{-2}$  for a TSI of  $1.1 S_0$  (at 339 K), and to  $6.9 \text{ W m}^{-2}$  for a TSI of  $1.2 S_0$  (at 347 K). Small imbalances also occur in the single-column version of the model, but they tend to be negative (Chapter 2). Therefore, there must be energy lost in the three-dimensional system. Since the magnitude of the changes of steady-state imbalances are considerably smaller than the magnitude of the forcings we apply, the impact of these imbalances on the behavior of the model in the transient simulations should be small enough, not to affect any general conclusion we draw from the results. A known problem is that tracers cannot be conserved in a spectral model with vertical sigma-hybrid coordinates and hence water vapor (which is treated as a tracer) is not conserved. However, the diagnosed loss of water can account for  $2 \text{ W m}^{-2}$  of imbalance in the energy fluxes at most, and hence there must be other causes for the loss of energy.

The mass of water vapor is not included in the calculations of pressure in the horizontal transport but would lead to a larger increase in pressure at the equator than at the poles in the warm state, due to the meridional temperature gradient. The contribution of water vapor to the surface pressure difference between equator and poles is of the order of 40 hPa in the warm state. This meridional pressure gradient

would lead to an increase in poleward motion and hence to an additional poleward energy transport. An equilibrium would therefore require the temperature gradient to decrease, and therefore our model overestimates this gradient.

### 3.4.2 Physical interpretation of the results

#### Physics of the climate instability

As seen in the results, the climate instability that occurs as the TSI is increased from  $1.06 S_0$  (in the cold state) to  $1.08 S_0$ , is a consequence of the increase of the total cloud radiative effect. With the single-column version of the model we found also an increase of cloud radiative effect to be responsible for the climate transition from the cold to the warm state, which was caused by the decrease of reflected shortwave radiation due to the disappearance of the clouds at the top of the boundary layer (Chapter 2). Here the increase of the cloud radiative effect is more complex, with contributions from a reduction of cloud cover at the top of the boundary layer, an increase of high clouds in the subsidence region of the Hadley cells, and a decrease of cloud cover in the storm-track regions. The reduction of cloud cover in the storm-track regions is simply a consequence of the decrease of the meridional temperature gradient and the associated decrease of baroclinic eddies. The increase in cloud radiative effect in the tropics within the Hadley cells occurs in two phases. In the first phase, at a gSST of up to around 305 K, the convection cells in the upwelling region deepen (Figure 3.11, top right). Therefore, the dry adiabatic descent in the subsidence region stretches across a larger vertical extent and hence leads to a drying of the free troposphere. Therefore, the gradient of moist static energy (but not necessarily of relative humidity!) across the top of the boundary layer increases, which leads to stronger mixing of dry air into the boundary layer (Brient and Bony, 2013). This drying leads in turn to a decrease of boundary-layer clouds, which leads to a decrease of reflected shortwave radiation. In the second phase (Figure 3.11, bottom left), the weakening of the Hadley circulation favors the occurrence of convective cells in the subsidence region. This leads to an increase of clouds with high tops in this region. This in turn leads to a strong reduction of outgoing longwave radiation, which dominates the increase in reflected shortwave radiation in this phase.

Eventually the total radiative effect starts decreasing again: The increase in cloud condensate of the clouds which are formed as a consequence of convective activity leads to an increase in reflected shortwave radiation, whereas the outgoing longwave radiation remains constant due to constant cloud-top temperatures (Figure 3.11, bottom

### Changes in the Hadley cells

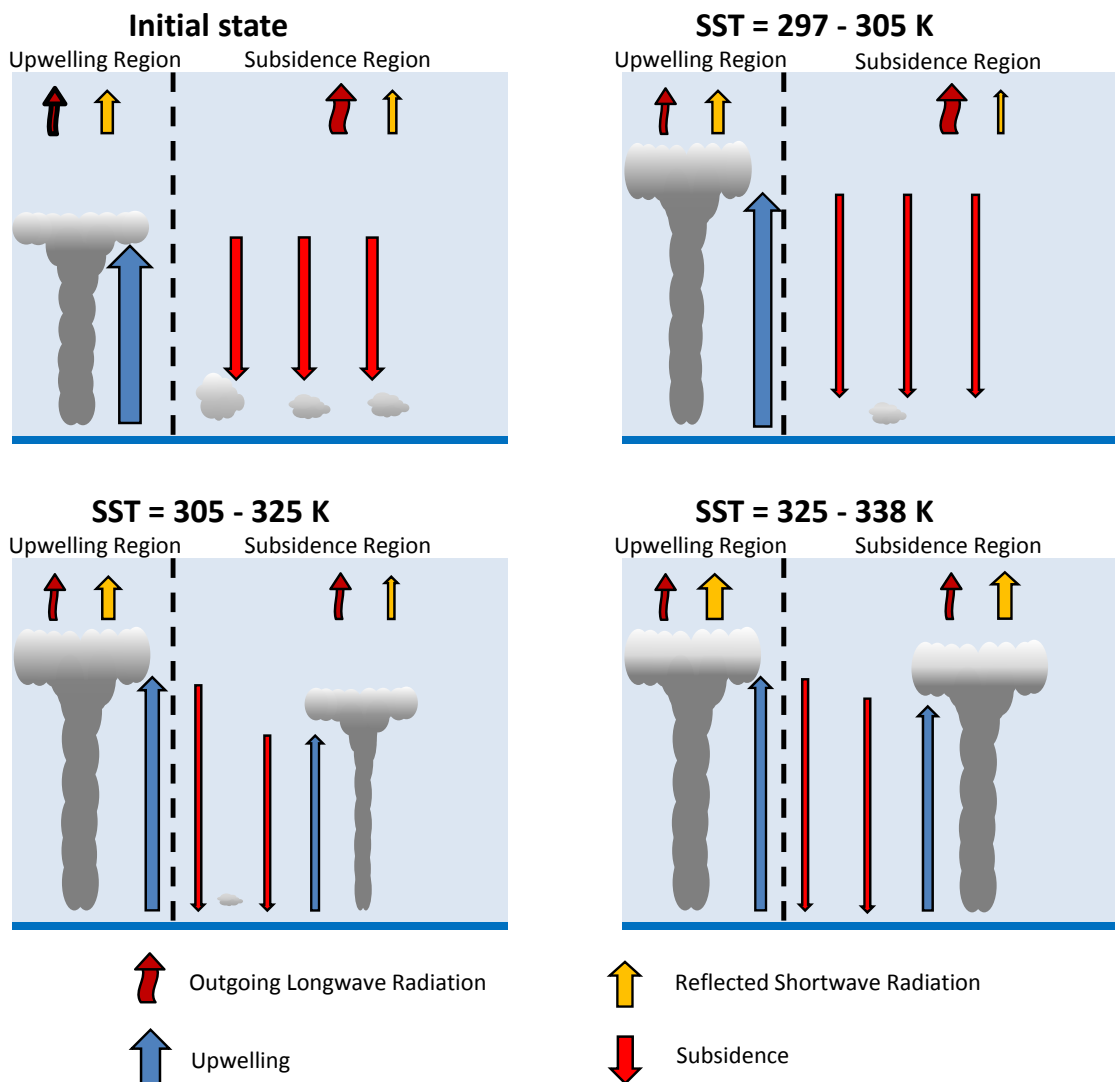


Figure 3.11: Changes in the Hadley cells during the transient period of the simulation with a of  $1.08 S_0$ . The width of the arrows scales with the flux of the associated quantity. The top left panel shows the initial state. In a first phase (top right panel) the subsidence region dries and leads to a decrease of planetary boundary layer and to a decrease of reflected shortwave radiation. In a second phase (bottom left panel) the weakening of the circulation leads to an increase of convective activity in the subsidence region and leads to a reduction of outgoing longwave radiation. During a last phase (bottom right panel) the convective clouds become increasingly thick which leads to an increase in reflected shortwave radiation.

right). The constant cloud-top temperatures are in agreement with the fixed anvil temperature theory by Hartmann and Larson (2002). Finally, it is the increase of reflected shortwave radiation within the Hadley cells which allows the aqua-planet to attain a new equilibrium.

### Clouds in the warm regime

In the warm regime, the zonal means of both total cloud condensate and cloud cover are increasing with increasing gSSTs. The outgoing longwave radiation remains nearly constant with increasing gSST, and an equilibrium is maintained due to the increasing cloud albedo. Hence, the results we obtain with our model are in agreement with the results we obtained with the single-column version of our model (Chapter 2). The mechanism responsible for this result was described in Chapter 2: The cloud top temperature remains constant, because the abundance of water vapor is linked to temperature (Hartmann and Larson, 2002) and because the clouds are already opaque in the infrared, and therefore additional cloud condensate increases the albedo only. This mechanism cannot, however, explain the increase in cloud cover.

Due to the weak meridional circulation in the warm state, most clouds are formed as a consequence of convective cells. Since the upwelling regions of such cells tend to be cloudy even in the present-day climate, the increase of cloud cover must occur over the subsidence regions. The results suggest that this is not a consequence of an increase of clouds at the top of the boundary layer, but that the increase of cloud cover occurs at layers above. We perform a simulation of three months with two-hourly output in steady state for both a TSI of  $1.06 S_0$  in the warm regime and a TSI of  $1.2 S_0$ . The results suggest that the frequency of cloudy periods is similar in both steady states, whereas the average lifetime of clouds in a grid-cell (henceforth local lifetime) above 200 hPa at latitudes between 32 S and 32 N is larger in the simulation with  $1.2 S_0$ . Especially at around 100 hPa, where the density of cloud condensate is high, there is a strong maximum with an average local lifetime of 23 hours in the simulation with a TSI of  $1.2 S_0$  compared to 17 hours in the one with a TSI of  $1.06 S_0$ . Since the increase in average duration of upwelling periods is much smaller than the increase of the local lifetime of the clouds around 100 hPa, the clouds at this level persist much longer into periods of subsidence. The increased cloud cover in the simulation with  $1.2 S_0$  is predominantly a consequence of this effect. Since clouds are advected by the model, the local lifetime of a cloud is not only affected by its total lifetime, but also by its horizontal extent and the local wind field by which it is carried along. Our analysis does not, however, allow us to determine the contribution of these effects to the average local lifetime of clouds. Note, that in order to avoid the influence of large-scale clouds in the storm-track regions, we did not include the mid and high latitudes into this analysis.

The prolonged lifetime of the clouds can be understood by extending the framework by O’Gorman and Schneider (2008). They show that in warm steady states, the

global-mean latent heat flux and hence the global-mean evaporation increase proportionally to the global-mean net solar flux at the surface. By mass conservation the global-mean precipitation increases proportionally to the global-mean net solar flux at the surface as well. In the warm regime of our simulations, the global-mean net solar flux at the surface hardly changes with increasing TSI, and therefore the global-mean precipitation is also nearly constant (not shown). However, the amount of atmospheric water vapor increases with increasing TSI. Since convection tends to lift larger amounts of water vapor with increasing amounts of atmospheric water vapor available but the precipitation remains constant, the amount of cloud condensate at the cloud top increases. This increase of cloud condensate leads either to a prolonged lifetime of the cloud tops or to an increase of their horizontal extent, which both in turn lead to a larger average cloud cover, and, if the wind speeds do not increase (which they do not in our simulations), to a longer average local lifetime.

### 3.5 Comparison to previous work

One of the main differences between the results obtained with our three-dimensional model compared to the ones obtained with the single-column version thereof used in Chapter 2 is that the upper levels become substantially moister in the warm regime in our three-dimensional model. The volume mixing ratio of water vapor exceeds the Moist Greenhouse limit of  $3 \times 10^{-3}$  (Kasting et al., 1993) at the top level at low and mid latitudes in all steady states in the warm regime, and hence the water vapor would be subject to increased photo-dissociation. So unlike in the single-column version of the model, the three-dimensional model is capable of representing the Moist Greenhouse. The reason why the stratosphere is much moister in the three-dimensional version of our model is that, due to the enhanced deep convection in this model, the vertical temperature gradient is much smaller which leads to a much higher tropopause and as a consequence to a much moister stratosphere than in the single-column version. But even though the single-column version fails to represent the Moist Greenhouse in the warm regime, there are nonetheless similarities between the warm regime obtained with both the three-dimensional and the single-column versions of our model. The most important similarity is that clouds provide a strong negative feedback in the warm regime of both versions of the models. Furthermore, the mechanisms leading to this result are similar. Therefore, since we could run the single-column model to considerably higher TSI and since we found that the negative cloud feedback allowed the column to remain in the warm regime up to TSIs of at least  $1.5 S_0$ , we expect that the aqua-planet would remain in the warm regime and thus in the Moist Greenhouse for considerably larger values of TSIs than we applied here. The three-dimensional model also produces only few low clouds in the warm regime (except at the poles), but the low clouds are not as vigorously suppressed as in the single-column model. Another main difference between the two versions of the model is that the climate transition from the cold to the warm regime occurs at much lower TSI in the single-column version (around  $1.4 S_0$  in the single-column version and  $1.06 - 1.08 S_0$  in the three-dimensional one). The climate of the single-column version of the model is kept in the cold state due to an increase in boundary-layer clouds. Since it is difficult to mix dry air into the boundary layer as pointed out in Chapter 2, the amount of cloud condensate is much larger in the single-column version than anywhere at low latitudes in the three-dimensional version of the model. The maximum temperature attained in the cold regime of the single-column version is very similar to the maximum gSST attained in the cold regime of the three-dimensional version of the model (around 296 K). However, the warm regime starts at much lower temperature (around 335 K) in the three-dimensional than in the single-column version of the model.

Boer et al. (2005) found the runaway behavior of the surface temperatures to be predominantly caused by a reduction of cloud cover with increasing global-mean surface temperatures in their three-dimensional model. Thus, their results are in agreement with ours in so far as it is the clouds which cause the climate to become unstable in the cold regime for large enough TSI. However, the longwave cloud radiative effect does not contribute to the instability in their model, since, unlike in our model, there is no increase of high clouds in the subsidence region of the Hadley cells. This is surprising, since Boer et al. (2005) also find a weaker Hadley circulation in their model at higher global-mean surface temperatures and hence less strong subsidence. They find no sign of stabilization of the climate as the global-mean surface temperature increases. Their model fails, however, at global-mean surface temperatures which are too low to assess whether a steady state in the warm regime can be attained, especially since a larger TSI is required to destabilize the cold climate in their study and therefore a possible steady state in the warm regime may only be attained at even higher global-mean surface temperatures than in our study.

Our results suggest that the Hadley circulation is weaker and reaches further polewards in the warm regime than in the cold one. This result is in accordance with the results obtained by Levine and Schneider (2011), who found in an idealized study of an aqua-planet that for global SSTs exceeding 295 to 300 K, the Hadley circulation weakens and widens slowly (if the poleward end of the Hadley cells is defined as the location where the mass stream function becomes zero) with increasing gSST.

Yang et al. (2013) recently investigated the effects of clouds on the habitability of a tidally-locked aqua-planet with different GCMs. They found that convection produces thick clouds of high albedo in the region near the substellar point, which leads to a strong negative cloud-radiative effect. So, even though the dynamics on a (slowly rotating) tidally-locked planet are very different from our "fast" rotating planet, clouds appear to provide a strong negative effect as the insolation increases on both planets. Furthermore, the clouds cause this negative effect no matter whether the increase in incoming solar radiation is caused by augmenting the TSI, or whether it is caused by changing the geographical latitude (towards high insolation).

## 3.6 Implications for planetary science

The model results suggest that the critical TSI to destabilize a present-day Earth-like climate lies between  $1.06 S_0$  and  $1.08 S_0$ . However, due to the missing sea ice, the critical value of TSI should likely be larger, since there should still be sea ice near the poles at a TSI of  $1.06 S_0$ . Hence, our estimate of the critical TSI might be biased low. This value is nonetheless larger than the one obtained in the one-dimensional study with a state of the art radiative transfer model by Kopparapu et al. (2013). Hence, our results suggest that an aqua-planet with low obliquity could sustain a present-day Earth-like climate at a shorter distance from its sun than reported by Kopparapu et al. (2013) (0.99 AU), that is, 0.96 to 0.97 AU for our study. Applied to Earth, our results suggest that the climate will remain in a present-day-like regime for at least another 650 to 880 million years (assuming a 9 % increase of TSI per billion years) all else remaining unchanged. However, the double equilibrium at  $1.06 S_0$  indicates that a climate transition could occur earlier than in 650 million years, if large amounts of greenhouse gases were injected into the atmosphere.

Once a TSI of between  $1.06 S_0$  and  $1.08 S_0$  is attained, the planet encounters a climate instability. However, the planet does not go into a Runaway Greenhouse, but the climate attains a warm steady state with low meridional temperature gradient, a weak meridional circulation without polar cells and a cloud regime dominated by convective clouds. The planet remains in this state at least to a TSI of up to  $1.20 S_0$  and hence at least for another billion years assuming again a 9 % increase of TSI per billion years. Since we expect that clouds would keep thickening with increasing gSSTs, we expect the increasing cloud albedo to keep the planet in the warm state for even larger values of TSI. Hence, surface habitability of a low-obliquity aqua-planet could be temporarily ensured to a TSI of up to at least  $1.20 S_0$  or down to a distance of 0.91 AU from the sun.

The volume mixing ratio at the top level of our planet exceeds the Moist Greenhouse limit in the warm regime and may even attain values as large as 0.015 at the top level for a TSI of  $1.20 S_0$ . Unlike most previous studies that exhibited a Moist Greenhouse (e.g. Kasting et al. (1984), Kasting (1988), Kasting et al. (1993), Kopparapu et al. (2013)), we find that the Moist Greenhouse does not evolve from a present-day climate along a trajectory of steady states, but as a result of a climate transition. Since the warm states can be maintained over a large range of TSI, considerable amounts of water vapor could be lost due to photo-dissociation of water vapor and the subsequent escape of hydrogen.

Abe et al. (2011) investigated whether an aqua-planet could evolve into a land planet using the one-dimensional radiative-convective model by Kasting (1988). When they kept the albedo at a present-day Earth value, they found that an aqua-planet would not remain in the Moist Greenhouse regime long enough to lose enough water to transform into a land planet. Instead, the planet would eventually go into a Runaway Greenhouse as the TSI attains a critical value. However, Abe et al. (2011) also pointed out that if the albedo increases, the critical TSI for a Runaway Greenhouse will increase as well. In this case, an aqua-planet may remain long enough in the Moist Greenhouse regime to evolve into a land planet. Our results suggest that clouds are acting to this end and that therefore the Runaway Greenhouse is a rather unlikely scenario for an aqua-planet at Earth's orbit. Furthermore, the global average of SST increases slowly enough with TSI for the aqua-planet to remain at moderately warm temperatures within the Moist Greenhouse regime. However, if most water was lost during the Moist Greenhouse and surface water was becoming scarce at the surface, there would be the possibility that cloud cover decreases and with it the albedo, and that therefore the temperatures would rise rapidly. In this case, the aqua-planet could be sterilized before it could evolve into a land planet.

## 3.7 Conclusions

Based on our simulations of a  $0^\circ$  obliquity aqua-planet with the general circulation model ECHAM6, we conclude:

1. An aqua-planet with a present-day Earth-like climate around a sun-like star will transit to a warm state with global-mean sea-surface temperatures exceeding 335 K, as a total solar irradiance between  $1.06 S_0$  to  $1.08 S_0$  is attained.
2. The transition to such a warm state does not follow a trajectory of steady states, but is caused by a climate instability.
3. The climate instability is caused by a positive cloud feedback. However, the cloud feedback becomes negative again as the surface temperature exceeds 330 K, which allows, together with the increased outgoing longwave radiation at high latitudes, to attain a new steady state.
4. The warm states are in the Moist Greenhouse regime, and hence a planet in such a state is expected to lose water due to photo-dissociation of water and the subsequent escape of hydrogen to space.
5. The dynamics of a planet in a warm state are fundamentally different from a planet in a present-day Earth state, with a low meridional temperature gradient, a weak meridional circulation, and without polar cells.
6. The increasing cloud albedo with increasing TSI can keep an aqua-planet in a warm state up to a TSI of at least  $1.2 S_0$ . Applied to Earth, our result suggest thus that Earth will remain long enough in a warm state to lose considerable amounts, if not nearly all, of its water.

### 3.A Influence of the sponge on the control climate

We discuss first the influence of the sponge on the control climate with  $S_0$ , by comparing the 30 years zonal means of simulations with and without sponge. The difference in the atmospheric temperatures do not exceed 0.8 K at the surface but may attain up to 11 K in the middle atmosphere. At most levels, the largest differences occur at high latitudes whereas the differences are small close to the equator. The difference in zonal winds is small near the surface, but starts increasing above 100hPa and attains large values of up to 60 m/s at the equator at 50 hPa. So despite the considerable impact of the sponge on the middle atmosphere, the influence of the sponge on the surface climate is small. Since the tropopause rises substantially in the warm climate, the sponge may have a larger effect in the warm states, but the impact should still remain small against the impact of the large forcings we apply and should thus not substantially alter the results. In simulations with sponge there is an unusual wave-like pattern at the levels where the sponge is active, which is most certainly a model error, and is partly responsible for the differences in the upper model levels. The error causing this pattern is, however, unknown.

## Chapter 4

# The Runaway Greenhouse as a result of a limitation of outgoing longwave radiation

We use a one-dimensional gray-atmosphere model to assess which properties of temperature profiles cause a limitation of OLR and may therefore cause a Runaway Greenhouse. In contrast to previous studies, no specific assumptions on the temperature profile are made. We find that a limitation of OLR occurs, if the temperature in the optically thin region of the atmosphere remains finite, and if in the optically thick region of the atmosphere the temperature does not increase faster with optical depth than a nearly-exponentially increasing limit profile. The analysis of our conditions reveals that for tropospheric conditions, the occurrence of a limitation of OLR depends crucially on the assumption that the temperature profile is exclusively determined by adiabatic convection. Therefore, temperature profiles should always be calculated dynamically in studies in which a possible limitation of OLR is of importance. Furthermore, if we apply our conditions to an atmosphere in radiative equilibrium, we find a new maximum value of OLR which is lower than the one previously reported.

## 4.1 Introduction

The occurrence of a Runaway Greenhouse (RG) depends crucially on the the existence of a limitation of outgoing longwave radiation (OLR). If the incoming radiation absorbed by the atmosphere and surface exceeds an upper bound of OLR, an uncompensated energy influx occurs. This prevents stabilization of the atmosphere, and hence an equilibrium cannot be reached. Current theories on the limitations of OLR made specific assumptions on the atmospheric temperature profile. Here we present an analysis that allows us to consider the limitation of OLR without specific assumptions on the atmospheric temperature profile.

In the past, two different mechanisms leading to a limitation of OLR have been identified. Simpson already discovered in 1927 that in his simple atmospheric model with prescribed temperature profiles and gray-gas absorption, the OLR does not exceed an upper limit if the temperature is increased (Simpson, 1927). However, Simpson thought this to be a consequence of the gray atmosphere model and did not think of this as a physically meaningful effect (Simpson (1927), Simpson (1928)). Much later, more studies have found limitations of OLR in their models, which can be attributed to the same kind of effect as seen in Simpson’s model, even though different models were used (e.g., Pollack (1971), Abe and Matsui (1988), Kasting (1988)).

Komabayashi (1967) and Ingersoll (1969) found independently of each other a different effect leading to a limitation of OLR. They assumed that the region near the top of the atmosphere (TOA) was in local radiative equilibrium and was underlain by a region saturated with water vapor. In this case, they found that pressure and temperature cannot both be continuous at the transition between the regions if the OLR exceeds a certain upper bound. They concluded from this result that the OLR cannot exceed this upper bound.

Nakajima et al. (1992) were the first to clearly distinguish between the two different limits of OLR. They called the one discovered by Simpson the “tropospheric limit“ and the one discovered by Komabayashi and Ingersoll “Komabayashi-Ingersoll-limit“. They gave a clear explanation of the origin of the Komabayashi-Ingersoll-limit and described the origin of the tropospheric limit in their model. They pointed out that the tropospheric limit of OLR is caused by the convergence of the temperature profile against a limit profile in the region where the most important contribution to the OLR originates. They did, however, not provide an explanation of why the temperature profile converges against a limit profile with increasing surface temperature.

Based on the assumption that a limitation of OLR occurs if the derivative of the

---

OLR with respect to the surface temperature tends to zero, Sugiyama et al. (2005) investigated sufficient conditions for the occurrence of a tropospheric limit. Their ansatz merits a further and deeper analysis and will be discussed in this study.

In the present study, we explain the "tropospheric limit" of OLR with no specific assumptions about the atmospheric temperature profiles. We show that the tropospheric limit is a special case of a more general principle, which also applies to non-tropospheric temperature profiles, such as the one defined by local radiative equilibrium. We propose sufficient conditions for the occurrence of a limitation of OLR and give a detailed physical interpretation of the conditions. We then compare our conditions to the ones proposed by Sugiyama et al. (2005).

## 4.2 Methods

### 4.2.1 Model atmosphere

Since we would like to determine the physical mechanisms leading to a limitation of OLR, it is sufficient to use an idealized model, which makes it easier to determine the influence of individual processes on the OLR. The model is a one-dimensional gray-atmosphere equilibrium model. The model is inspired by the model used by Nakajima et al. (1992), except that we do not assume any particular temperature profile. The assumption of the atmosphere being gray in the infrared may appear to be inaccurate, but we think that the assumption is suitable for our needs, since we are not interested in determining exact values for the maximum OLR. We neglect atmospheric windows for most of our considerations, but we will address this point in the discussion.

We do not assume any particular temperature profile, but assume the atmosphere to be heated at the surface and that hence the surface is the warmest point in the atmosphere. The radiative transfer of incoming shortwave radiation is not treated explicitly. However, the effect of absorption of incoming shortwave radiation can be included into any temperature profile.

At the bottom of the atmosphere there is a reservoir of a volatile greenhouse gas, which can provide an infinite amount of this gas to the atmosphere. A limited amount of other gases may be present, but since they would eventually make up only a negligible fraction as the temperature becomes large, we will assume no other gases to be present in the atmosphere for most calculations. Since the greenhouse gas is present everywhere in the atmosphere, the longwave optical depth  $\tau$ , integrated from the TOA, is a strictly monotonically increasing function with the distance from the TOA and can therefore be used as a vertical coordinate. Henceforth, we will refer to the longwave optical depth simply as optical depth. We do not consider the critical point of the greenhouse gas, which means that there is greenhouse gas in liquid form at the surface for any finite temperature. Therefore, the optical depth of the whole atmosphere  $\tau_s$  is a function of  $T_s$  which tends to infinity as  $T_s$  tends to infinity, and we can write:

$$\lim_{T_s \rightarrow \infty} \tau_s(T_s) = \infty \quad . \quad (4.1)$$

In our model it follows that

$$\lim_{\tau_s \rightarrow \infty} T_s(\tau_s) = \infty \quad . \quad (4.2)$$

We define the temperature profile to be a function  $T: \tau \mapsto T(\tau, T_s)$  with  $T_s$  as a parameter. We denote the temperature in the atmosphere at the location  $\tau \in [0, \tau_s]$  of

a temperature profile  $\tau \mapsto T(\tau, T_s)$  as  $T(\tau, T_s)$ . The temperature of the surface ( $T_s$ ) is in general not equal to the temperature of the atmosphere at the surface:  $T(\tau_s, T_s) \neq T_s$  (e.g., Pierrehumbert (2010)).

### 4.2.2 Radiative transfer

The model to describe the radiative transfer for the longwave radiation is the same as that used by Nakajima et al. (1992). We assume that there is no wavelength-dependence of the longwave absorption. Furthermore we neglect the influence of scattering. The surface emits radiation according to the Stefan-Boltzmann law,  $I^+(\tau_s) = \sigma T_s^4$ , where  $\sigma$  is the Stefan-Boltzmann constant. Furthermore we assume that the atmosphere is in local thermal equilibrium. We further use the two-stream-approximation, that is, we parametrize the radiative fluxes into an upward and a downward radiative stream. We assume hemispheric isotropy to integrate the resulting radiative transfer equations. This yields for the upward longwave radiation flux  $I^+$  and the downward longwave radiation flux  $I^-$  the equations

$$\begin{aligned} I^+(\tau) &= I^+(\tau_s) e^{-\frac{1}{\mu}(\tau_s - \tau)} + \int_{\tau}^{\tau_s} \sigma T^4(\tilde{\tau}, T_s) e^{-\frac{1}{\mu}(\tilde{\tau} - \tau)} \frac{1}{\mu} d\tilde{\tau} \\ I^-(\tau) &= \int_0^{\tau} \sigma T^4(\tilde{\tau}, T_s) e^{-\frac{1}{\mu}(\tau - \tilde{\tau})} \frac{1}{\mu} d\tilde{\tau} \quad . \end{aligned} \quad (4.3)$$

The factor  $\mu$  accounts for the fact that the radiation is not just traveling upward and downward, but is traveling in all directions. Therefore, the attenuation of the intensity of the radiation is larger than the one obtained from the difference in optical depth between two points in the atmosphere and hence requires a rescaling. A derivation of the two Eqs. (4.3), although with a slightly different notation, can be found in detail in Pierrehumbert (2010).

The OLR  $\mathcal{O}_T$  of a given temperature profile  $\tau \mapsto T(\tau, T_s)$  corresponds to the upward flux in the Eqs. (4.3) evaluated at the TOA  $\tau = 0$ :

$$\begin{aligned} \mathcal{O}_T(\tau_s, T_s) &= I^+(0) \\ &= \sigma T_s^4 e^{-\frac{\tau_s}{\mu}} + \int_0^{\tau_s} \sigma T^4(\tilde{\tau}, T_s) e^{-\frac{\tilde{\tau}}{\mu}} \frac{1}{\mu} d\tilde{\tau} \quad . \end{aligned} \quad (4.4)$$

If the OLR given by Eq. (4.4) is bounded for all  $T_s$ , we speak of the ‘‘Nakajima limitation’’ of OLR. Note that in the special case that the temperature profile is given by an adiabatic or a pseudo-adiabatic lapse rate, the Nakajima limitation of OLR corresponds to the tropospheric limit found by Nakajima et al. (1992).

## 4.3 Results

In this section we investigate in which cases the OLR has a Nakajima limitation. We would like to state sufficient conditions for the occurrence of such a limitation that are not too restrictive. Our approach is similar to the one by Sugiyama et al. (2005) in that we also state conditions for the OLR as the surface temperature tends to large values. We do not, however, derive the conditions here, but we prove in the appendix of this chapter that the conditions we propose are indeed sufficient. We explain in the discussion the reasons why such conditions are sufficient and make plausible why conditions of the sort are also necessary.

### 4.3.1 Assumptions

To prove that the conditions we introduce in the next subsection are sufficient for a Nakajima limitation we make three assumptions. These assumptions do not put constraints on the physically relevant cases. The first assumption, which we already discussed in the methods, is that  $\tau_s$  tends to infinity as  $T_s$  tends to infinity (Eq. (4.1)). Second we assume that the temperature at any location  $\tau$  in the atmosphere is finite as long as  $T_s$  does not tend to infinity, and hence

$$T(\tau, T_s) \in \mathbb{R}_{\geq 0}, \quad \forall \tau, T_s \in \mathbb{R}_{\geq 0} \quad . \quad (4.5)$$

Last we want to make an assumption on the relation between  $T_s$  and the temperature of the atmosphere at the surface  $T(\tau_s, T_s)$ , to avoid that the discontinuity of the temperature at the surface grows unrealistically fast. We assume that

$$\exists \beta \in \mathbb{R}_{\geq 0}, \text{ such that } T_s \leq \beta \cdot T(\tau_s, T_s), \quad \forall T_s, \tau_s \in \mathbb{R}_{\geq 0} \quad . \quad (4.6)$$

This assumption is more restrictive than would mathematically be necessary. But since we consider only steady states, large differences between  $T_s$  and  $T(\tau_s, T_s)$  could not be maintained in physically relevant cases, since a large temperature difference would inevitably lead to strong heat diffusion and hence to a reduction of the temperature difference.

### 4.3.2 Conditions

In our plane-parallel gray atmosphere model we make the three assumptions (4.1), (4.5) and (4.6). A Nakajima limitation occurs if a temperature profile  $T(\tau, T_s)$  then

satisfies the following two conditions:

There is a finite surface temperature  $T_{s_0}$ , a finite location  $\tau_0$  in the atmosphere, and a finite temperature  $T_a$ , such that the temperature  $T(\tau, T_s)$  is less than or equal to  $T_a$  at any location  $\tau$  “at or above“  $\tau_0$  ( $\tau \leq \tau_0$ ), if  $T_s$  exceeds  $T_{s_0}$ . In symbols this is:

$$\exists T_{s_0}, \tau_0, T_a \in \mathbb{R}_{\geq 0}, \text{ such that } T(\tau, T_s) \leq T_a, \forall T_s \geq T_{s_0}, \forall \tau \leq \tau_0. \quad (4.7)$$

There is a location  $\tau_1$  at the same location as or above  $\tau_0$  (from the previous condition) and there is a positive  $\epsilon$  such that  $T(\tau, T_s)$  is less or equal to the limit profile  $\hat{T}(\tau) \equiv T_c \cdot e^{\frac{1}{4\mu}\tau} \cdot \tau^{-\frac{1+\epsilon}{4}}$  at any location  $\tau$  “below“  $\tau_1$  ( $\tau > \tau_1$ ), where  $T_c$  is a finite constant. In symbols this is:

$$\begin{aligned} \exists \tau_1 \leq \tau_0 \text{ and } \exists \epsilon > 0, \text{ such that } T(\tau, T_s) \leq \hat{T}(\tau) \equiv T_c \cdot e^{\frac{1}{4\mu}\tau} \cdot \tau^{-\frac{1+\epsilon}{4}}, \\ T_c \in \mathbb{R}_{\geq 0}, \forall \tau > \tau_1, \forall T_s. \end{aligned} \quad (4.8)$$

The proof that the conditions (4.7) and (4.8) are sufficient for a Nakajima limitation to occur can be found in the appendix of this chapter.

## 4.4 Discussion

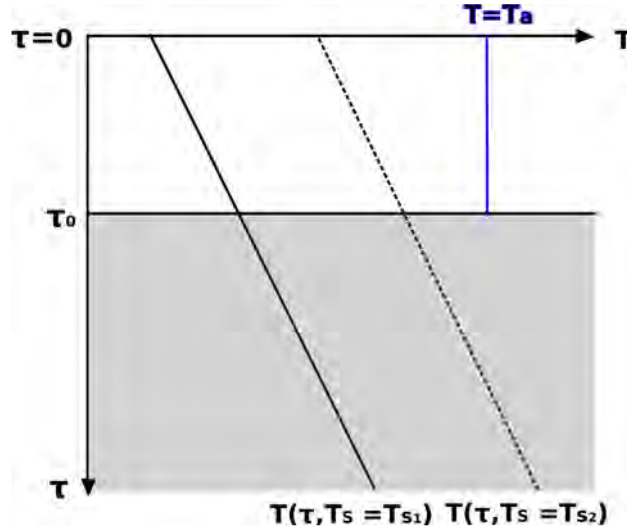


Figure 4.1: Sketch of two temperature profiles with surface temperatures  $T_{s_1}$  and  $T_{s_2}$  in temperature-optical-depth space in the region of the TOA. The shaded part corresponds to the optically thick part of the atmosphere below  $\tau_0$ . The finite temperature  $T = T_a$  is defined according to the condition (4.7).

### 4.4.1 Interpretation of the conditions

We start by discussing what kind of temperature profile it would take for the OLR not to be bounded. Then, we make plausible why the two conditions (4.7) and (4.8) are not only sufficient for a Nakajima limitation to occur, but why two conditions of the sort are also necessary for a Nakajima limitation. Figure 4.1 shows two hypothetical temperature profiles  $\tau \mapsto T(\tau, T_s)$  with different values of  $T_s$ . We assume that the temperature profile with  $T_s = T_{s_2}$  (profile 2) results by starting with the temperature profile with  $T_s = T_{s_1}$  (profile 1) and increasing the surface temperature to  $T_{s_2}$ . We assume the region of the atmosphere above  $\tau_0$  (from condition (4.7)) to be sufficiently thick for the radiation below  $\tau_0$  not to reach space, and hence all of the radiation contributing to the OLR is emitted from the atmosphere above  $\tau_0$ . Since the temperature in this region is larger at any optical depth  $\tau$  for profile 2 than for profile 1, the OLR resulting from profile 2 will also be larger. Hence, if the temperature in the region above  $\tau_0$  keeps increasing with surface temperature, the OLR will also keep increasing. Moreover, if we assume that the temperature in the region above  $\tau_0$  tends to infinity if the surface temperature tends to infinity, then the OLR also tends to infinity and is hence not bounded. So, in order for a limitation of OLR to occur, the condition is necessary

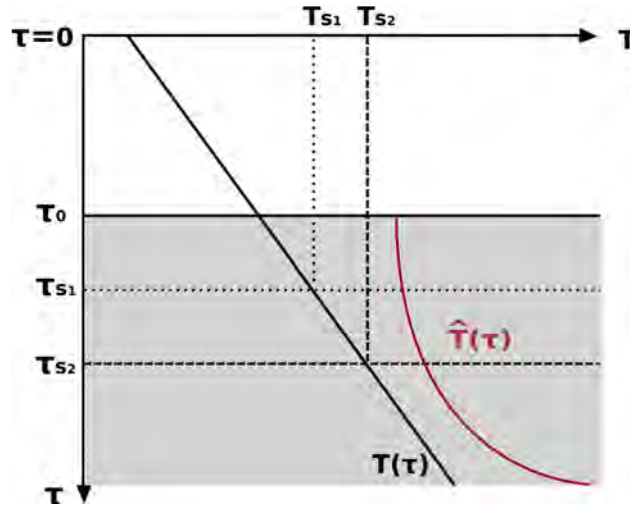


Figure 4.2: Sketch of two temperature profiles with surface temperatures  $T_{s_1}$  and  $T_{s_2}$  in temperature-optical-depth space in the region of the TOA. The shaded part corresponds to the optically thick part of the atmosphere below  $\tau_0$ .  $\hat{T}(\tau)$  denotes the limit profile defined in condition (4.8).

that the temperature above  $\tau_0$  must remain finite as the surface temperature tends to infinity. This is ensured by the condition (4.7), which states that there is an upper bound  $T_a$  for the temperature in the region where the atmosphere emits radiation to space. Mathematically, the condition (4.7) (together with condition (4.8)) is sufficient for the occurrence of a Nakajima limitation, but it is not necessary, because the OLR is bounded even if at single locations the temperature tends to infinity, as long as the integral over the temperature profile remains finite. An example would be the case for which in a region around a location  $\tau_i$  the temperature profile was proportional to  $-\tau - \tau_i$ , since the integral of this temperature profile over the optical depth remains finite in this region. This case is not, however, relevant in physical settings.

We now drop the assumption that the region below  $\tau_0$  does not contribute to the OLR. In this case, even if the condition (4.7) is satisfied, the OLR may still tend to infinity. We consider a temperature profile  $\tau \mapsto T(\tau, T_s) = T(\tau)$  that does not depend explicitly on the parameter  $T_s$ . This means that the temperature at a given location  $\tau$  is always the same irrespective of  $T_s$ . This temperature profile is plotted in Figure 4.2. We consider two different surface temperatures  $T_{s_1}$  and  $T_{s_2} > T_{s_1}$  with the optical depth of the entire atmosphere being  $\tau_{s_1}$  for  $T_s = T_{s_1}$  and  $\tau_{s_2} > \tau_{s_1}$  for the surface temperature  $T_{s_2}$ . The OLR resulting from the temperature profile  $\tau \mapsto T(\tau, T_{s_1})$  consists of the contribution from the region of the atmosphere above  $\tau_0$  and also from the contribution of the part of the atmosphere between  $\tau_0$  and  $\tau_{s_1}$ , meaning

from the total atmosphere. Compared to the profile  $\tau \mapsto T(\tau, T_{s_1})$ , the OLR resulting from the temperature profile  $\tau \mapsto T(\tau, T_{s_2})$ , is increased by the contribution from the region between  $\tau_{s_1}$  and  $\tau_{s_2}$ , which we assume without loss of generality to be optically as thick as the region between  $\tau_0$  and  $\tau_{s_1}$ . Since we assume that  $\tau_s$  tends to infinity with  $T_s$  to infinity (Eq. (4.1)) (and vice versa), we can put an infinite number of layers of this optical thickness into the atmosphere. Whether a Nakajima limitation occurs, depends on if and how the contribution to the OLR of these layers tends to zero with the increasing number of layers. If the increase in temperature with optical depth outweighs the increase in absorption with increasing optical depth, then the OLR is not bounded. Mathematically, the OLR given by Eq. (4.4) is bounded for the temperature profile  $\tau \mapsto T(\tau, T_s)$  ( $= T(\tau)$ ) if and only if the integral on the right hand side converges as  $T_s$  and hence  $\tau_s$  tend to infinity. Convergence of the integral is ensured if  $T(\tau)$  is smaller than  $\hat{T}(\tau)$  as the surface temperature tends to infinity (see condition (4.8) and appendix). Hence the condition (4.8) ensures that the increase in optical depth effectively shields the TOA as the surface temperature tends to infinity.

The temperature of the profile  $\tau \mapsto \hat{T}(\tau)$  on the right-hand side of Eq. (4.8) tends to infinity if  $\tau$  tends to zero. Hence, the condition (4.8) alone is not sufficient for a limitation of OLR to occur. Furthermore, except for the limits of  $\tau$  to zero and  $\tau$  to infinity, the condition (4.8) is more restrictive than condition (4.7) and is only required in the limit of  $\tau_s$  to infinity. Therefore, we state in the conditions that there should be a finite optical depth  $\tau_1$ , with the contribution of the region above  $\tau_1$  remaining finite being ensured by condition (4.7) and with the contribution of the region below  $\tau_1$  remaining finite being ensured by condition (4.8) (and also by condition (4.7) down to  $\tau_0$ ).

#### 4.4.2 The limit profile

Previous studies on the Runaway Greenhouse were all based on the tacit assumption that condition (4.8) is satisfied. In this subsection we show why this assumption is indeed correct for all physically realistic cases.

The condition (4.8) defines and uses a limit profile  $\tau \mapsto \hat{T}(\tau)$ . To obtain an idea of how restrictive this profile is in physical cases, we consider an atmosphere with a temperature profile of the form of the limit profile below an arbitrary point. We assume that our atmosphere consists of just one component; since we assume gray longwave absorption, the optical depth (measured from the TOA) is proportional to the pressure

$p$  and hence

$$\tau(p) = \frac{\kappa}{g} p \quad , \quad (4.9)$$

where  $\kappa$  is the gray gas absorption coefficient and  $g$  is the acceleration of the planet. Hence, the limit profile  $\tau \mapsto \hat{T}(\tau)$  as a function of  $p$  is

$$p \mapsto \hat{T}(p) = T_0 \cdot e^{\frac{\kappa}{4\mu g} p} \cdot \left( \frac{\kappa}{g} p \right)^{-\frac{1+\epsilon}{4}} \quad , \quad \epsilon > 0 \quad . \quad (4.10)$$

Since the temperature increases almost exponentially with pressure, this profile will for any choice of  $\kappa > 0$  and  $\epsilon$  lead to very high temperatures for large enough pressures and especially to higher temperatures than in any physically realistic case. Hence, since condition (4.8) must be satisfied only in the limit of  $T_s$  to infinity and therefore in the limit of  $p$  to infinity, condition (4.8) is always satisfied in physically realistic cases.

### 4.4.3 Application to selected temperature profiles

In this subsection, we discuss a few simple atmospheric temperature profiles in the light of the conditions (4.7) and (4.8).

#### Local radiative equilibrium

We start with an atmosphere in local radiative equilibrium (LRE). In LRE, the temperature profile  $\tau \mapsto T_{\text{LRE}}(\tau, T_s)$  is given by (e.g., Pierrehumbert (2010))

$$\tau \mapsto T_{\text{LRE}}(\tau, T_s) = \sqrt[4]{\frac{1 + \frac{1}{\mu}\tau}{2 + \frac{1}{\mu}\tau_s}} \cdot T_s \quad . \quad (4.11)$$

Eq. (4.11) implies the well-known discontinuity at the surface such that the temperature of the surface  $T_s$  is always higher than the temperature of the atmosphere at the surface  $T_{\text{LRE}}(\tau_s, T_s)$ .

We have not yet specified the relationship between  $\tau_s$  and  $T_s$ ; this relationship is crucial to determine whether a limitation of OLR exists. If  $T_s^4$  increases faster with  $\tau_s$  than  $2 + \frac{1}{\mu}\tau_s$ , the temperature at any location  $\tau$  in the atmosphere tends to infinity with  $T_s$  to infinity, and no limitation of OLR exists. In this case condition (4.7) is violated everywhere. By contrast, if  $T_s^4$  increases more slowly with  $\tau_s$  than  $2 + \frac{1}{\mu}\tau_s$ , the temperature at any finite  $\tau$  remains bounded and a Nakajima limitation exists.

Komabayashi (1967) and Ingersoll (1969) also assumed an atmosphere in LRE and found the OLR to be limited; this limit was later named Komabayashi-Ingersoll limit (Nakajima et al., 1992). The mechanism responsible for the existence of a Komabayashi-Ingersoll limit is, however, different from mechanism responsible for the existence Nakajima limitation (see Introduction). The sufficient conditions we found in this subsection, apply to the Nakajima limitation only, and not to the Komabayashi-Ingersoll limit. If we assume that the relationship between  $T_s$  and  $\tau_s$  is given by the same parameterization for the water vapor saturation curve as used by Ingersoll (1969), then the OLR attains a maximum of  $331 \text{ W m}^{-2}$ . This maximum is considerably smaller than the Komabayashi-Ingersoll limit of  $385 \text{ W m}^{-2}$  obtained with the parameterization for the water vapor saturation curve. Hence, for an atmosphere which is entirely in local radiative equilibrium the Nakajima limitation is lower than the Komabayashi-Ingersoll limit.

### Static instability

Optically thick atmospheres tend to become statically unstable close to the surface (Pierrehumbert, 2010). If in the regions where convection occurs the radiative cooling can be neglected, then the temperature follows an adiabatic profile. We assume now that the atmosphere is below a point  $\tau_{\text{trop}}$ , below which the temperature profile follows a dry adiabat:

$$\tau \mapsto T_{\text{DA}}(\tau, T_s) = T(\tau_s) \cdot \left( \frac{\tau}{\tau_s} \right)^{\frac{R}{c_p}}. \quad (4.12)$$

This temperature profile does not explicitly depend on  $T_s$  (only through  $\tau_s$ ) and hence satisfies condition (4.7), and since the profile also satisfies condition (4.8) a Nakajima limitation occurs. Note, that for the assumption of a tropospheric temperature profile, the Nakajima limitation corresponds to the tropospheric limit.

Previous studies have shown that a Nakajima limitation occurs as well if a moist adiabatic temperature profile is assumed (Abe and Matsui (1988), Kasting (1988), Nakajima et al. (1992)). Nakajima et al. (1992) showed that the limitation occurs because the temperature profile becomes independent of the surface temperature (and hence condition (4.7) is satisfied). However, no previous study has explained why the adiabatic temperature profiles becomes independent of the surface temperature, and therefore we give now such an explanation. Since an adiabatic temperature profile implies that the cooling and warming occurs at the expense of the internal energy only, at a given pressure (and hence at a given  $\tau$ ), every parcel must have the same temperature, irrespective of  $T_s$ . Increasing  $T_s$  thus just leads to a longer adiabatic

ascent to a fixed  $\tau$ . This also holds true if condensation occurs, because the latent heat release occurs within the parcel. However, if convection does not occur adiabatically, the tropospheric temperature profile may depend on  $T_s$ . If, for example, radiative heating (and cooling) affects air parcels during convective ascent and descent, then the temperature profile becomes dependent on  $T_s$  and a Nakajima limitation does not necessarily occur (see previous section on LRE).

Convection is more efficient in distributing energy in the atmosphere than is radiation in regions which are optically not too thin. Therefore, for a fixed value of the net solar irradiance, the equilibrium-surface temperature of a convective (optically thick) atmosphere with an adiabatic temperature profile is lower than for an atmosphere in LRE. Hence it appears counter-intuitive that adiabatic convection gives rise to a Nakajima limitation whereas LRE does not necessarily. However, there is a reason for this to occur. If the whole atmosphere did follow an adiabatic temperature profile, the temperature at the TOA would tend to the absolute zero. This is simply because all internal energy would be used by the gas for the expansion work. As a consequence, the region of the atmosphere that contributes to the OLR remains relatively cold, and a Nakajima limitation occurs. If, by contrast, the atmosphere is optically thin, LRE leads to a very weak vertical temperature gradient, which means that energy is well distributed and most importantly that, as long as there is upwelling radiation, the temperature at the TOA does not tend to zero. Since the temperature in the region close to the TOA is mostly determined by the intensity of the upwelling radiation, it is not a priori limited.

### **A comparison to Nakajima et al. (1992)**

In the previous two subsections we have discussed what happens if we assume that the temperature profile is determined either by LRE or by convective equilibrium. A real atmosphere would tend to be in LRE in the optically thin region close to the top of the atmosphere and convective where the atmosphere becomes optically thick. Nakajima et al. (1992) considered such an atmosphere. They assume that their atmosphere consists of two different components, a condensable gray greenhouse gas and a non-condensable transparent gas. The convective part of the atmosphere follows a pseudo-adiabatic temperature profile. Above the tropopause the atmosphere is in LRE. The position of the tropopause is assumed to be where the radiative convergence becomes positive after integrating the pseudo-adiabatic lapse rate from the surface to the top of the atmosphere. For this atmospheric model, Nakajima et al. (1992) described a limitation of OLR which was caused by the fixed temperature structure in the region

of the atmosphere which effectively emits to space, which they called the tropospheric limit. However, they did not complete their argument on why the temperature profile converges against a limit profile. They mentioned that the temperature profile in their atmosphere converged towards the moist-adiabatic profile, but this convergence alone is not sufficient for the whole temperature profile to converge, as we are going to show now.

For a Nakajima limitation to occur, we require that the temperature in the optically thin region of the atmosphere is bounded (condition (4.7)). The region above the tropopause is in LRE, and therefore the temperature of this region is determined by the upwelling radiation from the region below. Hence, if the location of the tropopause  $\tau_t$  rises fast enough to larger  $\tau$  (and hence downward in the atmosphere) with increasing surface temperature, the OLR is not bounded, since the intensity of the upwelling radiation keeps increasing. We can, however, explain why this does not happen. As pointed out by Nakajima et al. (1992), for large enough surface temperatures, at large  $\tau$  the influence of the non-condensable liquid becomes negligible and the temperature profile converges towards a moist adiabatic temperature profile. As a consequence, the pseudo-adiabatic temperature profile that Nakajima et al. (1992) assumed must also converge towards a fixed temperature profile for large surface temperatures at altitudes where water vapor is not abundant anymore, and hence up to the top of the atmosphere. Since the pseudo-adiabatic temperature profile converges towards a profile which is independent of surface temperature, both upwelling and downwelling longwave radiation also converge. Therefore the location where the net radiative heating becomes positive, which is the location of the tropopause  $\tau_t$ , also converges against a fixed value. As a consequence the whole temperature profile converges with increasing surface temperature, and a Nakajima limitation exists.

#### 4.4.4 A comparison to the conditions obtained by Sugiyama et al. (2005)

We now compare our conditions for the occurrence of a Nakajima limitation to the ones obtained for a tropospheric limit by Sugiyama et al. (2005). The “tropospheric limit” by Sugiyama et al. (2005) is a special case of the Nakajima limitation if a tropospheric temperature profile is applied. Their conditions are formulated for each wavelength separately but can easily be reformulated to the gray-atmosphere case, by integrating the condition over all wavelengths. Their sufficient conditions for a “tropospheric limit” are: 1) that the atmosphere must be optically thick enough for the surface emission not to reach the top of the atmosphere; and 2) that temperature

must become dependent only on pressure and independent of surface temperature so that the atmospheric emission is fixed. The conditions from Sugiyama et al. (2005) are mathematically not sufficient for a Nakajima limitation to occur, because the integral over the atmospheric radiative emission could still diverge even if their two conditions are satisfied. However, if a troposphere or any other physically realistic setting is assumed, then the condition (4.8) is always satisfied and if indeed the temperature profile is independent of the surface temperature, the conditions by Sugiyama et al. (2005) are sufficient for a tropospheric limit to occur.

There is a mathematical problem in the derivation of the condition by Sugiyama et al. (2005) concerning the way convergence is treated. According to Sugiyama et al. (2005), the OLR is bounded if

$$\frac{d\mathcal{O}_T(\tau_s, T_s)}{dT_s} \rightarrow 0 \quad . \quad (4.13)$$

The arrow is, however, not sufficiently well defined. It could refer to the limit of  $T_s$  to infinity or to the limit of  $T_s$  to a finite surface temperature. Either way, the condition given by Eq. (4.13) is not sufficient to ascertain that the OLR is bounded. If the limit is to be taken for  $T_s$  to a finite surface temperature, then the OLR may just increase again at a larger surface temperature. If the limit is to be taken to infinity, then  $\mathcal{O}_T \propto \sqrt{T}$  is a counter example, since  $\mathcal{O}_T$  tends to infinity even though  $d\mathcal{O}_T/dT_s$  tends to zero. The same arrow-notation is also used to state that the temperature profile must become independent of the surface temperature, and the implicit assumption is made that the temperature profile becomes independent if  $dT(\tau_s, T_s)/dT_s \rightarrow 0$ . So, even though the written form of the conditions by Sugiyama et al. (2005) are sufficient for a tropospheric limit to occur in physically realistic cases, their mathematical derivation does not allow them to state condition 1) in the form it is stated. Therefore, condition 1) was so far a hypothesis, which we have now proven.

The condition 1) by Sugiyama et al. (2005) (as stated in written form) is more restrictive than our condition (4.7). The temperature profile does not require to become independent of the surface temperature for a Nakajima limitation to occur, as suggested in condition 1. It is sufficient that the temperature at any location within the atmosphere remains bounded, as suggested by our condition (4.7). If for example the temperature at locations in the atmosphere that contribute most to the OLR were to decrease with increasing surface temperature, the temperature profile would not become independent of the surface temperature, but the OLR would be limited (at least in the considered region of surface temperature). If the temperature close to the TOA is fluctuating around a fixed profile with a limited amplitude, then the temperature

profile would again not be independent of surface temperature, even though the OLR is bounded (if the condition (4.8) is satisfied as well). For these temperature profiles, a Nakajima limitation would, however, occur according to our condition (4.7).

#### 4.4.5 Generalizations and limitations

At a first glance a major limitation of our model may be the assumption of a gray atmosphere. However, the results can also be applied to a certain degree to non-gray atmospheres. The reason is that even the atmospheric windows become opaque if only the pressure of the greenhouse gas becomes large enough. This occurs first because the absorption coefficient of the greenhouse gas may be small, but it is nonzero and hence the windows may close if there is enough greenhouse gas, and second, because the absorption band will widen due to pressure broadening. So, one may define a minimal absorption coefficient  $\kappa_{\min}$  at the frequency where the absorption is weakest and apply this absorption coefficient to the radiative transfer equations. If a temperature profile then satisfies the conditions (4.7) and (4.8), the OLR would also be bounded with the wavelength-dependent absorption coefficients. This approach is equivalent to stating the conditions (4.7) and (4.8) for each wavelength, using Planck's source function instead of  $\sigma T^4$  (as done by Sugiyama et al. (2005)). Additionally, the absorption coefficients should not be zero for any range of frequencies, independent of the amount of greenhouse gas, for the OLR to be bounded, because in this case the contribution to the OLR from this range of the spectrum would keep increasing according to Planck's source function.

The assumptions that the temperature may tend to infinity, that an infinite amount of greenhouse gas is available for evaporation, and that there is no critical point may suggest that our model is of limited use for applications to real atmospheres. However, several studies (e.g., Kasting (1988), Nakajima et al. (1992), Kopparapu et al. (2013), Goldblatt et al. (2013)) have shown that the OLR is nearly constant with increasing surface temperatures well before all of the greenhouse gas would have evaporated into the atmosphere. Hence, the mechanisms which we found to be causing a limitation of OLR are already at work at surface temperatures of practical interest.

## 4.5 Summary

In our study we extend the work by Nakajima et al. (1992) and Sugiyama et al. (2005) on the limitation of outgoing longwave radiation (OLR). We consider a plane-parallel gray atmosphere the temperature profile of which is not further specified, and we integrate the radiative-transfer equations in a two-stream approximation in order to investigate under which conditions the OLR is bounded. If the OLR is bounded according to the radiative transfer equations we speak of a Nakajima limitation. We find that a Nakajima limitation occurs if the temperature in the optically thin region of the atmosphere remains finite, and if in the optically thick region of the atmosphere the temperature does not increase faster with optical depth than the shielding effect caused by the increasing optical depth. Furthermore, we show that the conditions proposed by Sugiyama et al. (2005) are sufficient for a Nakajima limitation to occur, but they are more restrictive than our conditions. We show further that an atmosphere in local radiative equilibrium does not necessarily exhibit a Nakajima limitation. However, if we assume that the atmosphere is saturated, we find that an atmosphere in radiative equilibrium exhibits a maximum of OLR which is lower than the maximum caused by the effect described by Ingersoll (1969). Therefore, an atmosphere which is in local radiative equilibrium would attain a Runaway Greenhouse at a TSI which is lower than previously assumed. We show, furthermore, that for tropospheric conditions, the occurrence of a Nakajima limitation depends crucially on the assumption that the temperature profile is exclusively determined by adiabatic convection. Therefore, temperature profiles should always be calculated dynamically in studies in which a possible limitation of OLR is of importance.

## 4.A Mathematical principles of the Nakajima limitation

If

- 1.)  $T(\tau, T_s) \in \mathbb{R}_{\geq 0}$ ,  $\forall \tau, T_s \in \mathbb{R}_{\geq 0}$
- 2.)  $\lim_{T_s \rightarrow \infty} \tau_s(T_s) = \lim_{\tau_s \rightarrow \infty} \tau_s = \infty$
- 3.)  $\exists \beta \in \mathbb{R}_{> 0}$ , such that  $T_s \leq \beta \cdot T(\tau_s, T_s)$ ,  $\forall T_s, \tau_s \in \mathbb{R}_{\geq 0}$
- 4.)  $\exists T_{s_0}, \tau_0, T_a \in \mathbb{R}_{\geq 0}$ , such that  $T(\tau, T_s) \leq T_a$ ,  $\forall T_s \geq T_{s_0}$ ,  $\forall \tau \leq \tau_0$
- 5.)  $\exists \tau_1 \leq \tau_0$  and  $\exists \epsilon > 0$ , such that  $T(\tau, T_s) \leq \hat{T}(\tau) \equiv T_c \cdot e^{\frac{1}{4\mu}\tau} \cdot \tau^{-\frac{1+\epsilon}{4}}$ ,  
 $T_c \in \mathbb{R}_{\geq 0}$ ,  $\forall \tau > \tau_1$ ,  $\forall T_s$

then  $\mathcal{O}_T(\tau_s, T_s)$  remains bounded  $\forall T_s, \tau_s \in \mathbb{R}_{\geq 0} \cup \infty$ .

*Proof.* From 1.) it follows that for any finite  $T_s$  the temperature remains finite throughout the atmosphere and hence does the OLR. So it is sufficient to show that  $\mathcal{O}_T(\tau_s, T_s)$  remains bounded as  $T_s$  tends to infinity:

$$\begin{aligned}
\lim_{T_s \rightarrow \infty} \mathcal{O}_T(\tau_s, T_s) &= \lim_{T_s \rightarrow \infty} \sigma T_s^4 \cdot e^{-\frac{\tau_s}{\mu}} + \lim_{T_s \rightarrow \infty} \int_0^{\tau_s} \sigma T^4(\tilde{\tau}, T_s) e^{-\frac{\tilde{\tau}}{\mu}} \frac{1}{\mu} d\tilde{\tau} \\
&= \lim_{T_s \rightarrow \infty} \sigma T_s^4 \cdot e^{-\frac{\tau_s}{\mu}} + \lim_{T_s \rightarrow \infty} \int_0^{\tau_0} \sigma T^4(\tilde{\tau}, T_s) e^{-\frac{\tilde{\tau}}{\mu}} \frac{1}{\mu} d\tilde{\tau} \\
&\quad + \lim_{T_s \rightarrow \infty} \int_{\tau_0}^{\tau_s} \sigma T^4(\tilde{\tau}, T_s) e^{-\frac{\tilde{\tau}}{\mu}} \frac{1}{\mu} d\tilde{\tau} \\
&\leq \lim_{T_s \rightarrow \infty} \underbrace{\sigma (\beta T(\tau_s, T_s))^4}_{3.)} \cdot e^{-\frac{\tau_s}{\mu}} + \lim_{T_s \rightarrow \infty} \underbrace{\int_0^{\tau_0} \sigma T_a^4 \cdot e^{-\frac{\tilde{\tau}}{\mu}} \frac{1}{\mu} d\tilde{\tau}}_{4.)} \\
&\quad + \lim_{T_s \rightarrow \infty} \underbrace{\int_{\tau_0}^{\tau_s} \sigma \hat{T}^4(\tilde{\tau}) e^{-\frac{\tilde{\tau}}{\mu}} \frac{1}{\mu} d\tilde{\tau}}_{5.)} \\
&\leq \lim_{\tau_s \rightarrow \infty} \underbrace{\sigma (\beta \hat{T}(\tau_s))^4}_{2.)} \cdot e^{-\frac{\tau_s}{\mu}} + \sigma T_a^4 \left(1 - e^{-\frac{\tau_0}{\mu}}\right) \\
&\quad + \lim_{\tau_s \rightarrow \infty} \underbrace{\int_{\tau_0}^{\tau_s} \sigma \hat{T}^4(\tilde{\tau}) e^{-\frac{\tilde{\tau}}{\mu}} \frac{1}{\mu} d\tilde{\tau}}_{2.)} \\
&= \sigma T_a^4 \left(1 - e^{-\frac{\tau_0}{\mu}}\right) + \frac{\tau_0^{-\epsilon}}{\mu \epsilon} \sigma T_c^4 < \infty
\end{aligned}$$

□

# Chapter 5

## Conclusions

### 5.1 Answers to the research questions

Based on the simulations I performed with the single-column version (Chapter 2) and the three-dimensional version (Chapter 3) of ECHAM6, and based on my theoretical investigations with the gray-atmosphere model (Chapter 4), I now give concise answers to the questions posed in the introduction of the thesis (Chapter 1). For more details please refer to the main chapters.

**What TSI is necessary to cause a climate instability when starting from a present-day Earth-like climate? Would this climate instability prevent an Earth-like planet from attaining the Moist Greenhouse regime?**

Based on my three-dimensional simulations of an aqua-planet with ECHAM6, I conclude that a TSI between  $1.06 S_0$  and  $1.08 S_0$  is necessary to destabilize a present-day Earth-like climate. The maximum global-mean surface temperature attained in the present-day Earth-like climate is only 296 K. The transition does not lead to a Runaway Greenhouse, but leads to a new steady state with a global-mean surface temperature of around 340 K. This steady state is in the Moist Greenhouse regime, because the stratosphere is sufficiently moist for a rapid loss of hydrogen to space. The aqua-planet remains in the Moist Greenhouse regime for a TSI of at least up to  $1.2 S_0$ . The single-column is not able to represent the Moist Greenhouse and is therefore not suited to answer the above research questions.

**What is the influence of clouds on the critical TSI for the onset of a Runaway Greenhouse? How do clouds influence the energy balance in warm climates?**

The results obtained with the single-column version of ECHAM6 suggest that the critical TSI to trigger a Runaway Greenhouse is increased from 1.10 - 1.12  $S_0$  for clear-

sky conditions to at least 1.50-1.70  $S_0$  for full-sky conditions. The higher cloud albedo allows the climate to remain in equilibrium for markedly higher values of TSI. In warm climates, clouds provide a very strong negative feedback, because the cloud albedo increases with TSI while the OLR remains unchanged. The simulations of the aqua-planet reveal that the cloud feedback is positive for global-mean surface temperatures up to 330 K, but becomes negative at higher temperatures. As in the single-column model, clouds also provide a very strong negative feedback in the warm regime in the simulations of the aqua-planet.

**How does the global circulation differ between a present-day Earth-like climate and a much warmer climate? How does the circulation affect the cloud formation in a warm climate?**

In the three-dimensional simulations of an aqua-planet with ECHAM6 I find that stable warm climates exist with global-mean surface temperatures of around 340 K. These warm climates are characterized by a low meridional surface-temperature gradient, a weak meridional circulation without polar cells, a moist stratosphere, and convection-dominated cloud formation. The Hadley circulation is much weaker in the warm climate than in the present-day Earth-like climate, and the Hadley cells extend further poleward. The weaker Hadley circulation leads to an increase in convective events in the subsidence region, and hence the cloud cover in this region is considerably larger in the warm climate.

**Which properties of a temperature profile cause the OLR to be limited? Do physically realistic assumptions lead to profiles with such properties?**

In the gray-atmosphere model I find that any temperature profile satisfying the following two conditions leads to a limitation of OLR: 1. The temperature remains finite in the optically thin region of the atmosphere, and 2. in the optically thick region of the atmosphere, the temperature does not increase faster with optical depth than a nearly-exponentially increasing limit profile. In physically relevant settings, the latter condition is always satisfied. Tropospheric conditions lead to a limitation of OLR if the convection occurs completely adiabatically and additionally the energy transport by radiation can be neglected. In an entirely statically stable atmosphere, the occurrence of a limitation of OLR depends crucially on the boundary conditions at the surface of the temperature profile.

## 5.2 Synthesis and implications

### 5.2.1 Differences between the effects of solar forcing on the climate of an aqua-planet and of CO<sub>2</sub>-induced forcing on Earth's climate

Present discussions in climate science are focused on CO<sub>2</sub>-induced forcing and the associated global warming rather than on solar forcing. In this context, it is interesting to compare the effects of the solar forcing on the climate of my three-dimensional aqua-planet with the effects of a CO<sub>2</sub>-induced forcing of similar magnitude on Earth's climate. Increasing the TSI from 1.00 S<sub>0</sub> to 1.06 S<sub>0</sub> leads to a global-mean radiative imbalance of 12 W m<sup>-2</sup> on average over the first year of my aqua-planet simulation. A similar global-mean radiative-imbalance is attained in a three-dimensional simulation with ECHAM6 for present-day Earth when the atmospheric concentration of CO<sub>2</sub> is increased to eight times the preindustrial value (Meraner et al., 2013). The two radiative forcings lead to an increase in steady-state global-mean surface temperature of 6.4 K for my aqua-planet and of 12 K for present-day Earth (Meraner et al., 2013), respectively. Hence, the temporal-mean climate sensitivity deduced from these values is smaller for the aqua-planet (0.53 K / (W m<sup>-2</sup>)) than for Earth (1 K / (W m<sup>-2</sup>)). Possible causes for the discrepancy in climate sensitivity are the absence of sea-ice and land on the aqua-planet, the difference in initial surface temperatures, the difference between the obliquity of the two planets, and the difference in the meridional distribution between solar forcing and CO<sub>2</sub>-induced forcing.

My model simulations of the aqua-planet show that a TSI between 1.06 S<sub>0</sub> and 1.08 S<sub>0</sub> is necessary to destabilize a present-day Earth-like climate. With an albedo of 0.3, this corresponds to an instantaneous global-mean radiative imbalance of between 14 W m<sup>-2</sup> and 19 W m<sup>-2</sup>. Since I did not perform simulations where the TSI is increased directly from 1.00 to 1.08 S<sub>0</sub>, I cannot assess the fast feedbacks for such an increase of TSI. According to Meraner et al. (2013) even an instantaneous imbalance of 19 W m<sup>-2</sup> caused by increasing the atmospheric CO<sub>2</sub> concentrations to 4480 ppm would not lead to a climate instability. This raises two interesting questions. First, does the climate instability not occur in Meraner et al. (2013) because their model is forced by increasing the atmospheric CO<sub>2</sub> concentrations or because of the differences between Earth and my aqua-planet? Second, why is the climate of the aqua-planet less sensitive to small solar forcings than present-day Earth is to CO<sub>2</sub>-induced forcing of similar magnitude in the cold regime but then destabilizes for smaller radiative forcings than present-

day Earth does? These two questions should be tackled in future studies by either increasing atmospheric CO<sub>2</sub> concentrations on the aqua-planet or by increasing the TSI on Earth.

## 5.2.2 A look into Earth's far future

My three-dimensional simulations imply that an aqua-planet on an Earth-like orbit would remain in a present-day Earth-like climate for a TSI of up to 1.06 or 1.08  $S_0$ . The most important differences between Earth and the aqua-planet in my simulations are the different obliquity and the absence of sea ice (and land) on the aqua-planet. These differences could have a multitude of effects, the totality of which can only be investigated by GCM simulations of Earth for increased values of TSI. In the following discussion I will therefore just assume that the results of the aqua-planet also apply to Earth. Assuming an increase of TSI of 9 % per billion years, Earth would remain in a present-day-like climate for the next 650 to 880 million years before going into the Moist Greenhouse regime, where it would remain for at least another billion years. In this time, Earth would lose considerable amounts of water. However, based on the estimates by Abe et al. (2011), a billion years in the Moist Greenhouse would not suffice to lose all water with the stratospheric volume mixing ratios I found on my aqua-planet. The results of the experiments with the single-column version of ECHAM6 suggest that a steady state could be maintained even for much larger TSIs. However, the single-column version was not able to represent the Moist Greenhouse, because of the inability of that model to mix water vapor into the stratosphere. Nonetheless, the increase in cloud cover with increasing TSI, which allowed the column to remain in equilibrium for large values of the TSI, is also a feature of the Moist Greenhouse regime in the three-dimensional aqua-planet simulations. Therefore, I expect that Earth will remain in the Moist Greenhouse regime until nearly all water is lost, and I expect a Runaway Greenhouse to be a rather unlikely scenario for Earth. The situation may become interesting once water becomes scarce at the surface. On the one hand, if cloud cover decreases as the planet dries, the remaining water could evaporate in a Runaway Greenhouse. On the other hand, Abe et al. (2011) hypothesized that once nearly all water is lost, the planet could transform into a land planet, which their simulations suggest to be habitable for TSIs of up to 1.7  $S_0$ . The transition to a land planet, that is, the transition from a water-covered surface to a land surface, has not been investigated and should be subject of further studies.

How may this future affect life on Earth? Some simple lifeforms are known to be able to grow in most extreme conditions such as temperatures as high as 113 C° (Pikuta

et al., 2007). Therefore, such simple lifeforms would certainly be able to survive for a long time in the Moist Greenhouse regime, since temperatures in my simulations do not exceed  $80^{\circ}$  C even with a TSI of  $1.2 S_0$ . However, for complex organisms the situation would be more difficult in hot climates. In my three-dimensional simulations, once the aqua-planet attains the Moist Greenhouse, the annual-mean surface temperatures even at the poles do not fall much below  $60^{\circ}$  C. On Earth, lower annual mean temperatures could be expected at higher elevations. Chlorophyll remains stable up to temperatures of around  $75^{\circ}$  C (Rothschild and Mancinelli, 2001). Therefore, well-adapted plants could probably survive for quite some time in the Moist Greenhouse regime in niches at high elevations. These plants could then form the base for a foodchain.

### 5.2.3 Early Venus

Measurements of the ratio of deuterium to hydrogen in the Venusian atmosphere suggest that Venus may have lost considerable amounts of water (Donahue et al. (1982), Debergh et al. (1991)). So Venus may have been a habitable planet in the past. The TSI of Venus was between  $1.34 S_0$  and  $1.43 S_0$  (Newman and Rood, 1977) when the sun reached the main sequence 4.5 billion years ago. Applied to early Venus, the three-dimensional results I obtain with the aqua-planet thus suggest that Venus never had a present-day Earth-like climate. The results of the single-column model would suggest that the TSI was too low for a Runaway Greenhouse to occur. Unfortunately, I could not run the three-dimensional aqua-planet to large enough TSIs to confirm this result. I can, however, conclude from the three-dimensional simulations of the aqua-planet that early Venus was likely in a Moist Greenhouse state or in a post-Runaway-Greenhouse state. In both cases, early Venus would have been subject to a rapid loss of water.

### 5.2.4 The habitable zone of our solar system

The three-dimensional results I obtain with the aqua-planet have interesting implications for the habitable zone of our solar system. A low-obliquity water-rich planet with a similar rotation rate as Earth on an orbit with low eccentricity is safe from a rapid loss of water down to a distance of about 0.97 AU from the sun. But the loss of water does not immediately render a planet uninhabitable, so a planet would become uninhabitable at 0.97 AU after a certain time only. The "hard" inner edge of the habitable zone is the TSI at which a Runaway Greenhouse occurs. According to the results I obtain with the aqua-planet, the hard inner edge is at shorter distance than 0.91 AU

from the sun and the results I obtain with the single-column model suggest that the inner edge is even much closer to the sun (0.80 - 0.82 AU).

It would be interesting to investigate how sensitive the values I obtained for the inner edge of the habitable zone would be to changes of orbital parameters, such as the obliquity of the planet. The obliquity of the planet has a large influence on the global circulation. Since the effect on clouds of the weakening of the circulation with increasing SST is ultimately responsible for destabilizing the present-day Earth-like climate in my three-dimensional aqua-planet simulations, the critical TSI to destabilize such a climate likely depends on the obliquity of the planet, and so does its habitability.

The results by Abe et al. (2011) suggest that a land planet would remain habitable for considerably larger TSI than an aqua-planet. But already the presence of continents on a partially ocean-covered planet, such as Earth, likely has an influence on the TSI required to destabilize a present-day Earth-like climate, because large land masses do not only have an influence on the circulation, but also directly on the atmospheric moisture and thus on clouds. How large the influence on the critical TSI is, certainly also depends on the geographical distribution of the land, and is left to future studies.

### **5.2.5 The Runaway Greenhouse at different stages of stellar evolution**

My results suggest that a water-rich planet on an Earth-like orbit would go into the Moist Greenhouse regime as the TSI increases and that it remains in that regime for a considerable amount of time. In the case of our sun, it is hence unlikely, yet not impossible, that such a planet goes into a Runaway Greenhouse. However, the situation may be different for Earth-like planets around other stars or for a hypothetical Earth-like planet on a different orbit around our sun. Hence, I am discussing now under which conditions an Earth-like planet could go into a Runaway Greenhouse before most of the water is lost. I always assume here that the TSI would eventually become large enough for a Runaway Greenhouse to occur and I do not consider changes in the emission spectra of stars (except for extreme ultra-violet radiation).

An Earth-like planet is likely to go into a Runaway Greenhouse before most water is lost in the Moist Greenhouse regime if the luminosity of the star it orbits increases considerably faster with time than the luminosity of our sun currently does. The rate of increase of the luminosity of stars in the main sequence increases with both their age and their mass. So, Earth-like planets around more massive stars and Earth-like

planets which attain the Moist Greenhouse "late" in their star's lifetime are more likely to encounter a Runaway Greenhouse.

The rate at which hydrogen escapes to space depends on the intensity of the incoming solar extreme ultra-violet radiation. Abe et al. (2011) estimate that the extreme ultra-violet radiation presently emitted by our sun would make the loss of an Earth-like ocean impossible in under 600 million years. Weaker emissions of extreme ultra-violet radiation would extend the minimum time required to lose an Earth-like ocean even further. Hence, water-rich planets around stars with weak extreme ultra-violet emissions will be more likely to encounter a Runaway Greenhouse. The emission of extreme ultra-violet radiation of sun-like stars is supposed to decrease over time during the main sequence (Ribas et al., 2005). Thus, the temporal evolution of both the TSI and of the extreme ultra-violet spectrum suggest that planets around sun-like stars which attain the Moist Greenhouse "late" in their star's lifetime are more likely to encounter a Runaway Greenhouse.

### 5.2.6 Simulation of an entire Runaway Greenhouse

Hitherto, a dynamical simulation covering an entire Runaway Greenhouse has not been attempted. Previous studies on the Runaway Greenhouse have either only treated a limited range of temperatures or have studied radiative fluxes for prescribed temperature profiles. However, in Chapter 4 I point out that it is crucial to calculate the temperature profile dynamically in the context of the Runaway Greenhouse. Evaporation of an Earth-sized ocean would lead the liquid-gas boundary to the critical point of water, which existing models are not able to deal with appropriately. The modifications I introduced to ECHAM6 in order to run the model at higher temperatures are not sufficient to get even close to the critical point. An appropriate approximation of the equation of state near the critical point of water and an accurate calculation of the optical properties of the gas in the region would be necessary. Furthermore, the atmosphere and the ocean of the model would have to be treated as two phases of one fluid in order to be able to simulate the transition from the liquid phase to the super-critical phase. Developing a model satisfying these requirements is a challenging task left for future studies. But the prospect of deepening fundamentally not only our understanding of the Runaway Greenhouse but also generally of hot steam atmospheres is certainly worth the effort.



---

# Appendix A

## Appendix

### A.1 Moist physics in ECHAM6

Most of the physics in ECHAM6 are based on the assumption that the mass of water vapor in the atmosphere is negligible compared to the mass of dry air. In this case the pressure  $p$  of a column of dry air corresponds closely to the pressure  $P$  of a column of moist air and the mass mixing ratio of water vapor  $x_v$  corresponds closely to the specific humidity  $q_v$ . However, if water vapor becomes an important atmospheric constituent the approximation may lead to considerable errors. Therefore we apply changes to the physics using more generalized formulations. We will henceforth make the distinction between the abstract coordinates levels  $(v_i)_{i=0,\dots,n}$  and the abstract coordinates layers  $(l_i)_{i=0,\dots,n-1}$ . A layer  $l_{j-1}$  denotes the region between the level  $v_j$  and  $v_{j-1}$  for any  $j \in \{1, \dots, n\}$ . The level  $v_0$  denotes the top of the atmosphere and accordingly  $l_0$  is the upper most layer. Levels are exclusively reserved for pressures. All other quantities like temperature or specific humidity are defined for layers. However, pressures are also calculated for layers by calculating the mean of the two adjunct level pressures.

#### A.1.1 Pressure

Let  $P(v_j)$  be the pressure of moist air,  $p(v_j)$  the partial pressure of dry air and  $\tilde{p}(v_j)$  the pressure of a column of dry air at the level  $v_j$ . The difference between  $p(v_j)$  and  $\tilde{p}(v_j)$  is that for the calculation of  $p(v_j)$  the mass of the water vapor of the layers above  $v_j$  is taken into account, whereas water vapor is completely ignored for  $\tilde{p}(v_j)$ . The model pressure of ECHAM6 is always  $\tilde{p}(v_j)$  and hence water vapor is completely ignored. In order to find relations between the different pressures we also require the

partial pressure of water vapor  $e(v_j)$  at the level  $v_j$ . According to Dalton's law we can write

$$P(v_j) = p(v_j) + e(v_j) \quad . \quad (\text{A.1})$$

The difference in total Pressure between the level  $l_j$  and  $l_{j-1}$  corresponds to

$$P(v_j) - P(v_{j-1}) = \frac{m(l_{j-1}) \cdot g}{A} \quad , \quad (\text{A.2})$$

where  $m(l_{j-1})$  is the mass of the layer  $l_{j-1}$ ,  $g$  is Earth's acceleration and  $A$  is the unit surface. Since masses are additive we can write

$$P(v_j) - P(v_{j-1}) = \frac{(m_d(l_{j-1}) + m_v(l_{j-1})) \cdot g}{A} \quad , \quad (\text{A.3})$$

with  $m_d(l_{j-1})$  the mass of dry air and  $m_v(l_{j-1})$  the mass of water vapor. The specific humidity  $q_v(l_k)$  is defined as

$$q_v(l_k) = \frac{m_v(l_k)}{m_d(l_k) + m_v(l_k)} \quad , \quad \forall k \in \{1, \dots, n\} \quad . \quad (\text{A.4})$$

Hence  $m_v(l_{j-1})$  can be expressed as

$$m_v(l_{j-1}) = \frac{q_v(l_{j-1})}{1 - q_v(l_{j-1})} \cdot m_d(l_{j-1}) \quad . \quad (\text{A.5})$$

Replacing  $m_v(l_{j-1})$  and factoring out  $m_d(l_{j-1})$  in Eq. (A.3) yields

$$\begin{aligned} P(v_j) - P(v_{j-1}) &= \left(1 + \frac{q_v(l_{j-1})}{1 - q_v(l_{j-1})}\right) \cdot \frac{m_d(l_{j-1})g}{A} \\ &= \frac{1}{1 - q_v(l_{j-1})} \cdot \frac{m_d(l_{j-1})g}{A} \quad . \end{aligned} \quad (\text{A.6})$$

The mass of dry air  $m_d(l_{j-1})$  of the layer  $l_{j-1}$  can be expressed as

$$m_d(l_{j-1}) = \frac{A \cdot (\tilde{p}(v_j) - \tilde{p}(v_{j-1}))}{g} \quad . \quad (\text{A.7})$$

Applying the term for  $m_d(l_{j-1})$  to Eq. (A.6) finally leads to

$$P(v_j) - P(v_{j-1}) = \frac{1}{1 - q_v(l_{j-1})} \cdot (\tilde{p}(v_j) - \tilde{p}(v_{j-1})) \quad (\text{A.8})$$

or

$$P(v_j) = P(v_{j-1}) + \frac{1}{1 - q_v(l_{j-1})} \cdot (\tilde{p}(v_j) - \tilde{p}(v_{j-1})) \quad . \quad (\text{A.9})$$

Eq. (A.9) is a recursive formula for  $Pv_j$ . If  $v_0$  denotes the top of the atmosphere then

$$P(v_0) = \tilde{p}(v_0) = 0 \quad , \quad (\text{A.10})$$

and hence we can integrate the total pressure down to any desired level. Since  $q_v(l_{j-1})$  and  $\tilde{p}(v_j)$  are prognostic variables in ECHAM6 for all  $j \in \{1, \dots, n+1\}$ , Eqs. (A.9) and (A.10) allow to transform the model pressure  $\tilde{p}(v_j)$  (for a column of dry air) to the total pressure  $P$  including the mass of water vapor.

In the following subsections, all calculations are performed within single layers. Therefore, we will henceforth drop the layer coordinates.

### A.1.2 Specific humidity

The specific humidity is a prognostic variable in ECHAM6 and does not require adaptation. However, the processes leading to tendencies of the specific humidity do require modifications. The specific humidity  $q_v$  of any layer changes as a consequence of transport of water vapor and dry air as well as due to phase changes. We first consider phase changes. The most important quantity related to phase changes in ECHAM6 is the specific humidity of saturation  $Q$ .  $Q$  is a diagnostic variable and therefore we have to derive the correct formula for  $Q$  which is defined as

$$Q = \frac{M}{M + m_d} \quad , \quad (\text{A.11})$$

where  $M$  is the mass of water vapor required for saturation and  $m_d$  is the mass of dry air. Since we assume  $M$  and  $m_d$  to occupy the same volume we obtain

$$\begin{aligned} Q &= \frac{M}{M + m_d} \\ &= \frac{V \cdot \rho_s}{V \cdot (\rho_s + \rho_d)} \\ &= \frac{\rho_s}{\rho_s + \rho_d} \quad , \end{aligned} \quad (\text{A.12})$$

where  $\rho_s$  is the density of water vapor required for saturation and  $\rho_d$  is the density of dry air. The equation of states for the ideal gas allows us to rewrite

$$\begin{aligned} \rho_d &= \frac{p}{R_d T} \\ \rho_s &= \frac{E}{R_v T} \quad , \end{aligned} \quad (\text{A.13})$$

where  $p$  is the partial pressure of dry air and  $E$  is the pressure of water vapor at saturation.  $T$  is the temperature of the layer.  $R_d$  and  $R_v$  denote the specific gas constants of dry air and water vapor respectively. By applying the Eqs. (A.13) to Eq. (A.12) we obtain

$$\begin{aligned} Q &= \frac{\rho_s}{\rho_s + \rho_d} \\ &= \frac{\frac{E}{R_v T}}{\frac{E}{R_v T} + \frac{p}{R_d T}} \\ &= \frac{\frac{R_d}{R_v} \cdot E}{\frac{R_d}{R_v} \cdot E + p} . \end{aligned} \quad (\text{A.14})$$

Unfortunately  $p$  is not known. But according to Dalton's law we can write  $p$  as

$$p = P - e \quad , \quad (\text{A.15})$$

where the  $P$  is the pressure of moist air and  $e$  is the partial pressure of water vapor. Hence we can rewrite Eq. (A.14) to obtain

$$Q = \frac{\frac{R_d}{R_v} \cdot E}{\frac{R_d}{R_v} \cdot E + (P - e)} . \quad (\text{A.16})$$

The partial pressure of water vapor can be expressed with the help of the specific humidity  $q$ :

$$\begin{aligned} q &= \frac{m_v}{m_v + m_d} \\ &= \frac{\rho_v}{\rho_v + \rho_d} \\ &= \frac{\frac{R_d}{R_v} \cdot e}{\frac{R_d}{R_v} \cdot e + p} \end{aligned} \quad (\text{A.17})$$

$m_v$  and  $\rho_v$  denote the mass and the density of water vapor respectively. Solving Eq. (A.17) for  $e$  yields

$$e = \frac{P \cdot q}{\frac{R_d}{R_v} + (1 - \frac{R_d}{R_v})q} . \quad (\text{A.18})$$

The saturation pressure of water vapor is a function of the temperature only and  $E = E(T)$  can be obtained from a lookup table. Hence, by using the Eqs. (A.16) and (A.18) we can calculate  $Q$ .

### A.1.3 Relative humidity

The relative humidity  $r$  of any layer is defined as

$$r = \frac{e}{E} \quad , \quad (\text{A.19})$$

where  $e$  is the partial pressure of water vapor and  $E$  is the partial pressure of saturation of water vapor. Similarly to the previous subsection, we can express  $e$  using the specific humidity  $q$  as

$$\begin{aligned} q &= \frac{\frac{R_d}{R_v} \cdot e}{\frac{R_d}{R_v} \cdot e + p} \\ \Leftrightarrow e &= \frac{q \cdot p}{\frac{R_d}{R_v} \cdot (1 - q)} \quad , \end{aligned} \quad (\text{A.20})$$

where  $p$  denotes the partial pressure of dry air. The same calculation can be performed for  $E$  using the specific humidity of saturation  $Q$ :

$$\begin{aligned} Q &= \frac{\frac{R_d}{R_v} \cdot E}{\frac{R_d}{R_v} \cdot E + p} \\ \Leftrightarrow E &= \frac{Q \cdot p}{\frac{R_d}{R_v} \cdot (1 - Q)} \quad . \end{aligned} \quad (\text{A.21})$$

By applying the terms for  $e$  and  $E$  given by the Eqs. (A.20) and (A.21) respectively to the definition of the relative humidity (A.19) we obtain

$$\begin{aligned} r &= \frac{q \cdot p}{\frac{R_d}{R_v} \cdot (1 - q)} \cdot \frac{\frac{R_d}{R_v} \cdot (1 - Q)}{Q \cdot p} \\ &= \frac{1 - Q}{1 - q} \cdot \frac{q}{Q} \quad . \end{aligned} \quad (\text{A.22})$$

Hence we can express the relative humidity by using the variable  $Q$  (calculated as described in the previous subsection) and the prognostic variable  $q$ .

### A.1.4 Density

The total density  $\rho$  of any layer can be written as the sum of the densities of its constituents

$$\rho = \rho_d + \rho_v + \rho_l + \rho_i \quad , \quad (\text{A.23})$$

where  $\rho_d$ ,  $\rho_v$ ,  $\rho_l$  and  $\rho_i$  are the density with respect to the whole volume of dry air, of water vapor, of liquid water and of water ice respectively. We define the mass mixing ratios for water vapor  $v$ , liquid water  $l$  and water ice  $i$  as

$$x_\alpha = \frac{\rho_\alpha}{\rho_d} \quad \alpha = v, l, i \quad , \quad (\text{A.24})$$

and rewrite the Eq. (A.23) as

$$\begin{aligned} \rho &= \rho_d \cdot \left( 1 + \frac{\rho_v}{\rho_d} + \frac{\rho_l}{\rho_d} + \frac{\rho_i}{\rho_d} \right) \\ &= \rho_d \cdot (1 + x_v + x_l + x_i) \quad . \end{aligned} \quad (\text{A.25})$$

We can find an expression for  $\rho_d$  by using Dalton's law and the equation of state of the ideal gas:

$$\begin{aligned} P &= p_d + e \\ &= \rho_d R_d T + \rho_v R_v T \\ &= \rho_d R_d T + \rho_v R_v T \cdot \frac{\rho_d R_d}{\rho_d R_d} \\ &= \rho_d R_d T \left( 1 + \frac{R_v \rho_v}{R_d \rho_d} \right) \\ &= \rho_d R_d T \left( 1 + \frac{R_v}{R_d} \cdot x_v \right) \\ \Leftrightarrow \rho_d &= \frac{P}{R_d T} \left( 1 + \frac{R_v}{R_d} \cdot x_v \right)^{-1} \end{aligned} \quad (\text{A.26})$$

By applying the term for  $\rho_d$  to Eq. (A.25) we obtain

$$\rho = \frac{P}{R_d T} \cdot \frac{1 + x_v + x_l + x_i}{1 + \frac{R_v}{R_d} \cdot x_v} \quad . \quad (\text{A.27})$$

Eq. (A.27) allows to determine  $\rho$  using only constants and prognostic variables of ECHAM6.

The density of the gaseous components  $\rho_{gas}$  can be expressed by starting from Eq. (A.27) and dropping the mixing ratios  $x_l$  and  $x_i$ . We obtain

$$\begin{aligned}
 \rho_{gas} &= \frac{P}{R_d T} \cdot \frac{1 + x_v}{1 + \frac{R_v}{R_d} \cdot x_v} \\
 &= \frac{P}{T} \cdot \frac{1 + \frac{\rho_v}{\rho_d}}{R_d + R_v \frac{\rho_v}{\rho_d}} \\
 &= \frac{P}{T} \cdot \frac{\rho_d + \rho_v}{R_d \rho_d + R_v \rho_v} \\
 &= \frac{P}{T} \cdot \frac{1}{(1 - q)R_d + qR_v} \quad ,
 \end{aligned} \tag{A.28}$$

where  $q$  is the specific humidity of water vapor. If  $x_l$  and  $x_i$  are negligible then  $\rho = \rho_{gas}$ .

### A.1.5 Specific gas constants

For a mixture of gases like moist air the gas constant is different from the gas constant of either water vapor or dry air. According to the equation of state we can write

$$\rho = \frac{P}{R_m T} \quad , \tag{A.29}$$

where  $R_m$  is the specific gas constant of moist air. If no condensate is present or if the amount is of condensate negligible, we can apply this equation to Eq. (A.28) and by solving for  $R_m$  we obtain

$$\begin{aligned}
 R_m &= \frac{R_d \rho_d + R_v \rho_v}{\rho_d + \rho_v} \\
 &= (1 - q) \cdot R_d + q \cdot R_v \quad ,
 \end{aligned} \tag{A.30}$$

where  $q$  is the specific humidity.

In a few places in ECHAM6 Eq. (A.29) is applied to Eq. (A.28). Solving for  $R_m$  then yields

$$R_m = \frac{R_d + R_v \cdot x_v}{1 + x_v + x_l + x_i} \quad , \tag{A.31}$$

or by expanding the fraction with  $\rho_d$  we obtain

$$R_m = \frac{R_d \rho_d + R_v \rho_v}{\rho_d + \rho_v + \rho_l + \rho_i} \quad . \tag{A.32}$$

In Eq. (A.32)  $R_m$  is not calculated consistently, because the condensate does not behave like an ideal gas. Since Eq. (A.32) is, however, only used to handle density in

a convenient way in ECHAM6, we kept the equation where the approximation thereof was used in the original code.

### A.1.6 Density- and virtual temperatures

The density temperature  $T_{dens}$  of any layer is defined as

$$T_{dens} = \frac{1 + \frac{R_v}{R_d} \cdot x_v}{1 + x_v + x_l + x_i} \cdot T \quad , \quad (\text{A.33})$$

where  $T$  is the temperature of the layer,  $R_d$  and  $R_v$  are the gas constants of dry air and water vapor respectively and the mixing ratios  $x_v$ ,  $x_l$  and  $x_i$  are defined as in the previous subsection. We note that according to Eq. (A.27) the density temperature satisfies

$$\rho = \frac{P}{R_d T_{dens}} \quad . \quad (\text{A.34})$$

The virtual temperature  $T_{vir}$  of is defined as

$$T_{vir} = ((1 - q)R_d + qR_v) \cdot T \quad , \quad (\text{A.35})$$

where  $q$  is the specific humidity. We note that according to Eq. (A.28) the virtual temperature satisfies

$$\rho_{gas} = \frac{P}{R_d T_{vir}} \quad . \quad (\text{A.36})$$

We define accordingly the potential density temperature as

$$\Theta_{dens} = \frac{1 + \frac{R_v}{R_d} \cdot x_v}{1 + x_v + x_l + x_i} \cdot \Theta \quad , \quad (\text{A.37})$$

where  $\Theta$  is the potential temperature. The virtual potential temperature is defined as

$$\Theta_{vir} = ((1 - q)R_d + qR_v) \cdot \Theta \quad . \quad (\text{A.38})$$

## A.2 Modifications of the Radiation Code

### A.2.1 Molecular absorption coefficients

Most of the molecular absorption coefficients required for the radiative transfer scheme implemented in ECHAM6 are dependent on temperature. However, the range of temperature for which values exist in the lookup-tables of these coefficients is limited to temperatures well below 400 K. If the model temperatures exceed the range of lookup-tables the values for the absorption coefficient are linearly extrapolated. If values of the coefficients decrease with increasing temperatures, the linear extrapolation will eventually lead to negative absorption coefficients. Moreover, with the correlated-k method which is used for the radiative transfer calculations the coefficients in the so called g-space (Lacis and Oinas, 1991) may decrease in certain regions even if the absorption coefficients increase with temperature. This leads to problems in ECHAM6, especially for the so called self-broadened water vapor continuum, where the absorption coefficients become negative for certain g-points already in the 320's K.

We deal with this problem by applying an exponential extrapolation scheme for temperatures of up to at least 400 K. This is no perfect solution, but ascertains that negative absorption coefficients do not occur in the range of temperatures we are interested in and allows thus for running the model stably to up to 400 K. The extrapolation works as follows:

$$k(T, g) = k(T_1, g) \cdot \left( \frac{k(T_2, g)}{k(T_1, g)} \right)^{\frac{T-T_1}{T_2-T_1}}, \quad (\text{A.39})$$

where  $k$  is the molecular absorption coefficient for a given temperature  $T$  and g-point  $g$ .  $T_1$  and  $T_2$  are reference temperatures for which the absorption coefficients are tabulated. In practice  $T_1$  and  $T_2$  are the two highest temperatures for which a value of the absorption coefficient is tabulated in the lookup-tables.

The extrapolation is performed in the longwave radiation scheme for the molecular absorption coefficients of the self-broadened water vapor continuum, of the foreign-broadened water vapor continuum, of the key coefficients for the lower atmosphere and the upper atmosphere as well as for the minor coefficients for the lower atmosphere and the upper atmosphere.

In the shortwave radiation scheme the extrapolation is performed for the self-broadened water vapor continuum only. However, the other absorption coefficients are set to be zero, if they would be extrapolated to negative values.

### A.2.2 Lookup-table for the integrated Planck function

The original radiation code interpolates the values of both the spectrally integrated Planck function, which is required to calculate the thermal emission, and of its derivative with respect to temperature from a lookup table. However, values are tabulated only for temperatures of up to 340 K. Above this temperature the code performs a linear extrapolation which leads to an error since the spectral integral of the Planck function increases with the fourth power of temperature and thus leads to large errors as the temperature increases beyond 340 K. Therefore, we extended the table for integrated Planck function as well as for its derivative to temperatures of up to 400 K. We would like to point out that this is neither an extrapolation nor an approximation, but that we integrated numerically the Planck function as well as its derivative band-wise for each temperature in intervals of 1 K up to 400 K.

### A.2.3 Concentrations of radiatively active gases

Concentrations of radiatively active gases require to be transformed into number of molecules per area in order to be processed by the radiative transfer routines. The transformation is, however, different for water vapor from the other radiatively active gases, because the abundance of water vapor is given as a specific quantity (mass of water vapor per total mass), whereas the abundance of the other gases is given (after a transformation) as mass mixing ratio (mass of gas per mass of dry air). If  $x_i$  is the mass mixing ratio of the species  $i$  and  $q$  is the specific humidity then the number of molecules per area of the layer  $j$   $w_i(j)$  can be written as

$$\begin{aligned} w_i(j) &= \frac{N_A \Delta p_j}{m_i g} \cdot x_i(j) \\ w_v(j) &= \frac{N_A \Delta P_j}{m_v g} \cdot q(j) \quad , \end{aligned} \tag{A.40}$$

where  $v$  denotes water vapor,  $m_v$  the molecular mass thereof,  $m_i$  the molecular mass of the species  $i$ ,  $N_A$  the Avogadro constant,  $\Delta p_j$  the difference in pressure of dry air between the levels  $j$  and  $j - 1$  and  $\Delta P_j$  is the difference in total pressure between these levels. If the amount of water vapor is small then the pressure of dry air and the mass mixing ratio of water vapor may be used to calculate  $w_v(j)$  (as is done in the original version of the code), but this formulation leads to large errors if water vapor becomes a major atmospheric constituent.

# List of Figures

- 1.1 Sketch of previous results obtained in studies considering strong solar forcing. The blue ball denotes Earth's present surface temperature and TSI. Solid (colored) lines denote steady states found in previous studies and dashed lines denote climate instabilities. The red lines indicates the results obtained with one-dimensional models and violet lines denote the results obtained with three-dimensional models. The lower limit of surface temperatures of the Moist Greenhouse is supposed to lie around 340 K and the hard upper limit is the critical temperature of water (647 K). . . . . 2
- 2.1 Temporal mean of the SST over the last five years of the 50-years simulation as a function of TSI, for CSC (top left panel), for FSC with the Sundqvist scheme (top right panel) and with the Tompkins scheme (bottom right panel). Triangles indicate that the initial SST was below 290 K, and circles indicate that the initial SST was between 380 K and 385 K for CSC and FSC with the Sundqvist scheme, and between 360 K and 365 K with FSC with the Tompkins scheme. There are no marks for simulations in which a Runaway Greenhouse occurs within the fifty years. . . . . 19
- 2.2 Temporal evolution of the radiative imbalance at top of the atmosphere ( $I_{NET}$ ) as a function of SST for four realizations with an initial  $SST_{ini}$  of 286.8 K but different TSIs. For CSC (left panel) TSIs are  $1.10 S_0$  (black),  $1.12 S_0$  (red),  $1.13 S_0$  (blue) and  $1.15 S_0$  (green). For FSC with the Sundqvist scheme (right panel) the TSIs are  $1.35 S_0$  (black),  $1.38 S_0$  (red),  $1.39 S_0$  (blue) and  $1.40 S_0$  (green). The circles mark the value of the temporal average over the last five years of the 50-years simulation. . . . . 20

- 2.3 Atmospheric profiles of the temporal average over the last five years of simulation of cloud condensate (black, left panels) and temperature (red, left panels) and of cloud cover (black, right panels) and temperature (red, right panels). The vertical axis is the height in terms of pressure of dry air. The panels on the top show the results of one simulation with a cold start ( $SST_{ini} = 286.8$  K) for present-day insolation  $S_0$  for the Sundqvist scheme and the lower panels show the result of a simulation with the same initial SST for the same TSI but for the Tompkins scheme. These are the two control simulations for present-day climate for each of the cloud-cover schemes. . . . . 21
- 2.4 Temporal mean of the effective albedo over the last five years of simulation as a function of TSI for FSC with the Sundqvist scheme (left panel) and FSC with the Tompkins scheme (right panel). The curves are calculated by solving the energy balance at the top of the atmosphere for the albedo, with the OLR kept constant. Triangles indicate that the initial SST was below 290 K, and circles indicate that the initial SST was between 380 K and 385 K for CSC and FSC with the Sundqvist scheme, and between 360 K and 365 K with FSC the Tompkins scheme. There are no marks for simulations in which a Runaway Greenhouse occurs. . . . . 22
- 2.5 Cloud cover and cloud condensate in equilibrium: The top panels show the the temporal average over the last five years of simulation of cloud condensate (left) and fractional cloud cover (right) of one ensemble member with a cold start for different values of TSI with the Sundqvist scheme. The lower panels show the same variables for the Tompkins scheme. The vertical coordinate is height (in terms of pressure of dry air). The line contours on the left panels denote the temperatures in K. There are no steady states for TSIs larger than  $1.5 S_0$  for the Sundqvist scheme. Furthermore the simulation with a TSI of  $1.4 S_0$  was extended for an additional 30 years for the Sundqvist scheme to ensure that the equilibrium was attained. . . . . 23
- 2.6 The upper panels show the temporal evolution of fractional cloud cover as a function of time and height (in terms of pressure of dry air) for a simulation with a cold start ( $SST_{ini} = 286.8$  K) for a TSI of  $1.45 S_0$  for the Sundqvist scheme (left) and the Tompkins scheme (right). The lower panels show the fractional cloud cover of the same simulations plotted against the SST up to 360 K for the Sundqvist scheme (left) and the Tompkins scheme (right). . . . 24

- 2.7 Temporal evolution of the radiative imbalance at the top of the atmosphere ( $I_{NET}$ , black line) against the OLR (left panels, red line) as well as against the net outgoing shortwave radiation (right panels, blue line). The panels on the top show the results of one simulation with a cold start ( $SST_{ini} = 286.8$  K) for a TSI of  $1.45 S_0$  for the Sundqvist scheme and the lower panels show the result of a simulation with the same initial SST for the same TSI but for the Tompkins scheme. The simulation for the Sundqvist scheme and the one for the Tompkins scheme are the same as the ones shown in Figure 2.6. . . . . 26
- 2.8 Temporal mean of the vertically integrated mass of cloud condensate over the last five years of simulation as a function of TSI for FSC with the Sundqvist scheme (left panel) and FSC with the Tompkins scheme (right panel). Triangles indicate that the initial SST was below 290 K, and circles indicate that the initial SST was between 380 K and 385 K for CSC and with the Sundqvist scheme, and between 360 K and 365 K with FSC and with the Tompkins scheme. There are no marks for simulations in which a Runaway Greenhouse occurs. . . . . 27
- 3.1 Annual mean of globally averaged SST against time in years. The circles denote the four states from which new simulations were started. For a TSI of  $1.0 S_0$  and  $1.6 S_0$  two simulations were performed. . . . . 46
- 3.2 Zonal and temporal average over the last 30 years in steady-state of SST (top left panel), total amount of cloud condensate (bottom left panel), total cloud cover (top right panel) and albedo (bottom right panel) for five different simulations plotted against latitude. The horizontal axis is scaled with the sine of the latitude. . . . . 47
- 3.3 Temporal average over the last 30 years of the Eulerian-mean mass-stream function (left panels) and the vertical velocity (right panels) for the simulation with a TSI of  $1.06 S_0$  in the cold steady-state (top panels) and in the warm steady-state (bottom panels). The vertical axes are the height in terms of pressure of dry air and the horizontal axes are the latitude scaled with its sine. Blue contour lines denote clockwise rotation and red contour lines denote counter-clockwise rotation on the left panels. . . . . 48
- 3.4 Difference of the zonal and temporal average over the last 30 years of the steady-state radiative imbalance at the top of the atmosphere (TOA) between the warm and the cold state for the simulation with a TSI of  $1.06 S_0$  plotted as a function of Latitude. The black line denotes the net difference in imbalance, the red line denotes the difference in the LW-contribution and the blue line denotes the difference in the SW-contribution to the net imbalance. The horizontal axis is scaled as the sine of the latitude. . . . . 49

- 3.5 Zonal and temporal average over the last 30 years of the cloud condensate (left panels) and the fractional cloud cover (right panels) for the simulation with a TSI of  $1.06 S_0$  in the cold steady-state (top panels) and in the warm steady-state (bottom panels). The contours on the left panels denote temperatures in Kelvin. The vertical axis is the height in terms of pressure of dry air and the horizontal axis is the latitude scaled with its sine. . . . . 50
- 3.6 Temporal average over the last 30 years of the specific humidity for the simulations with a TSI of  $1.06 S_0$  in the cold steady-state (top left panel) and in the warm steady-state (top right panel), and with a TSI of  $1.20 S_0$  (bottom right panel). The contours denote temperatures in Kelvin, in intervals of 20 K above 220 K and in intervals of 10 K below 220 K. The vertical axis is the height in terms of pressure of dry air and the horizontal axis is the latitude scaled with its sine. . . . . 51
- 3.7 Zonal mean of total radiative effect (top left panel), of longwave effect (top right panel), of shortwave effect (bottom left panel) and of longwave cloud-radiative effect (bottom right panel) as a function of the global SST and latitude, for the transient simulation with a TSI of  $1.08 S_0$ . The radiative effects are calculated as changes from the initial radiative imbalances. The latitude is scaled with its sine. The global average of these quantities is plotted as a function of gSST to the right of the zonal averages. . . . . 52
- 3.8 Zonal mean of SST (top left panel), of vertical winds at 500 hPa (top right panel), of change in total cloud condensate (bottom left panel) and of change in total cloud cover (bottom right panel) as a function of the global SST and latitude for the transient simulation with a TSI of  $1.08 S_0$ . The latitude is scaled with its sine. The changes in total cloud condensate, total cloud cover and vertical winds are with respect to the annual average of the first year of simulation. . . . . 53
- 3.9 Zonal mean of fractional cloud cover for the transient simulation with a TSI of  $1.08 S_0$  at global SSTs of 297 K (top left panel), of 300 K (top right panel), of 305 K (bottom left panel) and of 310 K (bottom right panel). The vertical axis is the height in terms of pressure of dry air and the horizontal axis is the latitude scaled with its sine. . . . . 54
- 3.10 Zonal mean of the density of cloud condensate for the transient simulation with a TSI of  $1.08 S_0$  at global SSTs of 305 K (top left panel), of 315 K (top right panel), of 325 K (bottom left panel) and of 335 K (bottom right panel). The contours denote temperatures in Kelvin. The vertical axis is the height in terms of pressure of dry air and the horizontal axis is the latitude scaled with its sine. . . . . 55

- 3.11 Changes in the Hadley cells during the transient period of the simulation with  $a$  of  $1.08 S_0$ . The width of the arrows scales with the flux of the associated quantity. The top left panel shows the initial state. In a first phase (top right panel) the subsidence region dries and leads to a decrease of planetary boundary layer and to a decrease of reflected shortwave radiation. In a second phase (bottom left panel) the weakening of the circulation leads to an increase of convective activity in the subsidence region and leads to a reduction of outgoing longwave radiation. During a last phase (bottom right panel) the convective clouds become increasingly thick which leads to an increase in reflected shortwave radiation. . . . . 58
- 4.1 Sketch of two temperature profiles with surface temperatures  $T_{s_1}$  and  $T_{s_2}$  in temperature-optical-depth space in the region of the TOA. The shaded part corresponds to the optically thick part of the atmosphere below  $\tau_0$ . The finite temperature  $T = T_a$  is defined according to the condition (4.7). . . . . 74
- 4.2 Sketch of two temperature profiles with surface temperatures  $T_{s_1}$  and  $T_{s_2}$  in temperature-optical-depth space in the region of the TOA. The shaded part corresponds to the optically thick part of the atmosphere below  $\tau_0$ .  $\hat{T}(\tau)$  denotes the limit profile defined in condition (4.8). . . . . 75



---

# Bibliography

- Abe, Y., Abe-Ouchi, A., Sleep, N. H., and Zahnle, K. J. (2011). Habitable zone limits for dry planets. *Astrobiology*, 11(5):443–460.
- Abe, Y. and Matsui, T. (1988). Evolution of an impact-generated h<sub>2</sub>o-co<sub>2</sub> atmosphere and formation of a hot proto-ocean on earth. *Journal of the Atmospheric Sciences*, 45(21):3081–3101.
- Boer, G. J., Hamilton, K., and Zhu, W. (2005). Climate sensitivity and climate change under strong forcing. *Climate Dynamics*, 24(7-8):685–700.
- Bony, S., Colman, R., Kattsov, V. M., Allan, R. P., Bretherton, C. S., Dufresne, J.-L., Hall, A., Hallegatte, S., Holland, M. M., W-Ingram, Randall, D. A., Soden, B. J., Tselioudis, G., and Webb, M. J. (2006). How well do we understand and evaluate climate change feedback processes? *Journal of Climate*, 19(15):3445–3482.
- Brient, F. and Bony, S. (2013). Interpretation of the positive low-cloud feedback predicted by a climate model under global warming. *Climate Dynamics*, 40(9-10):2415–2431.
- Clement, A. C., Burgman, R., and Norris, J. R. (2009). Observational and model evidence for positive low-level cloud feedback. *Science*, 325(5939):460–464.
- Colman, R. (2003). A comparison of climate feedbacks in general circulation models. *Climate Dynamics*, 20(7-8):865–873.
- Debergh, C., Bezard, B., Owen, T., Crisp, D., Maillard, J.-P., and Lutz, B. L. (1991). Deuterium on venus - observations from earth. *Science*, 251(4993):547–549.
- Donahue, T. M., Hoffman, J. H., Hodges, R. R., and Watson, A. J. (1982). Venus was wet - a measurement of the ratio of deuterium to hydrogen. *Science*, 216(4546):630–633.
- Donohoe, A. and Battisti, D. S. (2011). Atmospheric and surface contributions to planetary albedo. *Journal of Climate*, 24(16):4402–4418.
- Gold, T. (1964). Outgassing process on the moon and venus. In *The Origin and Evolution of Atmospheres and Oceans*, pages 249–256. Wiley and Sons, New York.

- Goldblatt, C., Robinson, T. D., Zahnle, K. J., and Crisp, D. (2013). Low simulated radiation limit for runaway greenhouse climates. *Nature Geoscience*, 6(8):661–667.
- Goldblatt, C. and Watson, A. J. (2012). The runaway greenhouse: implications for future climate change, geoengineering and planetary atmospheres. *Philosophical Transactions of the Royal Society a-Mathematical Physical and Engineering Sciences*, 370(1974):4197–4216.
- Hartmann, D. L. and Larson, K. (2002). An important constraint on tropical cloud - climate feedback. *Geophysical Research Letters*, 29(20).
- Heinemann, M. (2009). Warm and sensitive paleocene-eocene climate. Reports on Earth System Science 70/2009, Max-Planck-Institute for Meteorology, Hamburg.
- Iacono, M. J., Delamere, J. S., Mlawer, E. J., Shephard, M. W., Clough, S. A., and Collins, W. D. (2008). Radiative forcing by long-lived greenhouse gases: Calculations with the AER radiative transfer models. *Journal of Geophysical Research: Atmospheres*, 113(D13).
- Ingersoll, A. P. (1969). Runaway greenhouse - a history of water on venus. *Journal of the Atmospheric Sciences*, 26(6):1191–1198.
- Ishiwatari, M., Nakajima, K., Takehiro, S., and Hayashi, Y.-Y. (2007). Dependence of climate states of gray atmosphere on solar constant: From the runaway greenhouse to the snowball states. *Journal of Geophysical Research: Atmospheres*, 112(D13).
- Ishiwatari, M., Takehiro, S., Nakajima, K., and Hayashi, Y. Y. (2002). A numerical study on appearance of the runaway greenhouse state of a three-dimensional gray atmosphere. *Journal of the Atmospheric Sciences*, 59(22):3223–3238.
- Kasting, J. F. (1988). Runaway and moist greenhouse atmospheres and the evolution of earth and venus. *Icarus*, 74:472–494.
- Kasting, J. F., Pollack, J. B., and Ackerman, T. P. (1984). Response of earths atmosphere to increases in solar flux and implications for loss of water from venus. *Icarus*, 57(3):335–355.
- Kasting, J. F., Whitmire, D. P., and Reynolds, R. T. (1993). Habitable zones around main-sequence stars. *Icarus*, 101(1):108–128.
- Komabayashi, M. (1967). Discrete equilibrium temperatures of a hypothetical planet with the atmosphere and the hydrosphere of one component-two phase system under constant solar radiation. *Journal of the Meteorological Society of Japan*, 45(1):137–139.
- Kopparapu, R. K., Ramirez, R., Kasting, J. F., Eymet, V., Robinson, T. D., Mahadevan, S., Terrien, R. C., Domagal-Goldman, S., Meadows, V., and Deshpande, R. (2013). Habitable zones around main-sequence stars: New estimates. *Astrophysical Journal*, 765(2).

- Lacis, A. A. and Oinas, V. (1991). A description of the correlated kappa-distribution method for modeling nongray gaseous absorption, thermal emission, and multiple-scattering in vertically inhomogeneous atmospheres. *Journal of Geophysical Research: Atmospheres*, 96(D5):9027–9063.
- Levine, X. J. and Schneider, T. (2011). Response of the hadley circulation to climate change in an aquaplanet GCM coupled to a simple representation of ocean heat transport. *Journal of the Atmospheric Sciences*, 68(4):769–783.
- Lohmann, U. and Roeckner, E. (1996). Design and performance of a new cloud microphysics scheme developed for the ECHAM general circulation model. *Climate Dynamics*, 12(8):557–572.
- Mauritsen, T., Stevens, B., Roeckner, E., Crueger, T., Esch, M., Giorgetta, M., Haak, H., Jungclaus, J., Klocke, D., Matei, D., Mikolajewicz, U., Notz, D., Pincus, R., Schmidt, H., and Tomassini, L. (2012). Tuning the climate of a global model. *Journal of Advances in Modeling Earth Systems*, 4.
- Meadows, V. S. and Crisp, D. (1996). Ground-based near-infrared observations of the venus nightside: The thermal structure and water abundance near the surface. *Journal of Geophysical Research: Planets*, 101(E2):4595–4622.
- Meraner, K., Mauritsen, T., and Voigt, A. (2013). Robust increase in equilibrium climate sensitivity under global warming. *Geophysical Research Letters*, 40:5944–5948.
- Mlawer, E. J., Taubman, S. J., Brown, P. D., Iacono, M. J., and Clough, S. A. (1997). Radiative transfer for inhomogeneous atmospheres: RRTM, a validated correlated-k model for the longwave. *Journal of Geophysical Research*, 102(D14):16663–16682.
- Nakajima, S., Hayashi, Y.-Y., and Abe, Y. (1992). A study on the runaway greenhouse-effect with a one-dimensional radiative convective equilibrium-model. *Journal of the Atmospheric Sciences*, 49(23):2256–2266.
- Newman, M. J. and Rood, R. T. (1977). Implications of solar evolution for earths early atmosphere. *Science*, 198(4321):1035–1037.
- Nordeng, T.-E. (1994). Extended versions of the convective parametrization scheme at ECMWF and their impact on the mean and transient activity of the model in the tropics. Technical Memorandum 206, ECMWF.
- O’Gorman, P. A. and Schneider, T. (2008). The hydrological cycle over a wide range of climates simulated with an idealized GCM. *Journal of Climate*, 21(15):3815–3832.
- Pierrehumbert, R. T. (2010). *Principles of Planetary Climate*. Cambridge University Press.

- Pikuta, E. V., Hoover, R. B., and Tang, J. (2007). Microbial extremophiles at the limits of life. *Critical Reviews in Microbiology*, 33(3):183–209.
- Pollack, J. B. (1971). Nongrey calculation of runaway greenhouse - implications for venus past and present. *Icarus*, 14(3):295–306.
- Popp, M., Schmidt, H., and Marotzke, J. (2014). Initiation of a runaway greenhouse in a cloudy column. *Submitted to the Journal of the Atmospheric Sciences*.
- Renno, N. O. (1997). Multiple equilibria in radiative-convective atmospheres. *Tellus*, 49:423–438.
- Renno, N. O., Stone, P. H., and Emanuel, K. A. (1994). Radiative-convective model with an explicit hydrologic-cycle .2. sensitivity to large changes in solar forcing. *Journal of Geophysical Research*, 99(D8):17001–17020.
- Ribas, I., Guinan, E. F., Gudel, M., and Audard, M. (2005). Evolution of the solar activity over time and effects on planetary atmospheres. i. high-energy irradiances (1-1700 angstrom). *Astrophysical Journal*, 622(1):680–694.
- Roeckner, E., Baeuml, G., Bonaventura, L., Brokopf, R., Esch, M., Giorgetta, M., Hagemann, S., Kirchner, I., Kornblueh, L., Manzini, E., Rhodin, A., Schlese, U., Schulzweida, U., and Tompkins, A. (2003). MPI-Report no. 349: The atmospheric general circulation model ECHAM5 part 1. Technical Report 349, Max-Planck-Institute for Meteorology, Hamburg.
- Rothschild, L. J. and Mancinelli, R. L. (2001). Life in extreme environments. *Nature*, 409(6823):1092–1101.
- Sackmann, I.-J., Boothroyd, A. I., and Kraemer, K. E. (1993). Our sun. 3. present and future. *Astrophysical Journal*, 418(1):457–468.
- Simpson, C. G. (1927). Some studies in terrestrial radiation. *Memoirs of the Royal Meteorological Society*, 2(16):69–95.
- Simpson, C. G. (1928). Further studies in terrestrial radiation. *Memoirs of the Royal Meteorological Society*, 3(1/10):1–26.
- Soden, B. J., Held, I. M., Colman, R., Shell, K. M., Kiehl, J. T., and Shields, C. A. (2008). Quantifying climate feedbacks using radiative kernels. *Journal of Climate*, 21(14):3504–3520.
- Stevens, B. and Bony, S. (2013). What are climate models missing? *Science*, 340(6136):1053–1054.

- Stevens, B., Giorgetta, M., Mauritsen, T., Crueger, T., Rast, S., Salzmann, M., Schmidt, H., Bader, J., Block, K., Brokopf, R., Fast, I., Kinne, S., Kornbluh, L., Lohmann, U., Pincus, R., Reichler, T., and Roeckner, E. (2013). The atmospheric component of the MPI-M earth system model: ECHAM6. *Journal of Advances in Modeling Earth Systems*.
- Sugiyama, M., Stone, P. H., and Emanuel, K. A. (2005). The role of relative humidity in radiative-convective equilibrium. *Journal of the Atmospheric Sciences*, 62(6):2001–2011.
- Sundqvist, H., Berge, E., and Kristjansson, J. E. (1989). Condensation and cloud parameterization studies with a mesoscale numerical weather prediction model. *Mon. Wea. Rev.*, 117(8):1641–1657.
- Tiedtke, M. (1989). A comprehensive mass flux scheme for cumulus parameterization in large-scale models. *Mon. Wea. Rev.*, 117(8):1779–1800.
- Tompkins, A. M. (2002). A prognostic parameterization for the subgrid-scale variability of water vapor and clouds in large-scale models and its use to diagnose cloud cover. *Journal of the Atmospheric Sciences*, 59(12):1917–1942.
- Vardavas, I. M. and Carver, J. H. (1985). Atmospheric-temperature response to variations in CO<sub>2</sub> concentration and the solar-constant. *Planetary and Space Science*, 33(10):1187–1207.
- Yang, J., Cowan, N. B., and Abbot, D. S. (2013). Stabilizing cloud feedback dramatically expands the habitable zone of tidally locked planets. *The Astrophysical Journal Letters*, 771(2):L45.



## Acknowledgements

First and foremost I would like to thank Jochem Marotzke and Hauke Schmidt for having taken upon them the arduous job of advising me during my PhD research. I see myself privileged to have benefited from the vast knowledge and experience of Jochem and I am thankful for having been allowed and encouraged to follow my own scientific curiosity on this interesting topic. Hauke has not only been both very interested and extremely helpful with my daily problems as well as with the overall progress of my work, but has also been very inspiring during our numerous scientific discussions.

I would like to thank Lennart Bengtsson for initiating the research on the topic of my thesis by asking whether the Runaway Greenhouse may not be worth studying.

I would like to express my gratitude to the International Max Planck Research School on Earth System Modelling (IMPRS-ESM) and especially to Antje Weitz, Cornelia Kampmann and Wiebke Böhm for all the support I received in the past years. They all make a tremendous job at running the IMPRS-ESM.

In fall 2009 Bjorn Stevens fished my application out of the not-to-be-considered-for-an-interview pile and unexpectedly decided that I should be invited to an interview. So I am not only very thankful to Bjorn for having done a great job as a panel chair, but also for having been given a chance to start my PhD research in the IMPRS-ESM.

I take the chance to express my gratitude to Sebastian Rast for his personal commitment in a lot of interesting discussions. His advice, especially concerning Chapter 3 and the model ECHAM6, have been crucial for the completion for this thesis. Furthermore, his personal advice has helped me a great deal in the last three years and I will not forget all the fun we had making stupid comments on virtually everything.

Many thanks to Erich Roeckner, Colin Goldblatt as well as to an anonymous Reviewer for their valuable comments and suggestions for Chapter 2 and to Cathy Hohenegger for her valuable comments and suggestions on Chapter 3.

I would like to thank Davide Zanchettin for being my office mate, personal proofreader, drummer, plant-waterer, plant-over-waterer, Italian-swearword-teacher, progmetal-concert companion, drinking and travel companion, complaint-box and in general just for having had a good time. I would like to thank Sajjad Saeed for the very nice time we had sharing the office. Thanks to the visiting students Johannes Kühn and Sebastian Milinsky for filling our office with life during their stay.

I would like to express my gratitude to Felix Bunzel for his friendship, help and advice. Felix has not only introduced me to Hamburg and to the Hamburger (the people, not the food), but also to his one and true love, the HSV.

My deepest gratitude goes to my colleagues Ritthik Bhattacharya, Jaison Ambadan Thomas and Fabio Cresto Aleina not only for their friendship and scientific and non-scientific advice, but also for the fun we had on several trips. Furthermore, I am extremely thankful to my colleagues and friends, especially to Hyung Sik Choi, Jan Ackmann, Daniel Goll, Jens Kieser, Matze Heinze, Suvarchal-Kumar Cheedala, Joni-Pekka Pietikäinen, Daniel Hernández Deckers, Mirjam Hirt and Josiane Salameh for their support, their help, their scientific and non-scientific advice and for all the fun we had.

My sincere thanks to Red Bull for keeping me awake when tired and for being a much better tasting alternative to coffee and Club Mate. Nonetheless, I would like to thank coffee for doing the job when Red Bull was not available.

Last but not least I would like to thank my friends and my family for their support.

## **Eidesstattliche Versicherung**

### ***Declaration on oath***

Hiermit erkläre ich an Eides Statt, dass ich die vorliegende Dissertationsschrift selbst verfasst und keine anderen als die angegebenen Quellen und Hilfsmittel benutzt habe.

*I hereby declare, on oath, that I have written the present dissertation by my own and have not used other than the acknowledged resources and aids.*

***Hamburg, den***

-----



Die gesamten Veröffentlichungen in der Publikationsreihe des MPI-M  
„Berichte zur Erdsystemforschung“,  
„Reports on Earth System Science“,  
ISSN 1614-1199

sind über die Internetseiten des Max-Planck-Instituts für Meteorologie  
erhältlich:

<http://www.mpimet.mpg.de/wissenschaft/publikationen.html>

